Doctoral Dissertation
Doctoral Program in Energy Engineering (29th Cycle)

Analysis of Combustion Phenomena and Knock Mitigation Techniques for High Efficient Spark Ignition Engines Through Experimental and Simulation Investigations

By

Mohsen Mirzaeian

******

Supervisor(s):
Professor Federico Millo

Doctoral Examination Committee:
Prof. Angelo Onorati, Referee, Politecnico di Milano, Milan, Italy
Prof. Michael Bargende, Referee, Universität Stuttgart, Stuttgart, Germany

Politecnico di Torino
2017

Declaration

I hereby declare that, the contents and organization of this dissertation constitute my own original work and does not compromise in any way the rights of third parties, including those relating to the security of personal data.

Mohsen Mirzaeian

2017

* This dissertation is presented in partial fulfillment of the requirements for **Ph.D. degree** in the Graduate School of Politecnico di Torino (ScuDo).

I would like to dedicate this thesis to my loving parents

Acknowledgment

It is my pleasure to acknowledge the roles of several individuals who were instrumental for completion of my PhD thesis.

Foremost, I would like to express my gratitude to my dear supervisor, Professor Federico Millo, whose expertise, understanding, and patience, added considerably to my graduate experience. The best advisor and teacher I could have wished for, he is actively involved in the work of all his students, and clearly always has their best interest in mind.

Besides my advisor, my sincere thanks also goes to Gamma Technologies LLC, IL, USA which sponsored my scholarship specially Dr. Syed Wahiduzzaman, Dr. Navin Fogla and Dr. Mike Bybee for offering me the summer internship opportunities and for their invaluable support during my study.

I must also acknowledge Eng. Massimo Ferrera, Eng. Vittorio Doria, Eng. Andrea Stroppiana, Dr. Sabino Luisi and Eng. Caterina Venezia from Centro Ricerche Fiat (CRF), Italy and Professor Lucio Postrioti from Spin off of University of Perugia, STSe – Shot to Shot Engineering., Italy for providing experimental data and their technical support.

I greatly appreciate the support received through the collaborative work undertaken with Argonn National Laboratory, USA with special thanks you to Dr. Janardhan Kodavasal and Dr. Sibendu Som for their collaboration and availability.

I would also like to thank Eng. Andrea Bianco from POWERTECH Engineering, Italy for his continuous support and useful suggestions.

These acknowledgements would not be complete without mentioning my research lab colleagues: Andrea Piano, Sabino Caputo, Giulio Boccardo, Alessandro Zanelli, Claudio Cubito, Francesco Sapio, Luciano Rolando, Daniele Porcu, Pranav Arya and Giuseppe Di Pierro. It was a great pleasure working with them and I appreciate their ideas, help and good humor.

I would like to give special thanks to Mahsa for standing beside me throughout my career and for supporting me during big troubles in addition to tolerating my behavior during the time that I was tired of problems.

To my family, thank you for encouraging me in all of my pursuits and inspiring me to follow my dreams. I am grateful to my parents, sister and brother who supported me emotionally and financially. I always knew that you believed in me and wanted the best for me. Thank you for teaching me that my job in life was to learn, to be happy, and to know and to understand myself; only then I could know and understand others.

Publications

Parte del lavoro descritto in questa tesi è stato anche preventivamente pubblicato in:

Part of the work described in this thesis was also previously published in the following publications:

1. V. Doria, A. Stroppiana, M. Ferrera, F. Millo, M. Mirzaeian, D. Porcu, "Knock Mitigation Techniques for Highly Boosted Downsized SI Engines: Miller Cycle and Water Injection", in: SIA Powertrain, Versailles, France, 2017.

2. Zhao, E., Moiz, A.A., Sibendu, S., Fogla, N., Bybee, M., Wahiduzzaman, S., Mirzaeian, M., Millo, F., Kodavasal, J., "Multi-cycle Large Eddy Simulation to Capture Cycle-to-Cycle Variation (CCV) in Spark-Ignited (Si) Engines", 10th US National Combustion Meeting, 2017.

3. Mirzaeian, M., Millo, F., Fogla, N., Bybee, M., Wahiduzzaman, S., Kodavasal, J., et al., "Modeling and Understanding Cycle-to-Cycle Variation Through Multi-Cycle LES", CONVERGE CFD User Conference, Vienna, 2017.

4. N. Fogla, M. Bybee, M. Mirzaeian, F. Millo, S. Wahiduzzaman, "Development of a K-k-∈ Phenomenological Model to Predict In-Cylinder Turbulence", SAE Int. J. Engines. 10 (2017) 562–575.

5. F. Millo, M. Mirzaeian, S. Luisi, V. Doria, A. Stroppiana, "Engine displacement modularity for enhancing automotive s.i. engines efficiency at part load", Fuel Journal. 180 (2016) 645–652. doi:10.1016/j.fuel.2016.04.049.

6. M. Mirzaeian, F. Millo, L. Rolando, "Assessment of the Predictive Capabilities of a Combustion Model for a Modern Downsized Turbocharged SI Engine", in: SAE Tech. Pap. 2016-01-0557, SAE International, 2016. doi:10.4271/2016-01-0557.

7. S. Luisi, V. Doria, A. Stroppiana, F. Millo, M. Mirzaeian, “Experimental Investigation on Early and Late Intake Valve Closures for Knock Mitigation through Miller Cycle in a Downsized Turbocharged Engine”, in: SAE Tech. Pap. 2015-01-0760, SAE International, 2015. doi:10.4271/2015-01-0760.

In addition, the following publications have already been submitted and are currently under review:

8. Ameen, M.M., Mirzaeian, M., Millo, F., Sibendu, S., “Numerical Prediction of CCV in a PFI Engine using a Parallel LES Approach”, Proceedings of the ASME 2017 Internal Combustion Fall Technical Conference

9. Zhao, E., Moiz, A.A., Sibendu, S., Fogla, N., Bybee, M., Wahiduzzaman, S., Mirzaeian, M., Millo, F., Kodavasal, J., “Examining the Role of Flame Topologies and In-cylinder Flow Field on Cyclic Variability in SI Engines Using Large Eddy Simulation”, International Journal of Engineering Research (IJER), 2017.

Abstract

Different technologies are being utilized nowadays aiming to boost the fuel efficiency of Spark-Ignition (SI) engines. Two promising technologies which are used to improve the part load efficiency of SI engines are the utilization of downsizing in combination with turbocharging and cylinder deactivation. Both technologies allow a shift of load points towards higher loads and therefore towards more efficient zones of the engine map, while performance is being preserved or even enhanced despite the smaller displacement thanks to high boost levels. However, utilization of both technologies will increase the risk of knock dramatically. Therefore, the abovementioned systems can be coupled with other technologies such as gasoline direct injection, Miller cycle and water injection to mitigate knock at higher load operating conditions.

Therefore, the aim of the current work is to investigate, through experimental and numerical analysis, the potential benefits of different knock mitigation techniques and to develop reliable and predictive simulation models aiming to detect root cause of cyclic variations and knock phenomena in downsized turbocharged SI engines.

After a brief introduction in Chapter 1, three different typical European downsized turbocharged SI engines have been introduced in Chapter 2, which were used for both experimental and simulation investigations, named as Engine A, which is downsized and turbocharged, Port Fuel Injection (PFI) with fixed valve lift and represents the baseline; Engine B, represents an upgraded version of Engine A, featuring Variable Valve Actuation (VVA), and Engine C which is a direct injection and further downsized engine.

Engine B, equipped with MultiAir VVA system, was utilized to evaluate the possible benefits of cylinder deactivation in terms of fuel economy at part load condition, which is discussed in Chapter 3. Since the MultiAir VVA system does not allow exhaust valve deactivation, an innovative strategy was developed, exploiting internal Exhaust Gas Recirculation (iEGR) in the inactive cylinders in order to minimize their pumping losses.

However, at higher load operating condition, risk of knock occurrence limits the performance of the engine. Therefore, the possible benefits of different knock mitigation techniques such as Miller Cycle and water injection in terms of fuel consumption were discussed in Chapter 4.

Potential benefits of Miller cycle in terms of knock mitigation are evaluated experimentally using Engine B, as shown in Chapter 4.2. After a preliminary investigation, the superior knock mitigation effect of Late Intake Valve Closure (LIVC) with respect to Early Intake Valve Closure (EIVC) strategy was confirmed;

therefore, the study was mainly focused on the latter system. It was found out that utilization of LIVC leads up to 20% improvement in the engine indicated fuel conversion efficiency.

Afterwards, Engine C, a gasoline direct injection engine, has been utilized in order to understand the potential benefits of water injection for knock mitigation technology coupled with the Miller Cycle, which is discussed in Chapter 4.3. Thanks to water injection potential for knock mitigation, the compression ratio could be increased from 10 to 13, which leads to an impressive efficiency improvement of 4.5%.

However, utilization of various advanced knock mitigation techniques in the development of SI engines make the system more complex, which invokes the necessity to develop reliable models to predict knock and to find the optimized configuration of modern high-performance, downsized and turbocharged SI engines. Considering that knock is strictly related to Cycle-to-Cycle Variations (CCV) of in-cylinder pressure, CCV prediction is an important step to predict the risk of abnormal combustion on a cycle by cycle basis.

Consequently, in Chapter 5, a procedure has been introduced aiming to predict the mean in-cylinder pressure and to mimic CCV at different operating conditions. First, a 0D turbulent combustion model has been calibrated based on the experimental data including various technologies used for knock mitigation which can impact significantly on the combustion process, such as Long Route EGR and

water injection. Afterwards, suitable perturbations are adapted to the mean cycle aiming to mimic CCV. Finally, the model has been coupled with a 0D knock model aiming to predict knock limited spark advance at different operating conditions.

Finally, in order to provide a further contribution towards the prediction of CCV, 3D-CFD Large Eddy Simulation (LES) has been carried out in order to better understand the root cause of CCV, presented in Chapter 6. Such analysis could be used to extract the physical perturbation from the 3D-CFD and to use it as an input for the 0D combustion model to predict CCV. The operating condition studied in this work is at 2500 rpm, 16 bar brake mean effective pressure (bmep) and stoichiometric condition. Based on the analysis conducted using LES, it was found out that the variability in combustion can be mainly attributed to both the direction of the velocity flow-field and its magnitude in the region around the spark plug. Furthermore, the effect of velocity field and equivalence ratio on the combustion has been decoupled, confirming that the former has the dominant effect while the latter has minor impact on combustion variability.

In conclusion, simulation models using 0D and 3D-CFD tools when calibrated properly based on experimental measurements can be used to support the design and the development of innovative downsized turbocharged SI engines considering the effects of CCV and knock on engine performance parameters.

Contents

List of Figures

List of Tables

Abbreviations

ABDC	After Bottom Dead Center
AEM	Activation Energy Multiplier
ATDC	After Top Dead Center
BDC	Bottom Dead Center
BSFC	Brake Specific Fuel Consumption
bmep	Brake mean effective pressure
CA	Crank Angle
CCV	Cycle-to-Cycle Variation
CD	Cylinder Deactivation
CFD	Computational Fluid Dynamics
COM	Center of Mass
COV	Coefficient of Variation
CPU	Central Processing Unit
CR	Compression Ratio
DE	Douaud and Eyzat
DEM	Dilution Exponent Multiplier
DoE	Design of Experiments
ECU	Electronic Control Unit
EGR	Exhuast Gas Recircultion
EIVC	Early Intake Valve Closure

EOI	End of Injection
GA	Genetic Algorithm
GDI	Gasoline Direct Injection
ICE	Internal Combustion Engine
ITM	Induction Time Multiplier
IVC	Intake Valve Closure
IVO	Intake Valve Opening
IMEP	Indicated Mean Effective Pressure
IMEPH	Indicated Mean Effective Pressure of the High pressure portion
IMEPL	Indicated Mean Effective Pressure of the Low pressure portion
iEGR	Internal Exhuast Gas Recircultion
KLSA	Knock Limited Spark Advance
KH	Kelvin-Helmholtz
LES	Large Eddy Simulation
LIVC	Late Intake Valve Closure
LIVO	Late Intake Valve Opening
LR	Long Route
MAPO	Maximum Amplitude of Pressure Oscillation
MFB	Mass Burnt Fraction
MKE	Mean Kinetic Energy
NP	Normal Production
NVH	Noise, Vibration, and Harshness

PCP	Peak Cylinder Pressure
PDA	Phase Doppler Anemometry
PDF	Probability Density Function
PFI	Port Fuel Injection
PMEP	Pumping Mean Effective Pressure
RANS	Reynolds Averaged Navier-Stokes
RNG	Renormalization Group
RON	Research Octane Number
RT	Rayleigh-Taylor
rpm	Round per minute
SA	Spark Advance
SCR	Selective Catalytic Reduction
SI	Spark-Ignition
SMD	Sauter Mean Diameter
TDC	Top Dead Center
TDCF	Top Dead Center Firing
TFSM	Turbulent Flame Speed Multiplier
TIT	Turbine Inlet Temperature
TKE	Turbulent Kinetic Energy
VVA	Variable Valve Actuation
WI	Water Injection
WOT	Wide Open Throttle

Symbols

A_f	Flame area
A_{tot}	Total area of all nozzles
B	Bore of the cylinder
B_m	Maximum laminar speed
B_ϕ	Laminar speed roll-off value
b_1	Modeling constant
b_3	Modeling constant
C_1	Tuning constant of the 0D turbulence model
C_2	Tuning constant of the 0D turbulence model
C_3	Tuning constant of the 0D turbulence model
C_a	Contraction coefficient
C_d	Discharge coefficients
C_{in}	0D turbulence model parameter
C_k	Flame kernel growth multiplier
C_s	Turbulent flame speed multiplier
$C_{s,dynamic}$	Dynamic Smagorinsky number
C_T	Tumble coefficient
C_{tumb}	Tuning constant of the 0D turbulence model
C_v	Velocity coefficients

C_β	0D turbulence model parameter
C_λ	0D combustion calibration multiplier
d_{noz}	Nozzle diameter
E_s	Speed dependent parameter
f	Tumble decay function
K	Mean kinetic energy
k	Turbulent kinetic energy
L	Angular momentum
L_b	Breakup length
L_I	Integral length scale
L_t	Turbulent length *scale*
M_b	Mass burnt
M_e	Entrained mass of the unburned gas
$MFB2$	2 % Mass fraction burnt
$MFB50$	50 % Mass fraction burnt
$MFB10-75$	Burn duration from 10% to 75%
$\dot{m}$	Mass flow rate
n	Engine revolution speed
n_{noz}	Number of nozzles
P	Pressure
P_k	Production of turbulent kinetic energy
$P_{\dot{\epsilon}}$	Production of turbulent dissipation rate

p_0	Reference pressure
p_f	Rectified in-cylinder pressure
p_{inj}	Injection pressure
R_f	Flame radius
Re_t	Reynolds number
r	Injected drop radius
$\tilde{r}$	Radius of the tumble macro-vortex
r_{23}	Sauter mean radius
s	Instantaneous piston stroke
S_L	Laminar flame speed
S_T	Turbulent flame speed
Sc	Turbulent Schmidt number
T_0	Reference temperature
T_u	Unburned gas temperature
t	Time
U	Mean velocity
u'	Turbulent intensity in the x direction
V	Volume
v	Isentropic velocity of the flow
v_{inj}	Injection velocity
v'	Turbulent intensity in the y direction
v_T	Turbulent viscosity

WF	Water fraction
w'	Turbulent intensity in the z direction
XX	Span of the flame in the X direction
YY	Span of the flame in the Y direction
ZZ	Span of the flame in the Z direction
α	The temperature exponent
β	Pressure exponent
Γ	Gamma function
Δ	Filter width
ε	Turbulent dissipation rate
λ	Taylor microscale of turbulence
ρ	Density
ρ_g	Gas phase density
ρ_l	Liquid phase density
$\dot{\rho}$	Rate of change of density
τ	Time scale/ Ignition delay
ϕ	In-cylinder equivalence ratio
ϕ_m	Fuel/air equivalence ratio at the maximum laminar flame speed
$\psi^{rateshape}$	Injection rate shape
ω	Angular speed of the tumble macro-vortex

Chapter 1

Introduction

The need to reduce anthropogenic greenhouse gases emissions has led most of the governments to set challenging targets for CO_2 emissions from passenger cars [1], as shown in Figure 1.

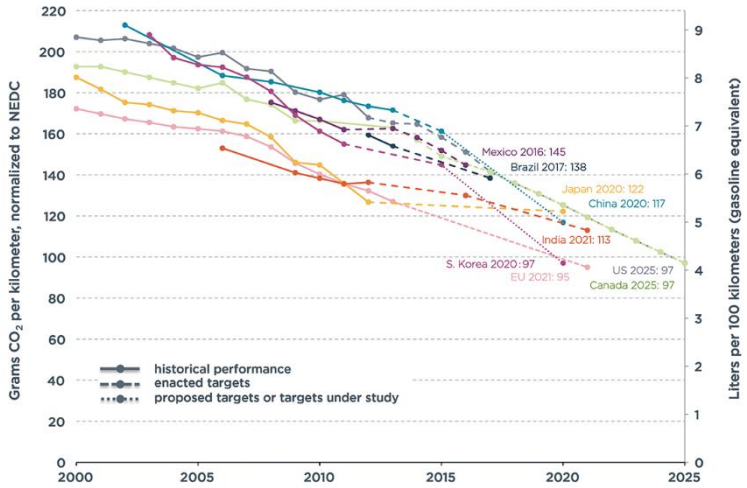

Figure 1. Trend of CO_2 emissions reduction targets in different countries [1]

Pollutant emissions are strictly related to engine operating conditions; hence, various emission test procedure and driving cycles have been established trying to reproduce the most significant operating conditions for different vehicle categories. Since for light duty vehicles the most frequent operating conditions are at low and medium load, as in the current procedure for type approval, which is based on the New European Driving Cycle (NEDC), the application of innovative technologies,

such as downsizing combined with turbocharging and cylinder deactivation, can be effectively implemented to reduce fuel consumption and pollutant emission at part load.

Downsizing combined with turbocharging has been proven to be an effective way to improve the fuel conversion efficiency [2,3] (Figure 2) in SI engines at part load operating condition. However, the utilization of high boost levels and high compression ratio can lead to dramatic increase of knock likelihood. Therefore, in order to mitigate knock occurrence, mixture enrichment and/or spark timing retard are generally being adopted [3–5], which consequently provoke a dramatic drop in fuel consumption efficiency at high load operating condition.

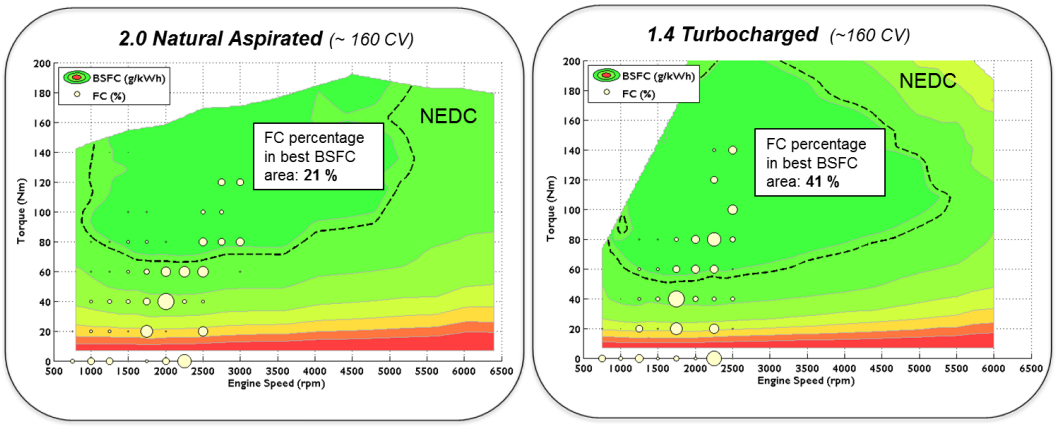

Figure 2. comparison of a natural aspirated and downsized turbocharged engine in terms of Brake Specific Fuel Consumption (BSFC) [6]

Cylinder deactivation [7] is another effective technology to improve spark ignition engines' efficiency at part load, thanks to its capability of significantly reducing pumping losses, by switching off a fraction of the cylinders at part load, while operating the active cylinders at higher loads and therefore with higher efficiencies. It can be observed (Figure 3, [8]) that cylinder deactivation can effectively reduce the fuel consumption at engine loads up to 5 bar brake mean effective pressure (bmep), while the utilization of this technology at higher loads is limited by knock.

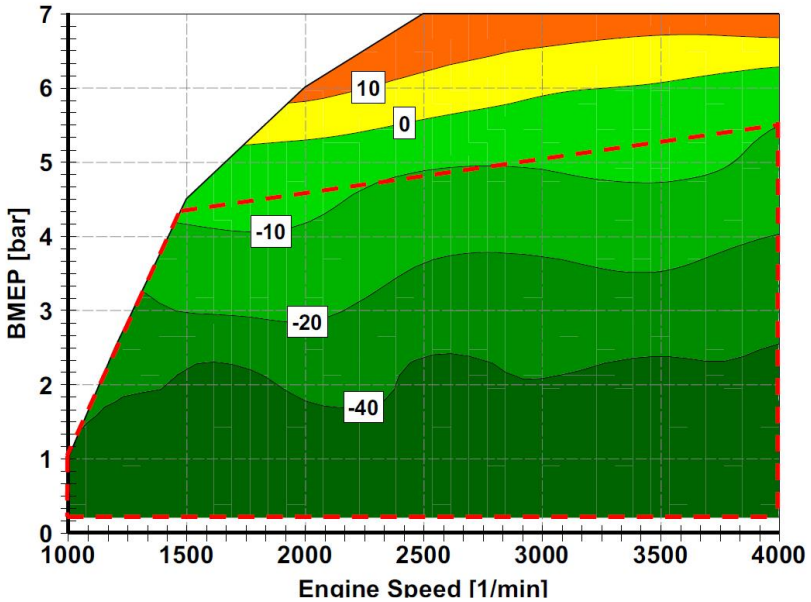

Figure 3. Difference of fuel consumption in 2-cylinder-modus to 4-cylinder-modus [g/kWh] (both throttle-free) [8]

The abovementioned technologies, downsizing combined with turbocharging and cylinder deactivation, are effective at part load operating condition; however, their application at higher load operating points is limited by knock. Currently, more dynamic test procedures such as Worldwide harmonized Light vehicles Test Procedures (WLTP) (shown in Figure 4) and Real Driving Emission (RDE) are being adopted with the aim to better represent real driving condition, while moving the operating area of the engine to higher loads. Therefore, understanding and mitigation of knock phenomena which is the bottleneck of SI engines at higher loads are of crucial importance.

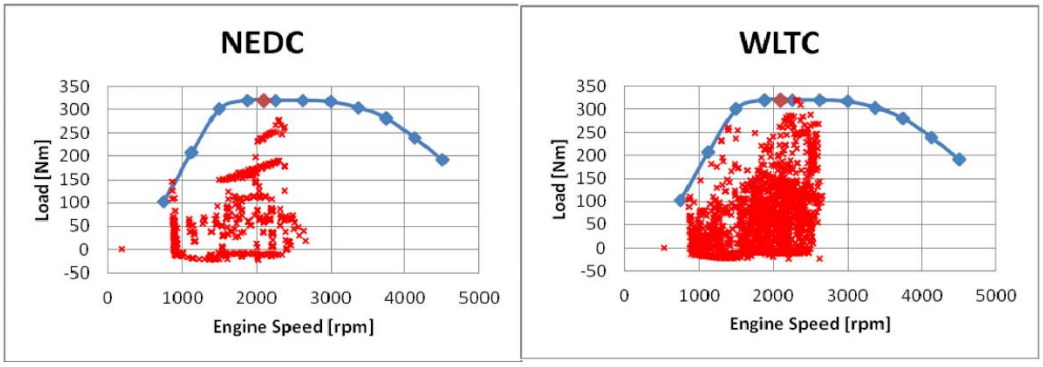

Figure 4. Comparison of NEDC (left) and WLTP (right) operating region [9]

As a consequence, various advanced technologies are currently being explored to achieve knock mitigation, including the adoption of cooled Exhaust Gas Recirculation (EGR) [10], [11], of variable compression ratio (for instance through

variable con rod length) [4], of Water Injection (WI) [12,13] and of Miller cycle [14,15]. Hence, it is of crucial importance to gather and to analyze extensive experimental data including such technologies aiming to understand their possible benefits in terms of fuel consumption. Furthermore, these technologies could be combined to maximize their fuel economy benefits which add further complexity to the engine calibration and design; therefore, it is necessary to have reliable models to find the optimized configuration and to support the production of modern high-performance, downsized and turbocharged SI engines.

Besides, experimental observations clearly show that SI engines are affected by a significant amount of Cycle-to-Cycle Variations (CCV) of cylinder pressure which is due to variability of combustion from one cycle to the subsequent one. Figure 5 indicates three different pressure traces and their corresponding burn rates of a 4-cylinder downsized, turbocharged SI engine at 2500 rpm and 16 bar bmep. It can be seen that not only the maximum pressure is different but also the crank angle at maximum pressure is changing. The differences in-cylinder pressure traces can be explained by the fact that the fuel is burning at different rates in each cycle (Figure 5-b). The variation of the in-cylinder pressure can be translated to difference in the indicated work. As an example, the Indicated Mean Effective Pressure (IMEP) of the fast and slow cycles are 17.3 and 16.14, respectively, which shows about 7% of variation from one cycle to the other. Therefore, it can be appreciated that CCV affects adversely the indicated work and consequently the fuel consumption in SI engines.

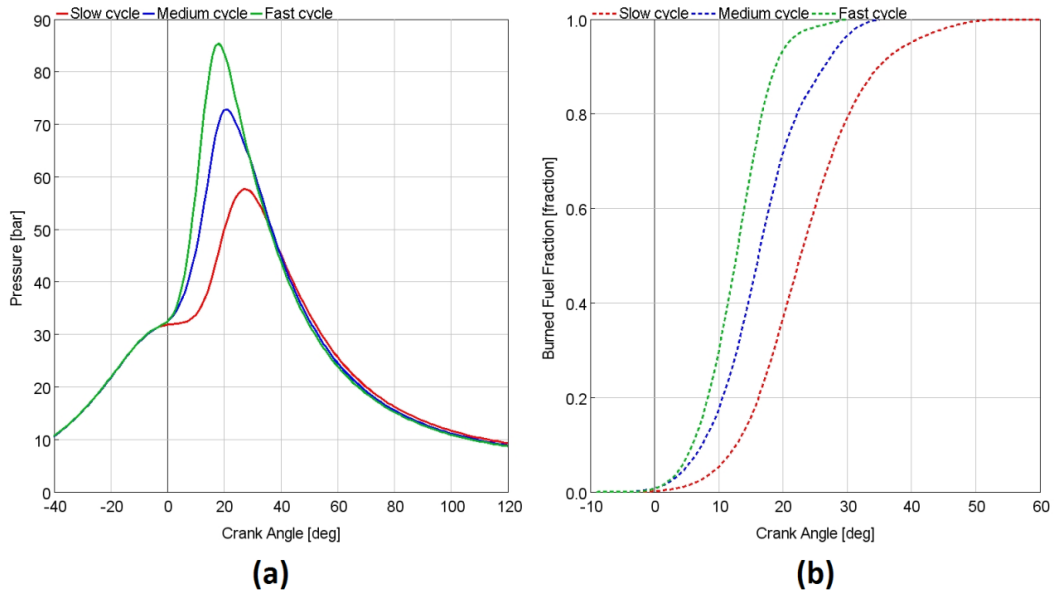

Figure 5. a) In-cylinder pressure at three different cycles b) Fraction of total fuel mass burned for the corresponding cycles

Moreover, considering that the mean cycle is not generally detonating and the faster than average cycle is more probable to knock, this phenomenon is heavily

dependent on CCV and cannot be described by looking at the average cycle only. Hence, as the application domain of the engine simulation models enters the relatively full load conditions, the modeling of cyclic variations becomes significantly important. As a consequence, robust and reliable methods for the prediction of the combustion process and CCV have become more and more important to support the design and calibration of modern high-performance, downsized and turbocharged SI engines.

Numerical investigations of the cyclic variation can be performed by two main categories of simulation tools: 0/1D simulation and three-dimensional Computational Fluid Dynamics simulations (3D-CFD).

The three-dimensional fluid-dynamics simulation performs the full analysis of the fluid motion and combustion independently from the complexity of the geometry analyzed. Therefore, the 3D-CFD could be utilized in the modelling of internal combustion engines. 3D-CFD has been extensively used for studying CCV also thanks to the unique possibilities offered by the Large-Eddy Simulation (LES) technique. Such technique could be used for the design purposes as well as to understand the root cause of CCV while due to huge Central Processing Unit (CPU) time required by 3D-CFD models, it is not possible to use them for the control and calibration purposes.

0/1D simulation represents another possible approach to model CCV. These models should be supported by an accurate model calibration with experimental data which allows to analyze and to predict combustion not only for the mean cycle but also its variability. Due to low computational time offered by 0/1D simulation, a great number of configurations can be compared in order to find the most suitable solution of the analyzed problem.

Hence, the aim of the current work was to gather a better understanding of causes of CCV and try to predict CCV in 0D, using the information coming from 3D CFD.

Parte del lavoro descritto in questo capitolo è stato anche preventivamente pubblicato in:

Part of the work described in this Chapter was also previously published in the following publications:

1. V. Doria, A. Stroppiana, M. Ferrera, F. Millo, M. Mirzaeian, D. Porcu, "Knock Mitigation Techniques for Highly Boosted Downsized SI Engines: Miller Cycle and Water Injection", in: SIA Powertrain, Versailles, France, 2017.

2. F. Millo, M. Mirzaeian, S. Luisi, V. Doria, A. Stroppiana, "Engine displacement modularity for enhancing automotive s.i. engines efficiency at part load", Fuel Journal. 180 (2016) 645–652. doi:10.1016/j.fuel.2016.04.049.

3. M. Mirzaeian, F. Millo, L. Rolando, "Assessment of the Predictive Capabilities of a Combustion Model for a Modern Downsized Turbocharged SI Engine", in: SAE Tech. Pap. 2016-01-0557, SAE International, 2016. doi:10.4271/2016-01-0557.

4. S. Luisi, V. Doria, A. Stroppiana, F. Millo, M. Mirzaeian, "Experimental Investigation on Early and Late Intake Valve Closures for Knock Mitigation through Miller Cycle in a Downsized Turbocharged Engine", in: SAE Tech. Pap. 2015-01-0760, SAE International, 2015. doi:10.4271/2015-01-0760.

Chapter 2

Experimental Set-up

The experimental and simulation analysis were performed on different engines, the main characteristic of which are summarized in this Chapter.

2.1 Engine A

The experimental activity was initially carried out in the Advanced Internal Combustion Engines Laboratory of the Energy Department of the Politecnico di Torino, Italy [16,17]. An extensive experimental campaign was carried out on a typical European 4-cylinder turbocharged SI engine (engine A), the main characteristics of which are reported in Table 1.

Table 1. Characteristics of Engine A

Number of cylinders / Arrangement	4 / In line
Displacement	1368 [cm^3]
Bore	72 [mm]
Stroke	84 [mm]
Injection System	Port Fuel Injection
Turbocharger	Fixed Geometry Turbine
Compression Ratio	9.8 : 1
Maximum Torque	270 Nm@ 3000 rpm
Maximum Power	132 kW@ 5750 rpm

The engine was installed on the test bench, shown in Figure 6, and connected to an eddy-current brake in its standard configuration. It was then equipped with 1 piezoelectric pressure transducer integrated in the spark-plug (KISTLER 6115) of cylinder #1, and 2 piezoresistive pressure transducers installed on the intake and exhaust ports of the same cylinder. Moreover, K-type thermocouples in the intake runners and at the turbine inlet, a linear lambda sensor mounted downstream of the turbine and a turbocharger speed sensor completed the experimental set-up.

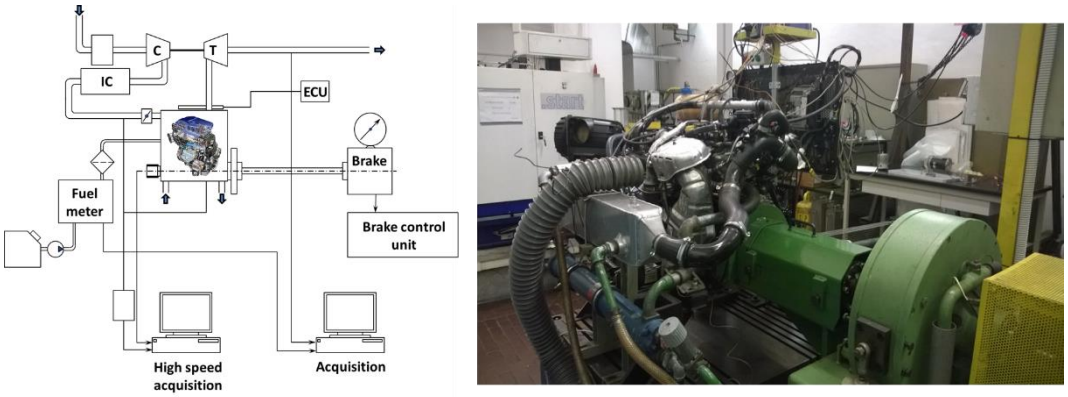

Figure 6.Test rig lay-out for Engine A

It is noteworthy that external EGR strategy has not been used in the experiment and the engine has been operated with a fixed valve timing at all operating conditions.

2.2 Engine B

Engine B, is similar to Engine A in terms of geometrical characteristics, while is equipped with Variable Valve Actuation (VVA) system. The experimental measurements have been carried out in Centro Ricerche Fiat (CRF), Italy [7,18]. The engine selected for the investigation is a Fiat MultiAir Fire 1.4 liter, turbocharged and Port Fuel Injected (PFI), the main features of which are listed in Table 2. The engine was fuelled with a 95 RON unleaded gasoline.

Table 2. Characteristics of Engine B

Number of cylinders / Arrangement	4 / In line
Displacement	1368 [cm^3]
Bore	72 [mm]
Stroke	84 [mm]
Injection System	Port Fuel Injection
Turbocharger	Fixed Geometry Turbine
VVA System	MultiAir

Compression Ratio	9.8 : 1
Maximum Torque	230 Nm@ 2000 rpm
Maximum Power	103 kW@ 5000 rpm

As far as intake valves are concerned, the engine is equipped with a tandem actuator, the MultiAir system [19], where both intake valves are operated by a unique actuator, the operating principle of which can be briefly summarized as follows, by means of the scheme shown in Figure 7. The cam is acting on a piston, which is connected to the intake valve through a hydraulic chamber filled by lubricant oil and can be used to couple or decouple the valve motion from the cam profile. The pressure in the hydraulic chamber is controlled by an on/off solenoid valve. When the solenoid valve is closed, the oil trapped into the chamber behaves like a solid body and transmits to the intake valve the lift schedule imposed by the intake cam profile. When the solenoid valve is open, the hydraulic chamber is depressurized and the intake valve is de-coupled from the camshaft: it does not follow the intake cam profile anymore and its motion is only determined by the inertia and return spring forces; the latter prevails, thus causing the valve closure, which can therefore be controlled by the opening of the solenoid valve, regardless of the cam profile. The final part of the valve closing stroke is controlled by a dedicated hydraulic brake to ensure a soft and regular landing phase at any engine operating condition. By controlling the solenoid valve actuation, both Early Intake Valve Closure (EIVC) and Late Intake Valve Opening (LIVO) strategies can be actuated, as shown in Figure 8 [19], [18].

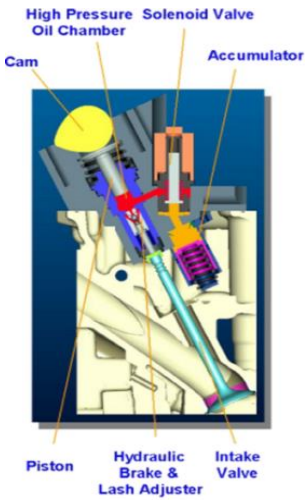

Figure 7. Scheme of the MultiAir VVA system for Engine B [18]

A specific intake cam lobe was designed in order to perform the planned experimental investigation on extreme late intake valve closures. While the Normal Production (NP) intake cam profile was designed to optimize the volumetric efficiency at 5500 rpm (that is the full rated power point of the tested engine), the

extreme late closure cam lobe allows a complete LIVC regulation with a maximum Intake Valve Closure (IVC) equal to the combustion Top Dead Center (TDC), as shown in Figure 9.

The engine was fully instrumented with four KISTLER 6052 C32 piezoelectric transducers which were installed on the engine cylinder head and coupled with a high-resolution (0.2 crank angle degrees) encoder for in-cylinder indicating analysis and knock detection.

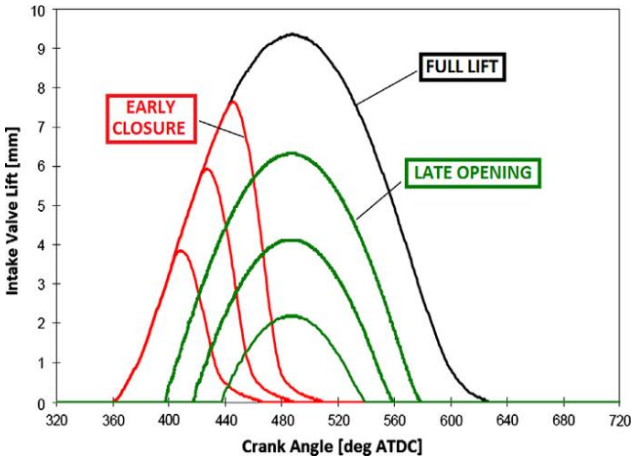

Figure 8. Examples of possible EIVC and LIVO strategies of the MultiAir VVA system [18]

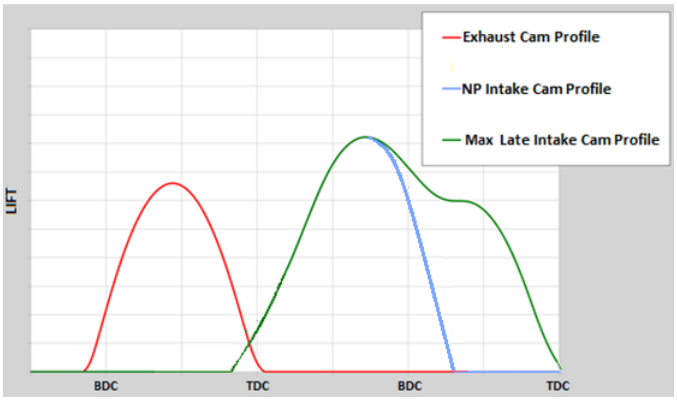

Figure 9. Exhaust and Intake cam profile tested [18]

2.3 Engine C

2.3.1 Engine set-up

Engine C is a Gasoline Direct Injection (GDI) European downsized, turbocharged SI engine equipped with VVA [6]. Two different engine set up were tested, one

with a Compression Ratio (CR) of 10 and one with a CR of 13. The experimental measurements have been carried out at Centro Ricerche Fiat (CRF), Italy.

Similar to Engine B, Engine C was fully instrumented with four KISTLER 6052 C32 piezoelectric transducers which were installed on the engine cylinder head and coupled with a high-resolution (0.2 crank angle degrees) encoder for in-cylinder indicating analysis and knock detection.

The engine was also equipped with a water injection system, including demineralized water tank, water pump, filter, 2 pressure transducers, a water rail, and the injectors. The injected water temperature is equal to 25°C. A schematic representation of the water injector position is shown in Figure 10.

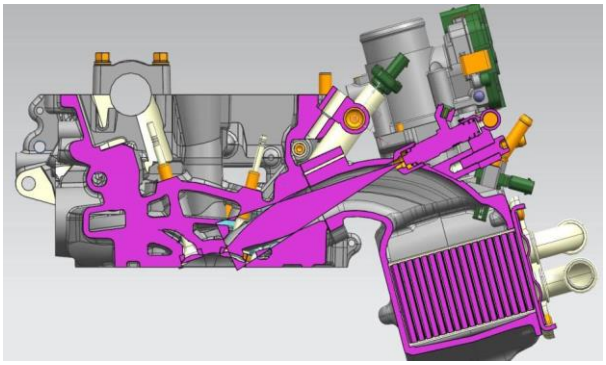

Figure 10. Schematic representation of the water injector position for Engine C [6]

2.3.2 Water injector set-up

Since a full characterization of the water spray was needed, a Phase Doppler Anemometry (PDA) was utilized in order to characterize the global shape of the analyzed injection system spray and to quantify the spray penetration and cone angle as a function of time. The schematic representation of the experimental setup is shown in Figure 11. More details could be found in [20]. Experimental characterization of the spray was carried out at Shot to Shot Engineering, a spin-off company of University of Perugia.

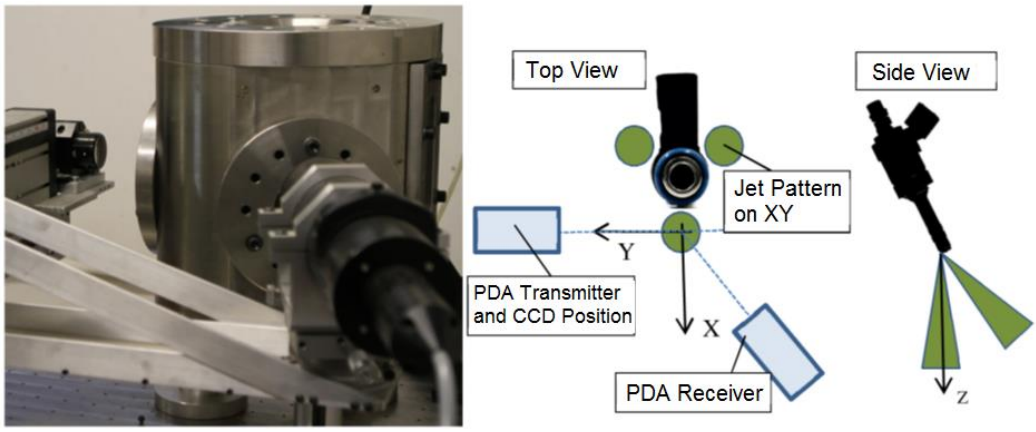

Figure 11. Test vessel used for imaging, PDA and momentum tests (left). Reference system (right)

A dINJ Injection Analyser has been used to measure the injection rate and injected mass. This instrument is currently being used for the hydraulic analysis of low pressure injection systems such as Port Fuel Injection (PFI) and Selective Catalytic Reduction (SCR). The schematic representation of the injection analyzer is reported in more details in [21] and also shown in Figure 12.

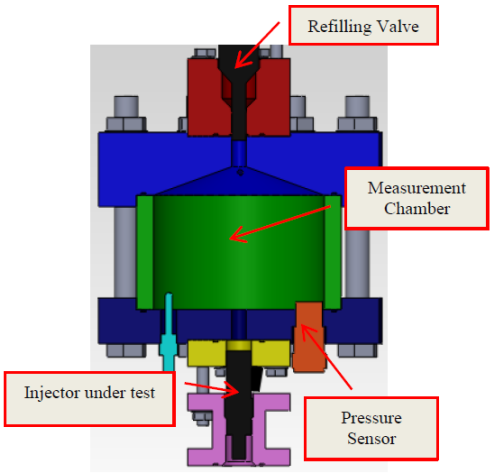

Figure 12. Schematics of the dINJ injection analyzer [21]

A closed vessel or measuring chamber acts as an isolated rail feeding the injector, that can operate against the atmosphere or any given ambient condition from vacuum to high pressure conditions. In fact, according to this scheme the detection of the downstream pressure conditions is not required for the injection rate/injected volume evaluation. The injection rate and the injected quantity measurements are based on the analysis of the pressure time-history in the measurement chamber [21].

Parte del lavoro descritto in questo capitolo è stato anche preventivamente pubblicato in:

Part of the work described in this Chapter was also previously published in the following publications:

1. F. Millo, M. Mirzaeian, S. Luisi, V. Doria, A. Stroppiana, "Engine displacement modularity for enhancing automotive s.i. engines efficiency at part load", Fuel Journal. 180 (2016) 645–652. doi:10.1016/j.fuel.2016.04.049.

Chapter 3

Engine Displacement Modularity for Enhancing Automotive SI Engines Efficiency at Part Load

3.1 Introduction

Part load operation of Spark Ignition (SI) engines is conventionally achieved by the use of a throttle to restrict the airflow into the engine; hence, allowing the quantity of fuel that is injected to be reduced, whilst maintaining a constant air-fuel ratio. However, this operation leads to a significant increase of the gas exchange or pumping work, which is one of the main reasons of the poor part load efficiency of SI engines.

One of the most widely used means to improve the part load efficiency of SI engines is the utilization of downsizing in combination with turbocharging [2]: fuel consumption and therefore CO_2 emissions are being reduced by means of engine downsizing, which allows a shift of load points towards higher loads and, as a result, towards more efficient zones of the engine map, while performance is being preserved or even enhanced despite the smaller displacement thanks to high boost levels [3].

Other technologies such as Variable Valve Actuation (VVA) and Cylinder Deactivation (CD) [22] could be effectively exploited as an alternative or in combination with downsizing and turbocharging in order to improve SI engine efficiency. Switching off a fraction (typically one half) of engine cylinders at part load is entitled as CD, which is an effective way to increase load (and therefore

efficiency) of the active cylinders, thus significantly improving part load efficiency while preserving full engine performance at Wide Open Throttle (WOT). As a result, the enclosed gas in the inactive cylinders works as a pneumatic spring which is periodically compressed and decompressed without overall pumping work [8].

Cylinder deactivation was first introduced for V8 engines by General Motors in the 80s with the title of "Displacement on Demand" [23]. This technology was then also applied to two 5.0-l V8 and 5.8-l V8 engines by Daimler in the 90s. Since the trend of automotive SI engines is nowadays going towards downsizing, this technology has been recently re-introduced in mass production [24], also in smaller engines with 4 and even 3 cylinders [25]. However, since cylinder deactivation causes lower frequency and higher amplitude torque pulsations at the crankshaft, it should be pointed out that the maximum potential fuel economy benefit may not be attained in practice due to NVH (Noise, Vibration, and Harshness) limitations [26]. Moreover, it is worth mentioning that cylinders cannot be deactivated individually, since the unequal cylinder firing intervals would cause unstable running, in other words, torque regularity should be guaranteed: hence groups of cylinders are usually being deactivated. For instance, in a 4-cylinder engine, the couples of cylinders that can be deactivated, with a firing order 1-3-4-2, are either the internal (2-3) or the external (1-4) ones. It is obvious that the adoption of this technology on a 3 cylinder engine is more challenging, since there is a need for a so called "rolling deactivation" of cylinders cycle by cycle [27].

Another strategy which is usually being utilized at part load with VVA systems is the Early Intake Valve Closure (EIVC), which allows to control the trapped air mass inside the cylinder without the need of any pressure loss across the throttle [19], [28]. However, the use of EIVC suffers from poor in-cylinder turbulence especially at low loads, which might lead to slower combustion rate and even misfiring. This weakness can be mitigated by means of the use of internal Exhaust Gas Recirculation (iEGR) that can allow significant reductions in terms of pumping losses without the need of using a significantly advanced EIVC. However, the dilution of the charge tends to adversely affect combustion stability and to increase cycle-to-cycle variations, and a proper balance between the use of internal EGR and of the advance of the EIVC has therefore to be found, in order to minimize pumping losses while preserving an acceptable combustion quality [29].

An interesting option is then the combination of CD with EIVC, since in this case the fired cylinders will be operated with a more than doubled load, and thus with less advanced EIVC and with further reduced losses, as demonstrated in [8], where fuel consumption reductions up to 16% in comparison with the conventional, throttled engine were achieved at low load, low speed (2 bar bmep, 2000 rpm).

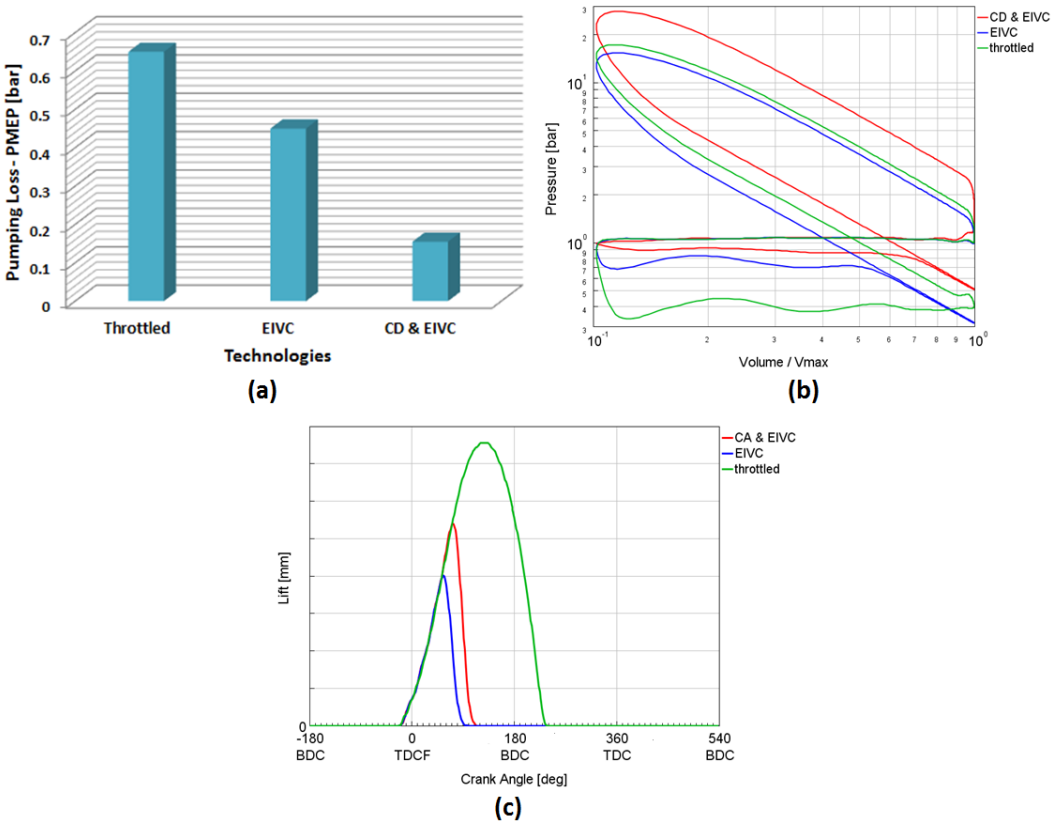

Figure 13. Different part load control strategies at 3000 rpm, 2 bar bmep: a) Pumping losses (Pumping Mean Effective Pressure PMEP); b) log p – log V diagram; c) intake valve lift profiles

An example of the benefits that can be achieved in terms of pumping losses reduction by means of EIVC and by means of EIVC combined with cylinder deactivation is shown in Figure 13-a, for a 2 bar bmep, 3000 rpm engine operating point, while the corresponding logarithmic pressure-volume diagrams and intake valve lift profiles are reported in Figure 13-b and Figure 13-c, respectively.

From Figure 13-a it can be seen that, in comparison with the conventional, throttled engine, the gas exchange or pumping work is already significantly reduced by means of EIVC only, although some residual losses still remain, due to the pressure drop occurring at small valve lifts (Figure 13-c); then, after the EIVC, the trapped charge is expanded and re-compressed, without contributing to the pumping work. Similar remarks can be made for the combination of EIVC and CD, although thanks to the increased load for the firing cylinders, the valve opening is expanded (Figure 13-c), with further reduced pumping losses, and the EIVC is more delayed, with further significant benefits in terms of charge turbulence and therefore of combustion speed and stability. CD and EIVC can therefore be combined, although achieving only a partial combination of benefits.

Although the combination of CD with a fully-variable valve train system such as the UniValve has been already quite extensively investigated [30], [31], a lack of knowledge exists about the possible combination of CD and other VVA systems such as the MultiAir, which are typically adopted on the intake side only, thus making the cylinder deactivation significantly more complex.

The aim the work described in this section is therefore the development of an innovative strategy, exploiting internal Exhaust Gas Recirculation (iEGR) in the inactive cylinders in order to minimize their pumping losses and allowing the effective combination of CD with a MultiAir VVA, without any additional component added to the exhaust valves.

3.2 Test matrix

In the current study, the investigation was focused on the comparison between the 4-cylinder mode versus the 2-cylinder mode at part load focusing on Engine B (more details can be found in Section 2.2). It is noteworthy that the engine can also be operated using 3 or 1 cylinder; however, due to drawbacks in NVH, these configurations are not discussed.

The selected operating points are listed in Table 3 including both load and speed sweeps:

- Load sweep at 2000 rpm (1, 2 and 3 bar bmep)
- Speed sweep at 2 bar bmep (1500, 2000 and 3000 rpm).

Table 3. Selected test points for displacement modularity analysis

Engine Speed [rpm]	**bmep [bar]**
1500	2
2000	1
2000	2
2000	3
3000	2

3.3 Innovative cylinder deactivation strategy

Although cylinder deactivation is generally performed by deactivating both the intake and exhaust valves, in order to seal the charge of the inactive cylinders and have them operating as pneumatic springs without pumping losses, since the MultiAir system allows keeping only the intake valves closed, a novel approach was needed in order to exploit CD.

In this approach, as far as inactive cylinders are concerned, utilization of early Intake Valve Opening (IVO) and Intake Valve Closing (IVC) close to the Top Dead Center (TDC) results in higher overlap between the intake and the exhaust valves, as shown in Figure 14. Therefore, EGR, which is produced by the active cylinders, is introduced instead of fresh air due lower in-cylinder pressure with respect to exhaust pressure close Bottom Dead Center (BDC). Afterwards, during the exhaust stroke (opened intake valves) EGR is pushed into the intake runners and again is re-entered in the inactive cylinders.

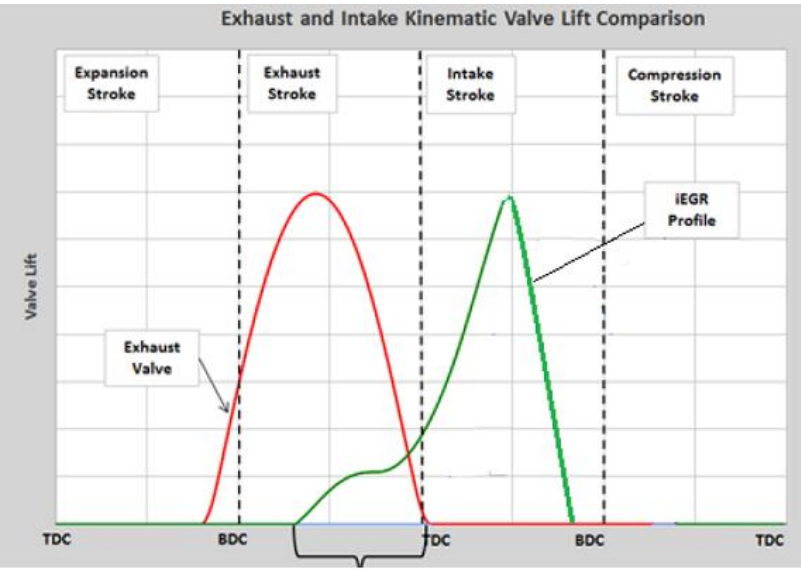

Figure 14. Exhaust and intake valve lift profiles to achieve EIVC and iEGR

Experimental analysis of inactive cylinders losses suggested that there is a compromise between the pumping and the heat losses. As it can be observed in Figure 15-a and Figure 15-c, the best trade-off between IMEPL and IMEPH, referred to Indicated Mean Effective Pressure of the Low (gas exchange stroke) and High (compression and expansion strokes) pressure portions of the engine cycle, respectively, has to be determined based on in-cylinder pressure analysis. It should be noted that for the sake of conciseness “ON” and “OFF” refers to active and inactive cylinders, respectively.

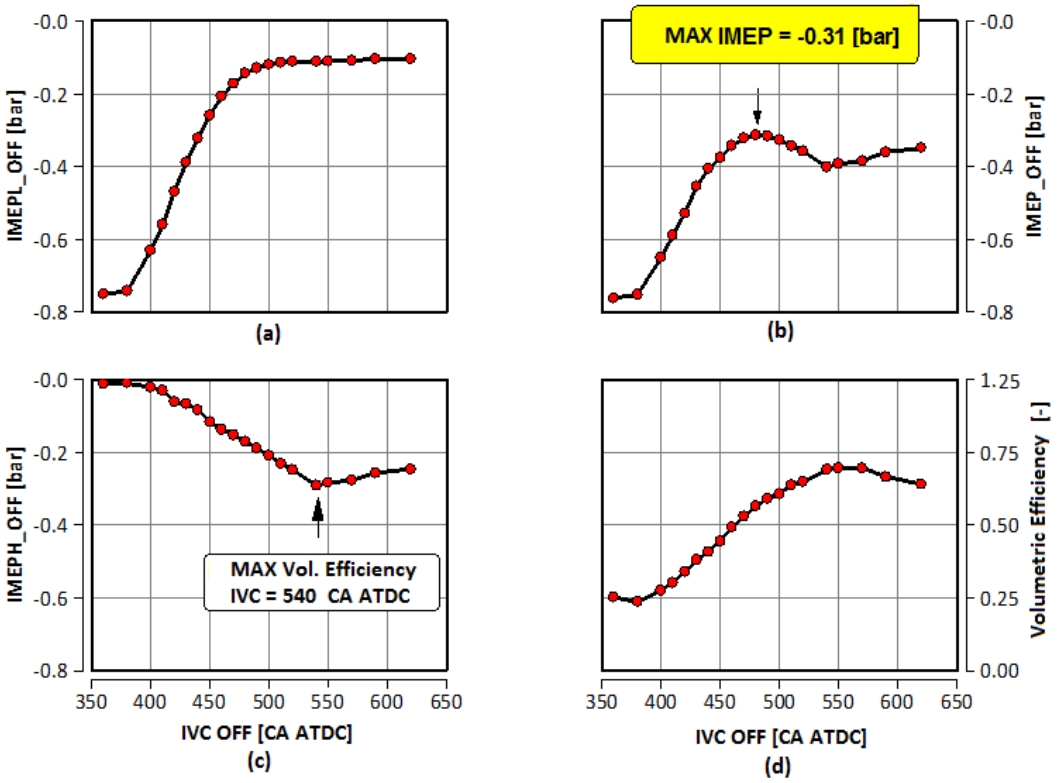

Figure 15. Effect of an IVC sweep for the inactive cylinders: a) IMEPL_OFF; b) IMEP_OFF; c) IMEPH_OFF; d) Volumetric Efficiency

3.4 Cylinder deactivation benefits

The performance of the innovative cylinder deactivation strategy were experimentally investigated for the engine operating points listed in Table 3, and the total pumping losses (i.e. the IMEPL for the whole engine) are shown in Figure 16-a in comparison with the corresponding values obtained for the 4-cylinder mode, in which all cylinders were operated with EIVC and internal EGR, which is the strategy generally adopted at part load by the MultiAir system. Moreover, the fuel conversion efficiency improvement obtained by modularity displacement with respect to 4-cylinder mode for the tested operating point has been depicted in Figure 16-b.

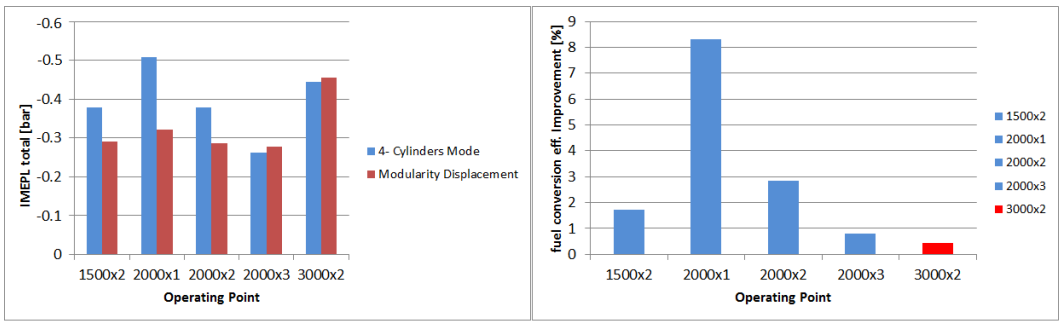

(a) (b)

Figure 16. a) Comparison of total IMEPL between 4-cylinder mode and modularity displacement for the tested operating points; b) fuel conversion efficiency improvement obtained by modularity displacement with respect to 4-cylinder mode for the tested operating point in which blue and red are showing positive and negative sign respectively

To wrap up. since the MultiAir VVA system does not allow exhaust valve deactivation, internal Exhaust Gas Recirculation (iEGR) in the inactive cylinders has been utilized in order to minimize their pumping losses.

This innovative cylinder deactivation technique was demonstrated to be effective in the low speed and low load operating region of the engine map, below 3 bar bmep and 3000 rpm, leading to a maximum reduction of pumping losses of about 30% compared to the EIVC unthrottled load control. More detail analysis regarding the possible benefits of Cylinder Deactivation strategy could be found in [7].

Parte del lavoro descritto in questo capitolo è stato anche preventivamente pubblicato in:

Part of the work described in this Chapter was also previously published in the following publications:

1. V. Doria, A. Stroppiana, M. Ferrera, F. Millo, M. Mirzaeian, D. Porcu, "Knock Mitigation Techniques for Highly Boosted Downsized SI Engines: Miller Cycle and Water Injection", in: SIA Powertrain, Versailles, France, 2017.

2. S. Luisi, V. Doria, A. Stroppiana, F. Millo, M. Mirzaeian, "Experimental Investigation on Early and Late Intake Valve Closures for Knock Mitigation through Miller Cycle in a Downsized Turbocharged Engine", in: SAE Tech. Pap. 2015-01-0760, SAE International, 2015. doi:10.4271/2015-01-0760.

Chapter 4

Knock Mitigation Techniques: Miller Cycle and Water Injection

4.1 Introduction

Different approaches are currently being explored to achieve knock mitigation in downsized, turbocharged engines at high loads [5], including the adoption of cooled EGR [10], [11], of water injection [6], of variable compression ratio (for instance through variable con rod length) [32], [4], of Miller cycle [14],[33],[34],[35],[15] and [19], the latter being achieved by reducing the effective compression ratio thanks to a shorter compression stroke and hence reaching lower charge temperatures inside the cylinder. The reduction of the effective compression ratio can be achieved through a Late Intake Valve Closure (LIVC), as shown in Figure 17, or through an Early Intake Valve Closure (EIVC).

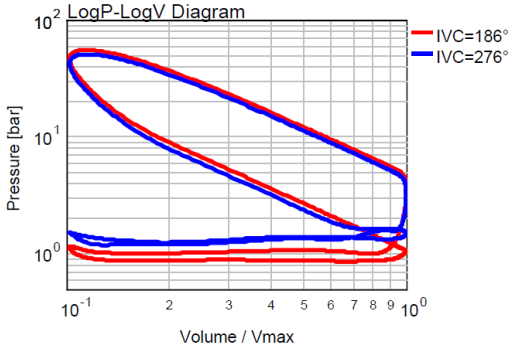

Figure 17. Comparison of a conventional SI engine cycle (red) and a Miller cycle through LIVC (blue) on a log P-log V diagram: both cycles have the same net indicated work

Moreover, although the effective compression ratio could be controlled by using both EIVC and LIVC, the former inherently reduces the level of turbulence in the cylinder, thus leading to a slower flame propagation ([36] and [18]), and may also cause poor fuel-air mixing, while the latter generally shows a less negative impact on turbulence and mixture formation. On the other hand, with the LIVC, the in-cylinder turbulence levels are preserved and the charge temperature is kept at an almost constant level; thus, guarantying a better fuel-air mixing.

Water injection is another promising technology for knock mitigation at higher load operating points. This technology is based on the utilization of high latent heat of water in order to cool down the intake charge. Moreover, thanks to increase in heat capacity of the total charge, additional temperature decrease can be achieved which results in reduction in knock tendency. The water could be injected either in the cylinder [37] or in the intake port [38]. It has been demonstrated by Hoppe et al. [12] that water injection combined with Miller cycle and cooled external EGR could lead to an efficiency increase of maximum 3.8% in the minimum Brake Specific Fuel Consumption (BSFC) region. In addition, Harrington [39] has indicated that not only knock can be mitigated by using water injection, NO_x emissions could also be reduced.

The first part of the current chapter is focused on the experimental investigation of Engine B with CR of 10 aiming to evaluate possible fuel consumption benefits of the Miller cycle thanks to its knock mitigation capability. In the second part, Engine C was considered in which compression ratio of the engine was augmented from 10 to 13 thanks to water injection strategy and the fuel consumption benefits have been evaluated at different operating points namely low, medium and high load condition.

4.2 Miller cycle

4.2.1 LIVC versus EIVC analysis

In order to confirm the superior knock mitigation effects of LIVC with respect to the EIVC strategy a preliminary experimental investigation was carried out on Engine B (more details can be found in Section 2.2).

The experimental data gathered at 19 bar bmep, 2500 rpm (hereafter referred to as 2500 x 19) which are shown in Figure 18 clearly proves the superior knock mitigation capability of the LIVC versus the EIVC. It can be clearly seen that the LIVC actuation shows the capability of running the engine with a more advanced spark timing; thus, resulting in less delayed combustion process (looking at MFB 50 in Figure 18-b), and with a leaner mixture (Figure 18-d), without exceeding the inlet turbine temperature limit, which was set at 950 °C (Figure 18-c). The better combustion phasing and the reduced need for mixture enrichment both contribute

to a better indicated fuel conversion efficiency (defined in [36]), as shown in Figure 18-a.

On the basis of these preliminary investigations, the EIVC was discarded and the research activities were then focused on the LIVC strategy only.

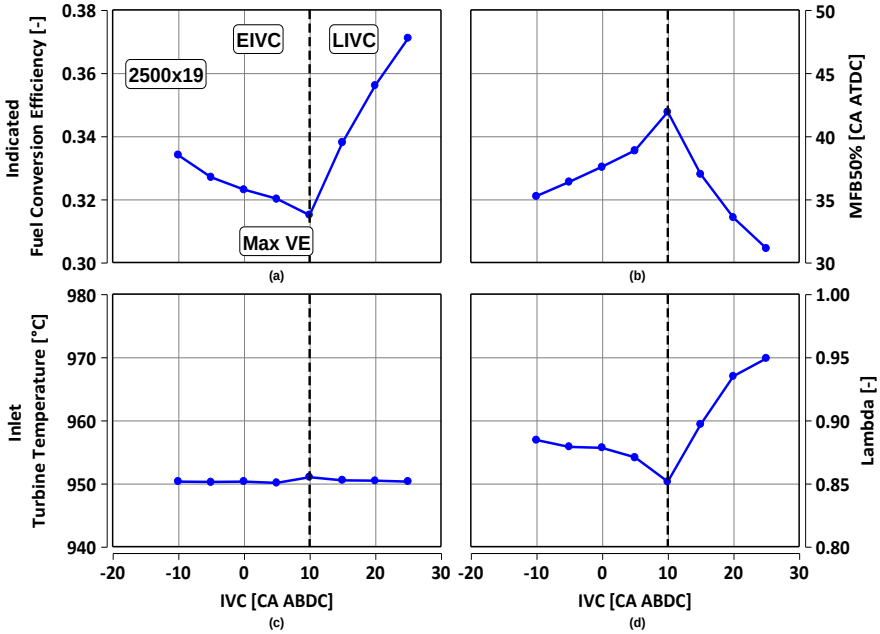

Figure 18. Effects of LIVC and EIVC at 2500 rpm x 19 bar bmep (dotted line shows IVC value corresponding to the maximum volumetric efficiency); a) Indicated fuel conversion efficiency; b) MFB50; c) Inlet turbine temperature; d) Relative air to fuel ratio (lambda)

More in detail, a preliminary 3D-CFD simulation was carried out for the intake and the compression phases considering two different valve strategy namely EIVC and LIVC (Figure 19) to support the experimental investigations.

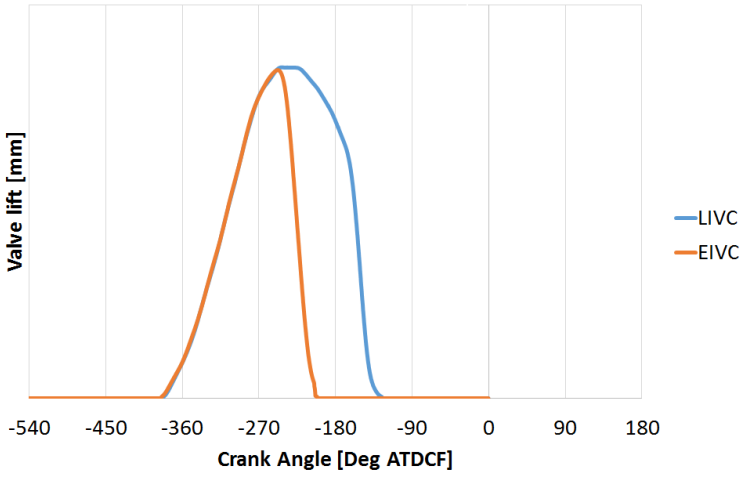

Figure 19. LIVC and EIVC lifts utilized for the 3D-CFD analysis

It is noteworthy that the time dependent pressure and temperature boundary conditions are derived from the 1-D model of the whole engine by means of GT-Power, Figure 20.

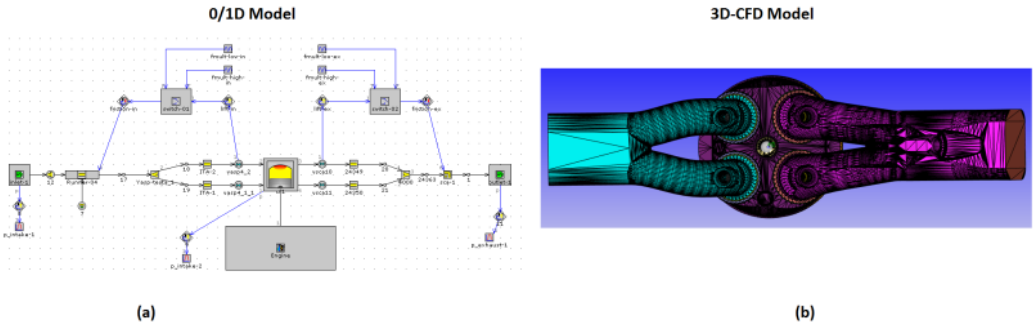

Figure 20. Sketch of the CFD models: 1D GT-Power engine simulations (a) provide the boundary conditions for the 3D-CFD calculation of the in-cylinder flow (b).

The Reynolds Averaged Navier-Stokes (RANS) turbulence model utilized in this work was the RNG (Renormalization Group) $k-\varepsilon$.

In order to have the same trapped mass inside the cylinder, it is required to increase the boost pressure in the EIVC strategy leading to higher mass flow rate and Turbulent Kinetic Energy (TKE) level in part A (Figure 21). Turbulent time scales are of the order of one millisecond such that the turbulent kinetic energy is rapidly dissipated. In part B, since in the EIVC strategy the intake valves are closed earlier, there are no sources to support the turbulence inside the cylinder after Intake Valve Closure (IVC) and the TKE decreases rapidly while in the LIVC strategy the late closure leads to higher level of turbulence near Top Dead Center Firing (TDCF).

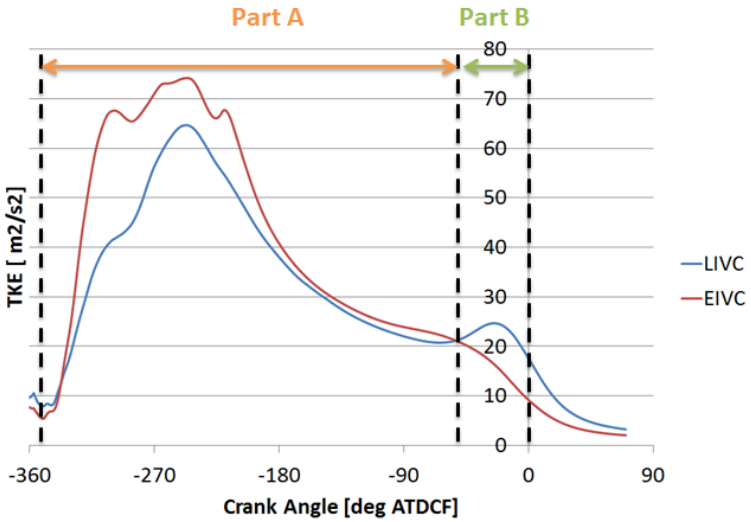

Figure 21. The comparison of the TKE between LIVC and EIVC strategies

As it can be appreciated from 2D representation of TKE for both EIVC and LIVC strategies in Figure 22 and Figure 23, higher in-cylinder TKE level in the LIVC strategy is detected.

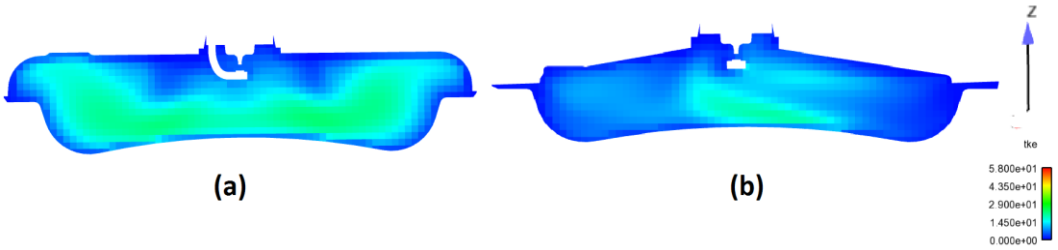

Figure 22. TKE at 5 degree before TDCF in the EIVC strategy (a) x plane (b)y plane

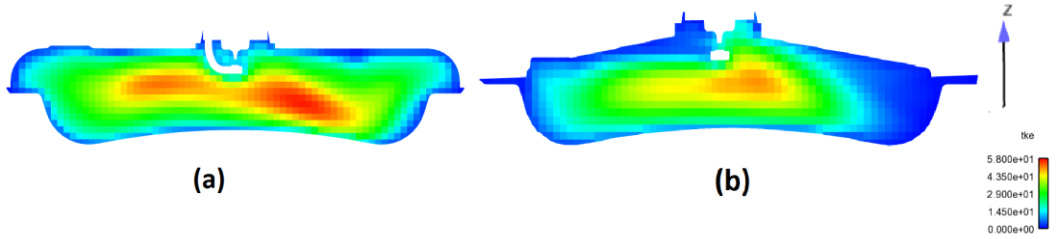

Figure 23. TKE at 5 degree before TDCF in the LIVC strategy (a) x plane (b)y plane

More in detail, the analysis has also been performed on the flow field to investigate its effect on turbulence. Considering that the destruction of tumble near TDCF is one of the main sources of turbulence at TDCF, the comparison of the tumble number for both late and early intake valve closure is depicted in Figure 24. It can be appreciated that the tumble number of LIVC strategy is higher than the EIVC case which is due to the fact that the flow through the intake valves are open to support the tumble motion.

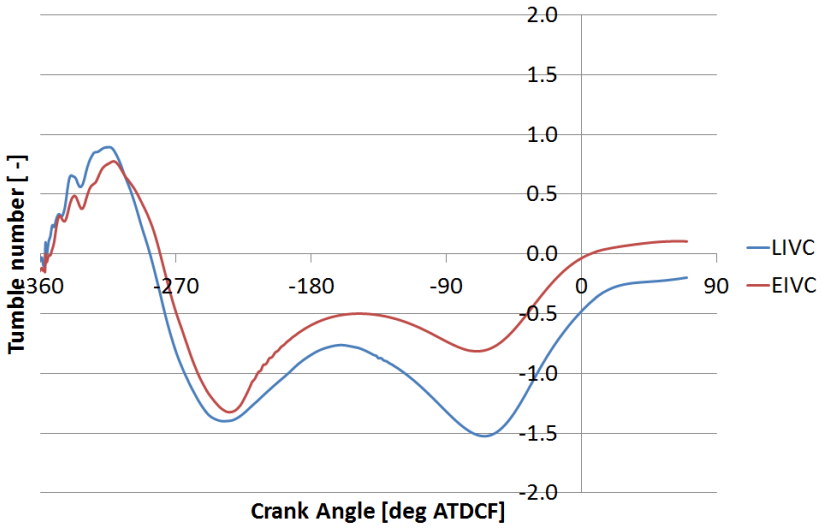

Figure 24. Comparison of Tumble number between LIVC and EIVC

The 3D visualization of the flow field for LIVC and EIVC is illustrated in Figure 25 and Figure 26, respectively. The strong tumble motion at LIVC strategy can be observed which is almost preserved during the 20 degrees crank angle, while the EIVC indicates a weak tumble motion which is due to the fact that the flow through the valves are not supporting the tumble generation.

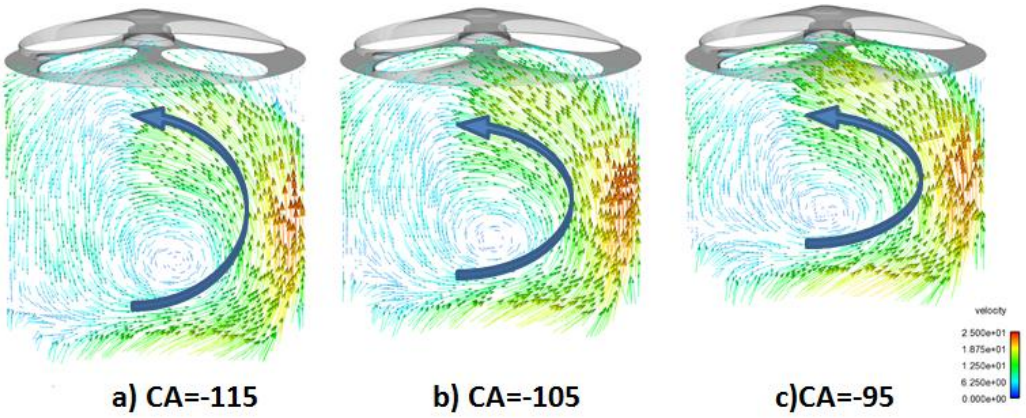

Figure 25. Velocity field For the LIVC strategy at different crank angle

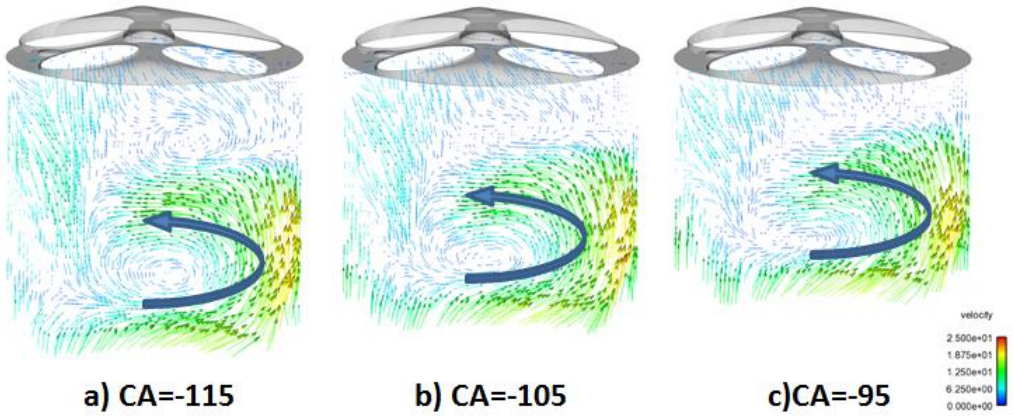

Figure 26. Velocity field For the EIVC strategy at different crank angle

4.2.2 Test matrix

After selecting the LIVC as the more promising strategy for knock mitigation, its potential was experimentally evaluated for Engine B (Section 2.2) on a test matrix of 22 engine operating points, as shown in Figure 27, including:

- Load from 14 to 20 bar bmep
- Speed from 1750 rpm to 5000 rpm

For each engine operating point, the indicated fuel conversion efficiency benefit versus the standard Normal Production (NP) cam profile that could be

achieved by exploiting the knock mitigation potential was assessed, without exceeding limits reported in Table 4.

Table 4. Limitations for the test matrix of LIVC analysis, Engine B

Parameter	**Unit**	**Limit**
Turbocharger angular speed	[rpm]	240 000
Inlet turbine temperature	[°C]	950
Outlet intercooler temperature	[°C]	Fixed at 50
Peak cylinder pressure	[bar]	85
Absolute boost pressure	[mbar]	2500
Spark Advance	-	knock limited at trace level

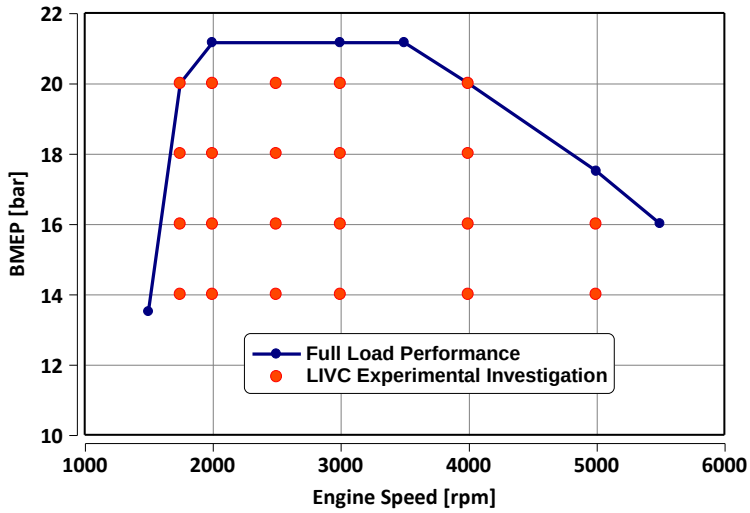

Figure 27. Experimental investigation test matrix for LIVC strategy

4.2.3 Results and discussion

The benefits that could be achieved by means of LIVC in terms of improvements of indicated fuel conversion efficiency referred to the values corresponding to the NP cam profile settings are shown in Figure 28.

As it can be observed, impressive efficiency enhancements (up to 20%) could be achieved at medium speeds and high loads (e.g. at 3000 rpm, 20 bar bmep), since in this region of the engine operating map the turbocharger is capable of providing a sufficient boost pressure to compensate for the reduced volumetric efficiency caused by the LIVC, thus, allowing the full exploitation of its knock mitigation

capability. On the other hand, although knock limitations are generally more severe at lower speeds, (such as 1750 and 2000 rpm), in this region the turbocharger is not capable to provide boost levels suitable to support extreme late IVCs, therefore, leading to an only marginal exploitation of the LIVC knock mitigation potential and as a result to lower efficiency gains in these conditions. Accordingly, at 2000 rpm, efficiency improvements (1.4% and 2.7 % respectively) could be obtained only at lower loads (14 and 16 bar bmep), while at higher loads (18 and 20 bar), the IVC could not be further delayed with respect to the NP settings, due to lack of boost, and no efficiency gains could be gathered. The same happened for all the investigated loads at 1750 rpm.

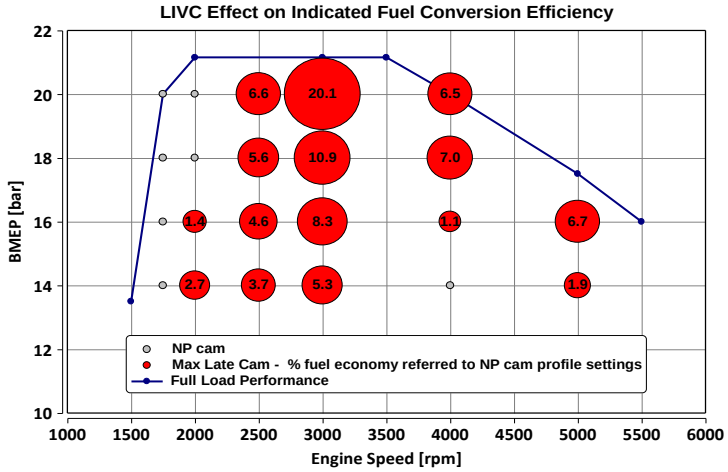

Figure 28. LIVC effects on indicated fuel conversion efficiency (% benefits referred to NP cam profile settings)

On the contrary, the LIVC strategy starts to be more efficient at higher speeds, 2500 rpm, with the benefits ranging from 3.7% to 6.6% at different loads. However, at 3000 rpm x 18 bar bmep and 3000 rpm x 20 bar bmep, the highest efficiency advantages are achieved around 20.1% and 10.9 %, respectively due to the possibility to operate the engine at stoichiometric conditions, without the need of mixture enrichment; that was on the contrary mandatory for the NP cam settings, in order to keep the turbine inlet temperature below the 950°C limit.

At 4000 rpm the benefits due to the LIVC strategy, although still important, started to decline, since the knock likelihood is partially mitigated by the augmented engine speed: in particular, at lower loads, i.e. at 14 and 16 bar bmep, no or only marginal (1.1%) benefits were achieved, since with the NP cam settings there was no need to significantly retard the combustion phasing in order to avoid knock occurrence. At higher loads instead, i.e. at 18 and 20 bar bmep, the knock mitigation provided by the LIVC allowed the engine operation with a significant decrease of mixture enrichment, thus, leading to relevant efficiency enhancements, equal to 7% and 6.5 %, respectively.

Identical observations apply to the highest revolution speed under investigation, 5000 rpm, for which the exhaust temperature control is the most critical issue to be addressed: important improvements could be achieved only at 16 bar bmep, thanks again to a significant decrease of mixture enrichment. In order to more clearly understand the mechanisms through which the LIVC allowed the achievement of the abovementioned efficiency gains, further analysis was carried out on all the engine operating points under investigation. However, for the sake of brevity, only one engine operating point, namely 3000 rpm x 20 bar bmep, will be discussed more in details hereafter, being representative, of the maximum exploitation of the knock mitigation effect which could be obtained by means of LIVC.

The effects of LIVC at 3000 rpm x 20 bar bmep are reported in Figure 29, Figure 30 and Figure 31. As one can see from Figure 29-a, the engine can be operated with a delayed IVC of 90 CA After Bottom Dead Center (ABDC); thus, achieving a 20% improvement of indicated fuel conversion efficiency with respect to NP cam configuration, thanks to the high boost pressure availability (Figure 29-d), which allows to compensate for the decreased volumetric efficiency (Figure 29-b), while still reaching the bmep target level (Figure 29-c). Moreover, the increase in the boost pressure significantly improves the efficiency of the gas exchange process, raising the Low pressure IMEP (hereafter referred to as IMEPL) of about 0.2 bar, as shown in Figure 30-a. Furthermore, thanks to the knock mitigation effect, the combustion phasing can be advanced by 9 CA (the MFB 50 can be moved from 33 to 24 CA After Top Dead Center (ATDC), Figure 30-c), and the mixture enrichment can be reduced up to stoichiometric conditions (Figure 30-b). Despite the mixture enleanment, the more advanced combustion phasing leads to a more stable process, with a substantial reduction of the Coefficient of Variation (COV) of the IMEP (Figure 31-a), and without significant worsening of the burn durations (Figure 31-b). Finally, it is worth to be pointed out that further delays of the IVC beyond 90 CA ABDC would not be possible, since the target bmep level could no more be reached (Figure 29-c), due to an insufficient boost pressure. In conclusions, for this operating point, the impressive enhancement of the indicated fuel conversion efficiency is to be attributed primarily to the mixture enleanment, then to the better combustion phasing, and only marginally to the improvements of the gas exchange phase.

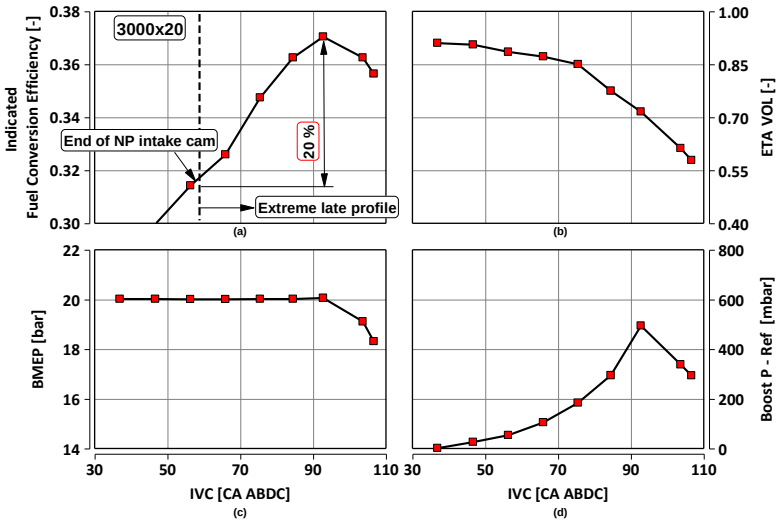

Figure 29. LIVC effects on: a) indicated fuel conversion efficiency; b) volumetric efficiency; c) bmep; d) boost pressure referred to the value corresponding to the maximum volumetric efficiency – 3000 rpm x 20 bar bmep.

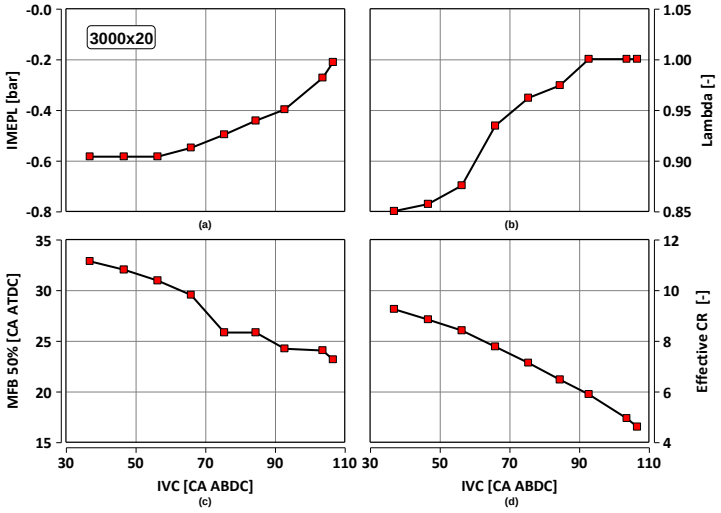

Figure 30. LIVC effects on: a) IMEPL; b) lambda; c) MFB50; d) effective compression ratio - 3000 rpm x 20 bar bmep.

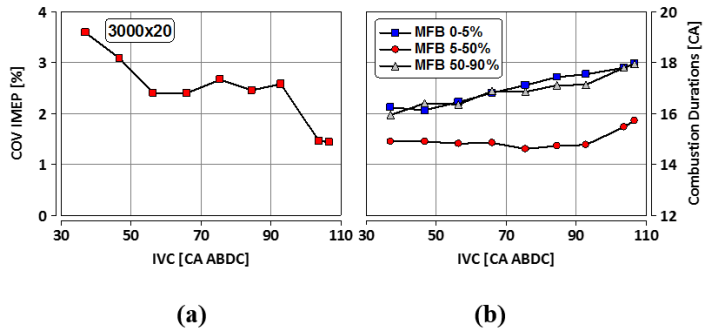

Figure 31. LIVC effects on COV of IMEP (a) and combustion durations (b) - 3000 rpm x 20 bar bmep

4.3 Water injection

4.3.1. Test matrix

The investigation has been carried out on Engine C considering CR10 and CR13. First, the whole map of Engine C has been experimentally investigated considering Miller cycle with CR10. Afterwards, CR of the engine C was augmented from 10 to 13 while the WI technology has been combined with Miller cycle in order to understand the additional fuel consumption benefits of WI at different operating points. Thanks to the WI for knock mitigation and augmented CR, fuel economy could be improved at low medium and high load condition. Three main zones of the engine map which have been analyzed experimentally are shown in Figure 32 [6,40].

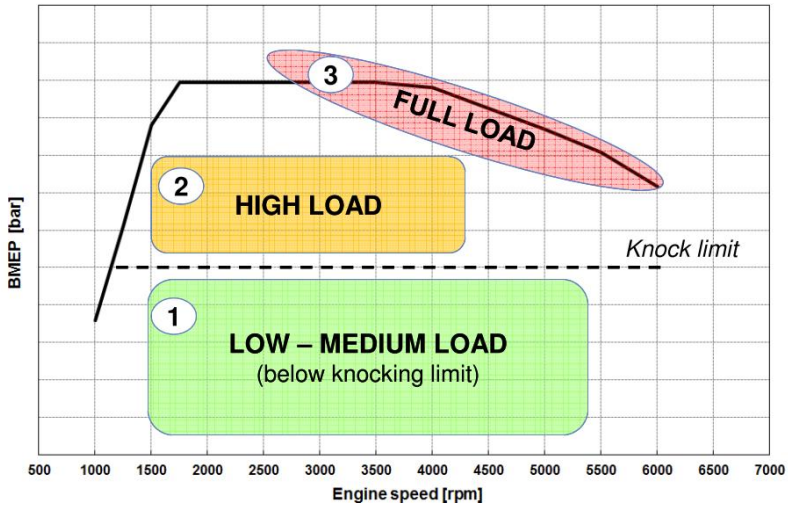

Figure 32. Different zones experimentally investigated at CR10 and CR13 for water injection analysis [40]

4.3.2 Experimental analysis

As it was already pointed out in the previous sections, thanks to knock mitigation potential obtained by water injection, the compression ratio could be increased from 10 to 13. The comparison between CR10 and CR13 in terms of BSFC reduction is illustrated in Figure 33. At higher loads, thanks to the augmented compression ratio and water injection, the BSFC has been reduced by maximum 4%. At lower loads in which knock is not probable, the water injection technology is not being utilized; however, the augmented compression ratio leads to a maximum BSFC reduction of 4.5%.

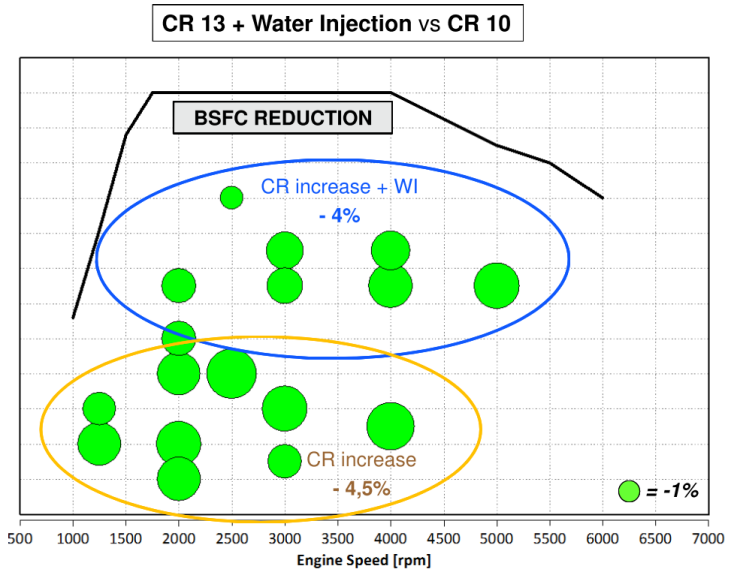

Figure 33. Comparison of CR10 and CR13 configuration at different speeds and loads

Further analysis was performed at each engine operating point, and for sake of brevity, two engine operating points, 2000 rpm x 13 bar bmep and 4000 rpm x15 bar bmep, are presented in Figure 34. It can be realized that combustion phasing is improved thanks to water injection allowing advancement of the spark timing. It is important to note that about 3% and 4% of BSFC reduction at 2000 rpm x 13 bar bmep and 4000 rpm x 15 bar bmep are registered with respect to CR10 configuration, respectively.

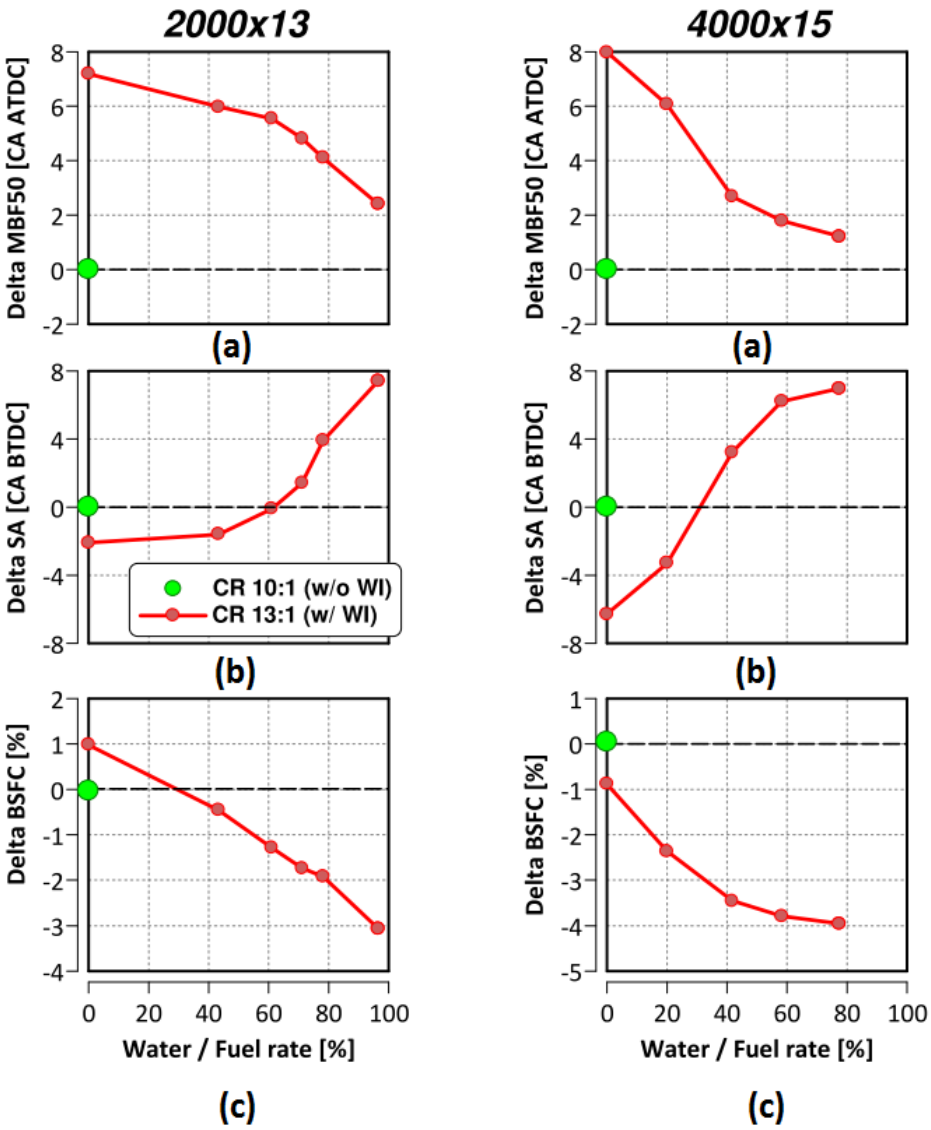

Figure 34. a) Delta MFB50; b) Delta MFB50; c) Delta BSFC as a function of water to fuel percentage at 2000 rpm x 13 bar bmep and 4000 rpm x 15 bar bmep

The full load performance of the engine at 2500, 3000 and 5500 rpm has been also investigated. It can be seen from Figure 35 that the water injection technology allows to use CR13 with limited penalties on performance.

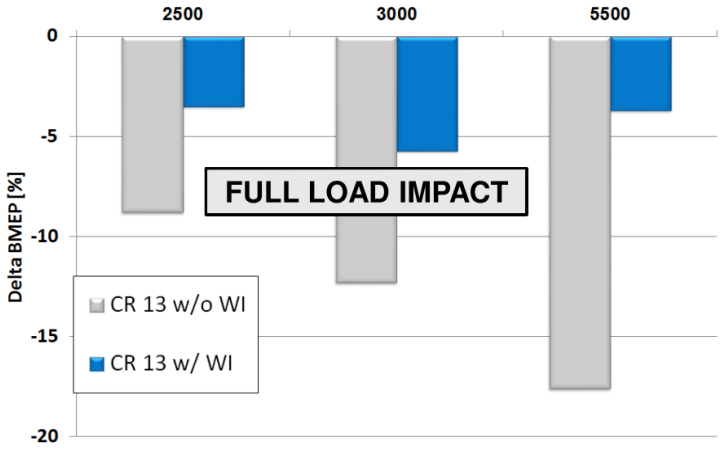

Figure 35.Delta bmep with respect to CR10 configuration at full load

The combustion phasing and delta power changes are depicted in Figure 36. It can be appreciated that the delta bmep percentage with respect to CR10 is decreased from about 17% (no water injection) to 4% (using around 40% water injection) which indicates limited impact on the performance when water injection is utilized.

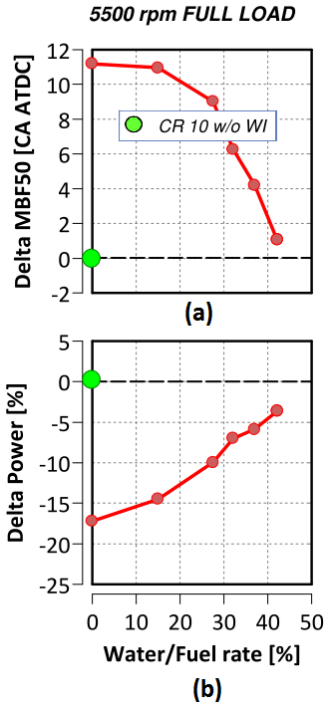

Figure 36. a) Delta MFB50; b) delta power as a function of water to fuel rate percentage

4.3.3 Further development of water injection configuration through 3D-CFD

Although, the potential knock mitigation of WI strategy was confirmed through a detailed experimental study, the water injection configuration could be further optimized through a preliminary 3D-CFD analysis aiming to fully exploit the possible benefits of this technology. It has been observed that phasing and spray targeting of the injector have significant effect on the water evaporation and on the impingement on the cylinder liner; therefore, a mini Design of Experiment (DoE) was performed in order to find the best phasing and spray targeting.

4.3.3.1 Engine model setup

3D-CFD simulations were carried out in cold flow conditions for the intake and compression phases engine operating point (4000 rpm x 17 bar bmep). The base grid was set to 4 mm, with additional mesh refinements up to a local grid size in the order to 0.5 mm during the gas-exchange process. The total number of cells at TDC was equal to 500’000. It is noteworthy that the time dependent pressure and temperature boundary conditions are derived from the 1D model of the whole engine by means of GT-Power.

4.3.3.2 Spray model

In order to accurately model the water injection phenomenon, it is important to have a model which is capable to accurately predict the spray break-up and penetration. The experimental measurements reported in Section 2.3.3, which were carried out in a pressurized vessel at the same pressure of the intake manifold, have been used to refine the spray model. The schematic representation of the geometry of the pressurized vessel is shown in Figure 37. The base grid was set to 2 mm, with additional mesh refinements up to a local grid size in the order of 0.5 mm for the injector.

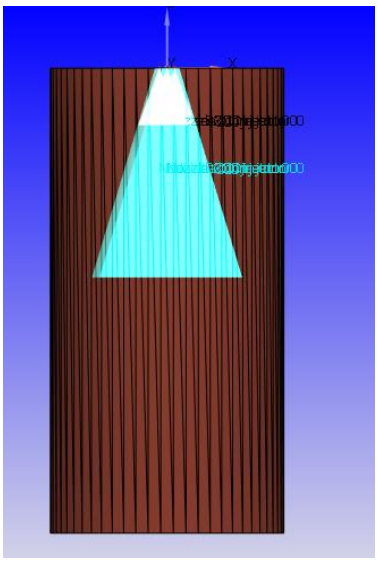

Figure 37. Sketch of the 3D CFD model of vessel

The Reynolds Averaged Navier-Stokes (RANS) turbulence model utilized in this work was the RNG (Renormalization Group) $k-\varepsilon$.

The Kelvin-Helmholtz - Rayleigh-Taylor (KH-RT) breakup length model has been used in the current work. In the KH model, the atomization process of the relatively large injected blobs is modeled using the stability analysis for liquid jets. In addition to the KH breakup mechanism [41], the RT instability is also believed to be responsible for droplet breakup. The unstable RT waves are thought to occur due to the rapid deceleration of the drops from the magnitude of the drag force. In this model, a breakup length L_b is specified as expressed in Equation 1:

$$L_b = C_{bl}\sqrt{\frac{\rho_l}{\rho_g}}d_{noz} \tag{1}$$

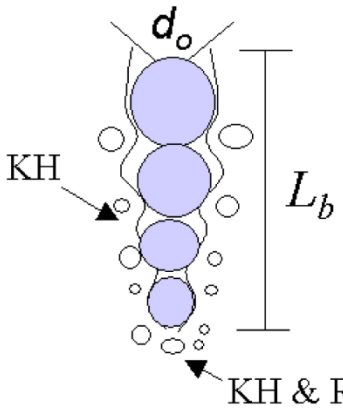

Figure 38. Schematic of the KH-RT spray breakup model

This model assumes that only KH instabilities are responsible for drop breakup inside of the characteristic breakup distance, L_b, while both KH and RT mechanisms are activated beyond the breakup length.

The Rosin-Rammler distribution was used to obtain injected drop sizes [42,43]. The cumulative probability function for the Rosin-Rammler distribution is given by:

$$\tilde{R} = 1 - \exp(-\zeta^q) \qquad 0 < \zeta < \zeta_{max} \tag{2}$$

where q is a calibration parameter:

$$\zeta = \frac{r}{\bar{r}} \tag{3}$$

$$\bar{r} = \Gamma(1 - q^{-1})\, r_{23} \tag{4}$$

where Γ is the gamma function and r_{23} is the Sauter mean radius. Once a value of ζ is selected, the injected drop radius is determined from:

$$r = \bar{r}\,\zeta = \Gamma(1 - q^{-1})\mathrm{r}_{23}\zeta \tag{5}$$

The next step is dedicated to the calculation of injection pressure and velocity. The total area of the nozzles for an injector is given by:

$$A_{tot} = \frac{\pi d_{noz}^2}{4} n_{noz} \tag{6}$$

Where $num_{noz}$and d_{noz} are number and diameter of the nozzles, respectively. The injection rate (Figure 39) is given as an input and the mass of injection during each interval ($dm_i^{rateshape}$) is given by:

$$dm_i^{rateshape} = \frac{\psi_i^{rateshape} + \psi_{i-1}^{rateshape}}{2} dt_i^{rateshape} A_{tot}\rho_l \tag{7}$$

Where $dt_i^{rateshape}$ is the time interval between two rate-shape entries and ρ_l is the liquid spray density. The rate-shape entries are given by $\psi_i^{rateshape}$, in which the units are assumed as velocity [m/s]. hence, the real velocities are calculated by:

$$v_{inj} = \frac{mass_{inj}}{\sum_{i=1}^{n} dm_i^{rateshape}} \psi_i^{rateshape} \tag{8}$$

The injection pressure is calculated as:

$$P_{inj} = \frac{1}{2}\rho_l \left(\frac{v_{inj}}{C_d}\right)^2 \quad (9)$$

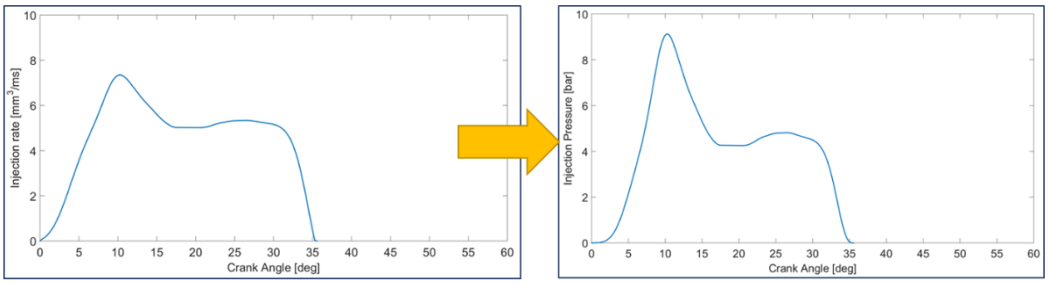

Figure 39. a) Injection rate; b) injection pressure

It is noteworthy that the discharge coefficient has been set such that the maximum injection pressure does not exceed the injection pressure reported the experiment. Finally, the new injection velocity is calculated as:

$$C_a = \frac{C_d}{C_v} \quad (10)$$

$$v_{inj,new} = \frac{v_{inj}}{C_a} \quad (11)$$

Where C_v and C_a are the velocity and contraction coefficients, respectively.

4.3.3.3 Spray model results

The comparison between the simulated and experimental spray penetration is shown in Figure 40. It can be seen that simulated and experimental penetrations are in good agreement, both in the transient and steady state part of the spray.

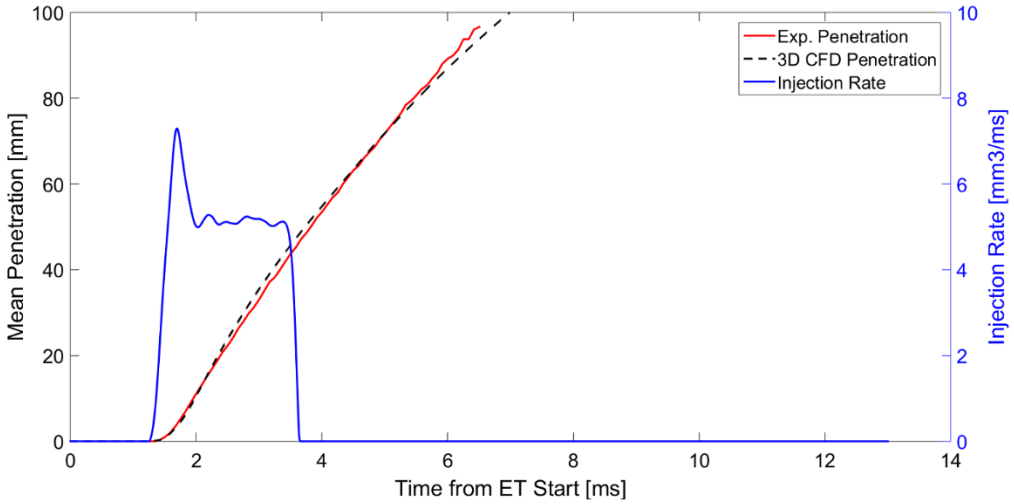

Figure 40. Comparison between experimental and simulated spray penetration

The experimental Sauter Mean Diameter (SMD) of the water droplets has been measured at two different distances from the spray tip, namely 50 mm and 90 mm. The measurement locations are in the x traverse as shown in Figure 41. Comparing the SMD values at $z = 50\ mm$ (blue line) and $z = 90\ mm$ (red line) from Figure 41, it can be observed that SMD increases as the distance from the injector tip increases which is due to the fact that larger particles have enough momentum to move forward, while the smaller ones are being broken up and stopped by the drag of the flow.

More in detail, the simulated and experimental visualization of the spray (as shown in Figure 42 after 3 ms from energizing time start, and Figure 43 after 6 ms from energizing time start) confirms that larger particles could travel a larger distance from the injector tip.

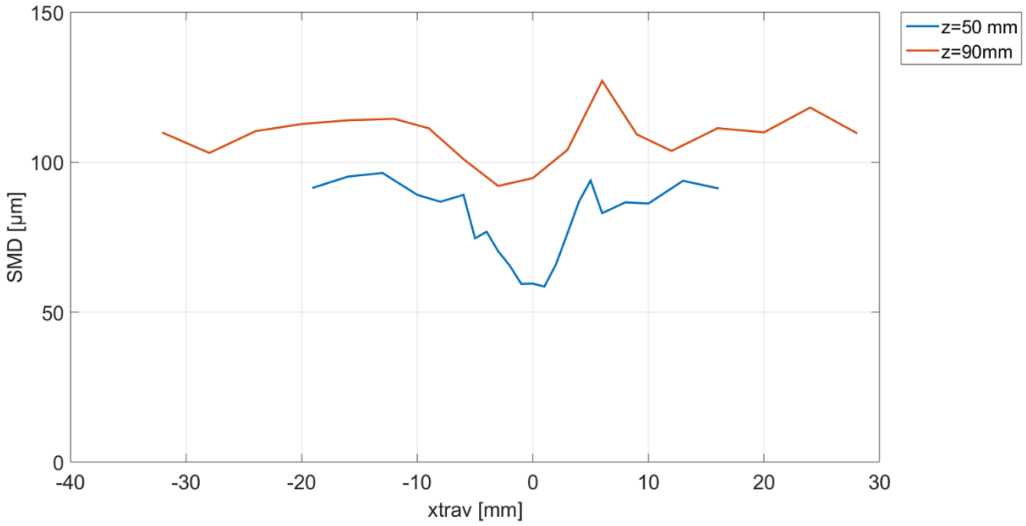

Figure 41. SMD values at different stations at z=50 mm and z=90 mm

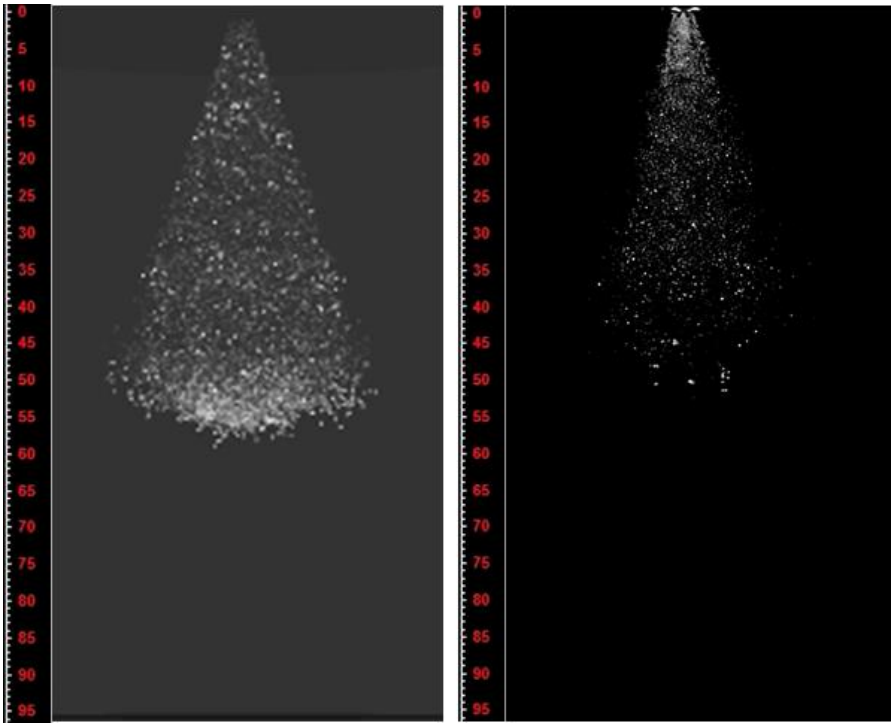

Figure 42. Comparison between experimental and simulated spray shape in the vessel after 3 ms

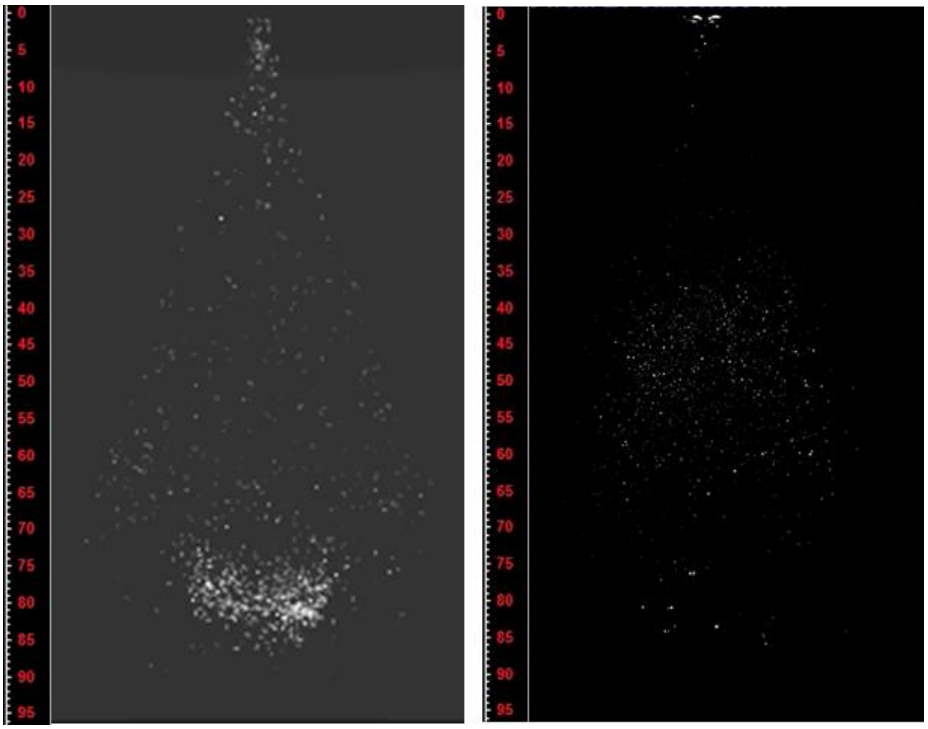

Figure 43. Comparison between the experimental and simulated spray shape in the vessel after 6 ms

In order to calculate average SMD from experimental measurements, the weighted average based on the number of particles in each station has been calculated which is written as Equation 12:

$$SMD_{meas,ave} = \sum_{i=1}^{N} \frac{n_i SMD_i}{\sum n_i} \qquad N = \#\ of\ stations \tag{12}$$

The SMD estimated from 3D-CFD can be calculated using a box as shown in Figure 44. The SMD of particles which are present in the box are calculated at each time as shown in Figure 45 (denoted by SMD_{sim} in Equation 13). The average simulated SMD (shown by $SMD_{sim,ave}$ in Equation 13) can be obtained by integrating the time dependent SMD from t_{start} to t_{end}=20 ms, shown in Equation 13.

$$SMD_{sim,ave} = \frac{1}{t_{end} - t_{start}} \int_{t_{start}}^{t_{end}} SMD_{sim}\, dt \tag{13}$$

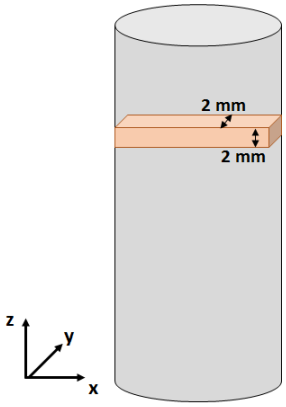

Figure 44. Defined box in the 3D-CFD domain aiming to calculate SMD

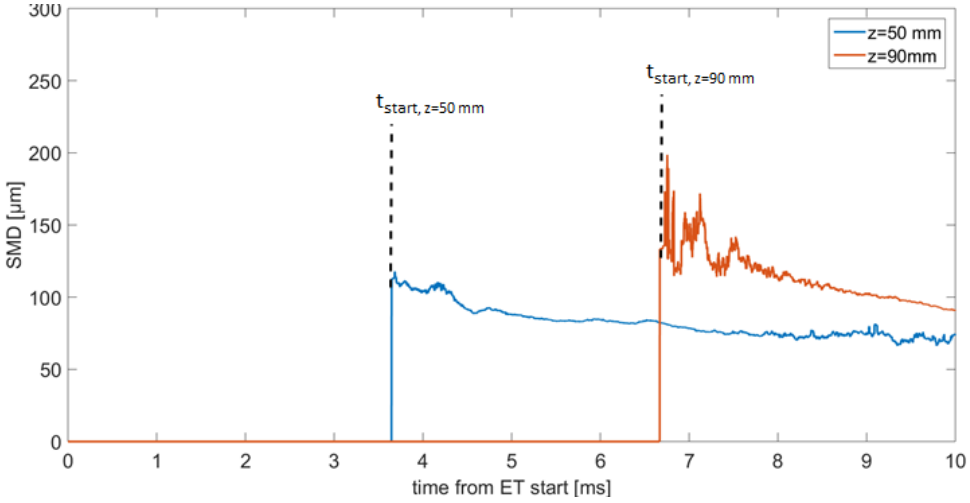

Figure 45. SMD at z=50 mm and z=90 mm as a function of time (based on 3D-CFD)

A comparison between simulated and measured average SMD is shown in Figure 46. The trend is well captured by the model and the matching is acceptable, showing slight overestimation by the model.

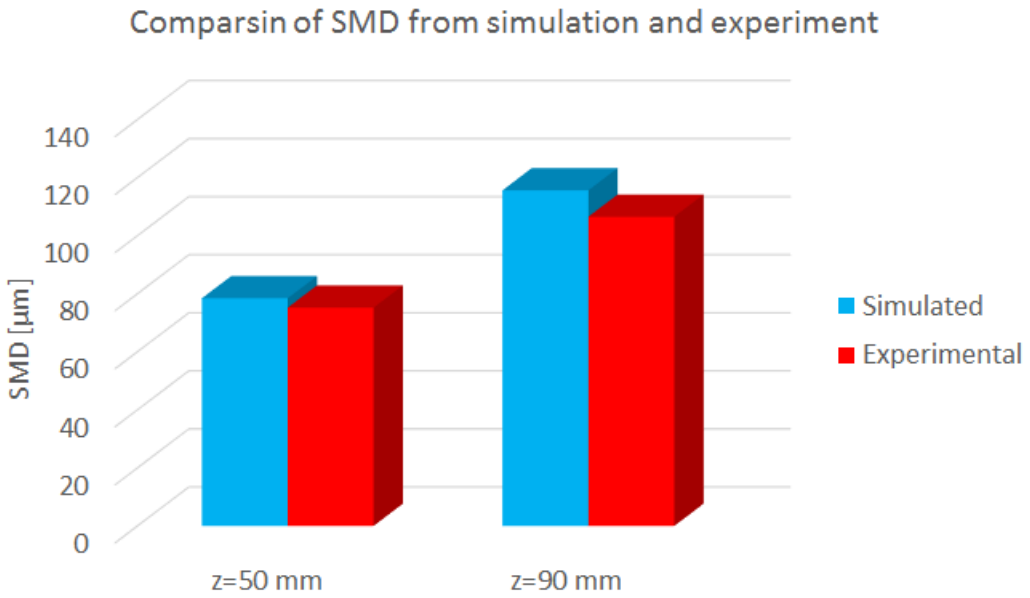

Figure 46. Comparison between simulated and measured SMD at z=50 mm and z=90 mm (measured from tip of the injector)

4.3.3.4 Engine model results

After the calibration of the 3D-CFD injector model, the model can be integrated with the engine model to further evaluate the effectiveness of water injection. Three different configurations can be considered in terms of spray targeting, as shown in Figure 47, including:

- Counter flow: in which the water is injected on the opposite direction of the intake charge, shown in Figure 47-a
- Parallel flow: in which the water injection is in the same direction of the intake charge, shown in Figure 47-b
- Perpendicular (vertical): in which the water is injected perpendicular to the direction of the intake charge, shown in Figure 47-c

It is worth mentioning that the standard configuration which is tested in the test rig is the parallel flow one.

In addition to the abovementioned configurations in terms of spray targeting, different phasing for the End of Injection (EOI) can also be considered: 360 and 450 °. As an example, the injection rate for EOI 360 and 450 ° is depicted in Figure 48. It can be observed that when EOI 360° is used (purple curve), the intake valve

starts to open at end of injection, while for the EOI of 450° the intake valve is open during whole water injection duration.

Therefore, a mini DoE was performed in order to find the best phasing and spray targeting for each configuration.

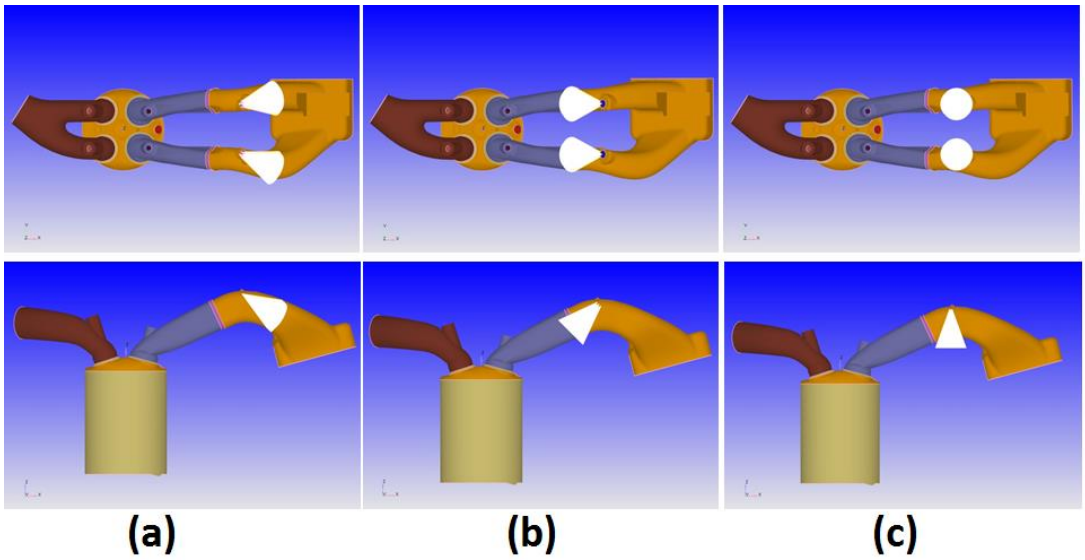

Figure 47. Schematic representation of different spray targeting: a) counter flow; b) parallel flow; c) perpendicular configuration

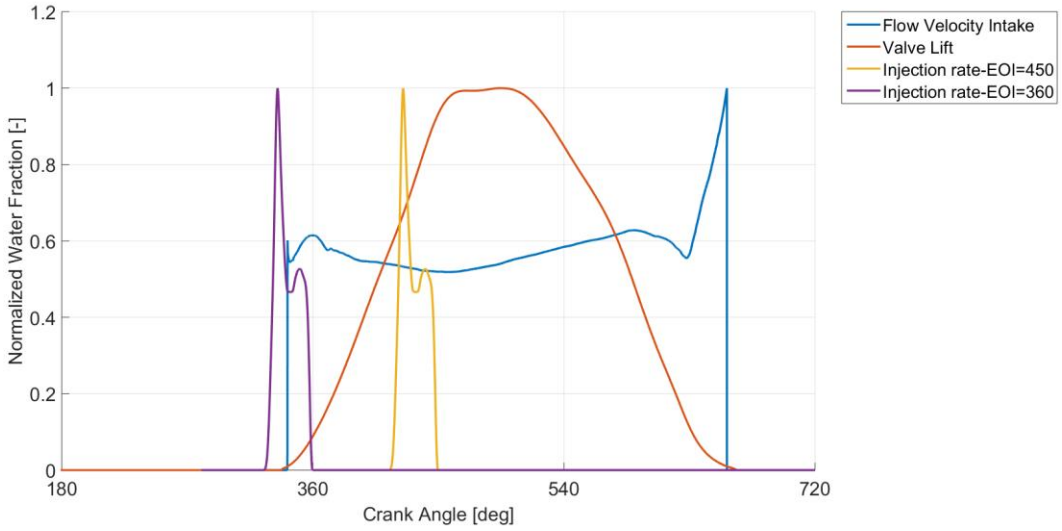

Figure 48. Injection rates at EOI of 360 and 450°C

As an example, the 3D-CFD visualization of water and fuel particles at different crank angles using parallel flow configuration and EOI of 360° is shown in Figure 49. As it can be observed from the 3D-CFD visualization, a portion of water remains in the film at the intake port after IVC timing which will not contribute to the knock mitigation effect.

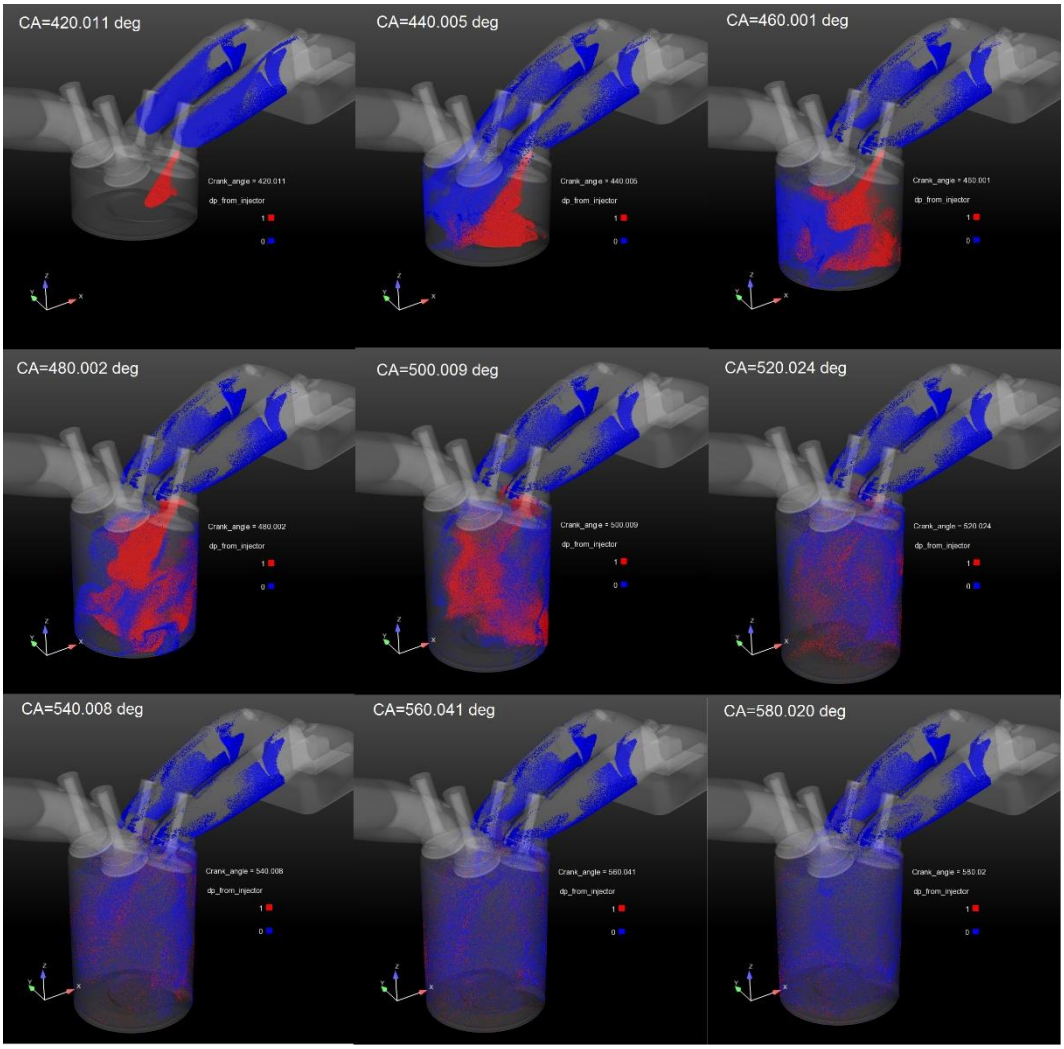

Figure 49. The visualization of water (blue) and fuel (red) particles at different crank angles with the standard configuration (parallel flow) and EOI=360 degrees

More in detail, it is important to understand how the water is distributed (in terms of evaporation, liquid particles in the charge and impingement on the wall) inside the cylinder and intake region. Therefore, for the sake of brevity, water distribution for the parallel flow configuration using EOI of 360° is shown in Figure 50 and Figure 51 in the cylinder and intake region, respectively in which:

- Gas phase: referred to the evaporated water in the flow
- Liquid phase: referred to the amount of liquid in the flow regime
- Film: referred to the amount of water sticking to the wall

It can be observed from Figure 50 that the maximum amount of water evaporated inside the cylinder is around 50% and there is still some amount water in the liquid form at IVC. Moreover, in the intake region (Figure 51), around 20%

of the water is in the film portion at the IVC timing and the rest of the water is in the gas phase, while a small portion is in the liquid phase.

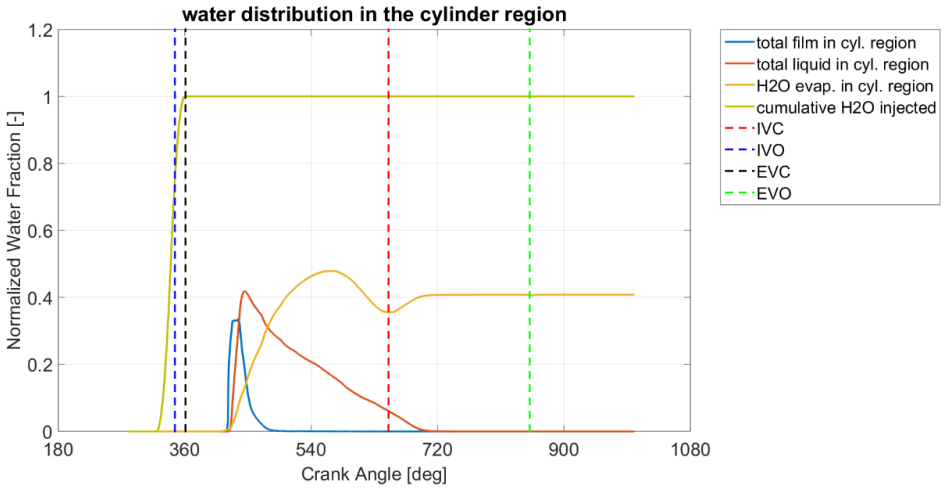

Figure 50. Water distribution in the cylinder region for the parallel configuration, EOI=360 degrees

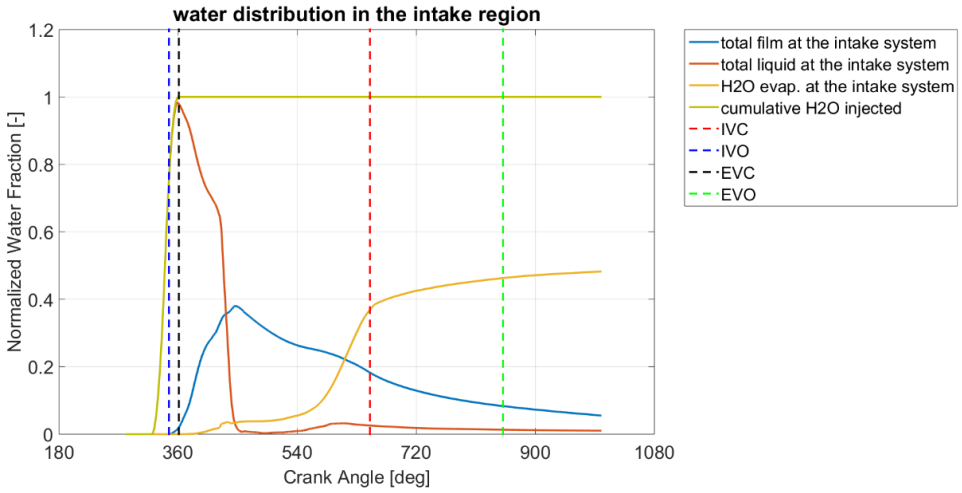

Figure 51. Water distribution in the intake region for the parallel configuration, EOI=360 degrees

However, in order to numerically evaluate the effectiveness of different configurations and phasing, two indexes, $Index_1$ and $Index_2$, have been defined as reported in Equation 14 and Equation 15, respectively. $Index_1$ (index of water evaporation) aims to evaluate how effective is the water injection in terms of charge air cooling, by comparing the amount of water which is evaporated with the total amount of water injected, while $Index_2$ (index of liner dilution) aims to evaluate the effect of water on diluting the lube oil on the liner.

$$Index_1 = \frac{Instantaneous\ water\ evaporated}{total\ water\ injected} \tag{14}$$

$$Index_2 = \frac{Integral\ of\ the\ water\ film\ on\ liner}{maximum\ water\ evaporated\ inside\ cylinder} \tag{15}$$

It can be observed from Figure 52 that the evaporation index is maximized using vertical configuration and EOI=360 degrees. The superior characteristic of the vertical configuration is confirmed in Figure 53 for EOI=450 degrees. In addition, the effect of phasing is shown in Figure 54 which indicates that the EOI of 360 degrees improves the water evaporation.

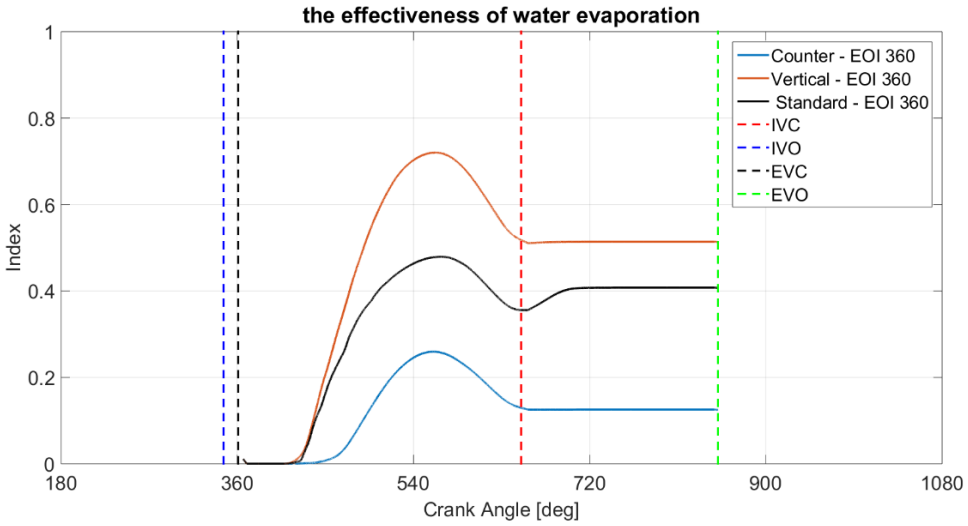

Figure 52. The comparison of the index of evaporation for different configuration with EOI=360 degrees

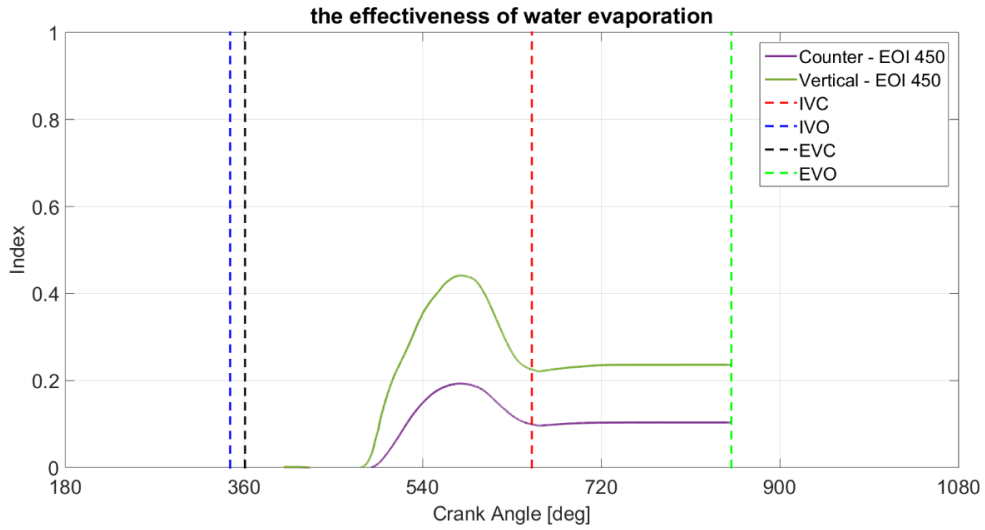

Figure 53. The comparison of the index of evaporation for different configuration with EOI=450 degrees

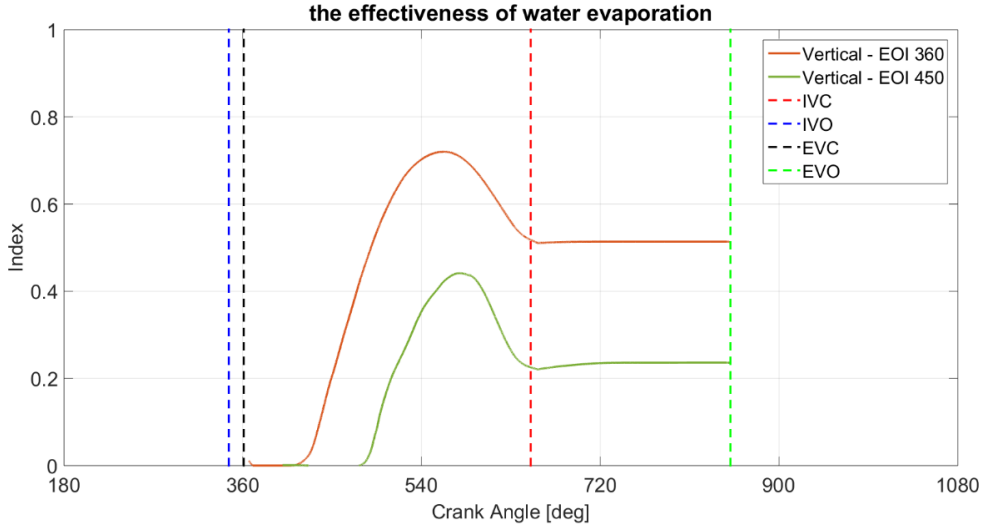

Figure 54. The comparison of the index of evaporation for vertical configuration and different EOIs

Considering the effect of different configurations and phasing on index of dilution (Figure 55, Figure 56 and Figure 57), it can be observed that counter and vertical configurations with the EOI of 360 degrees have the lowest value which indicates lower liner dilution effect.

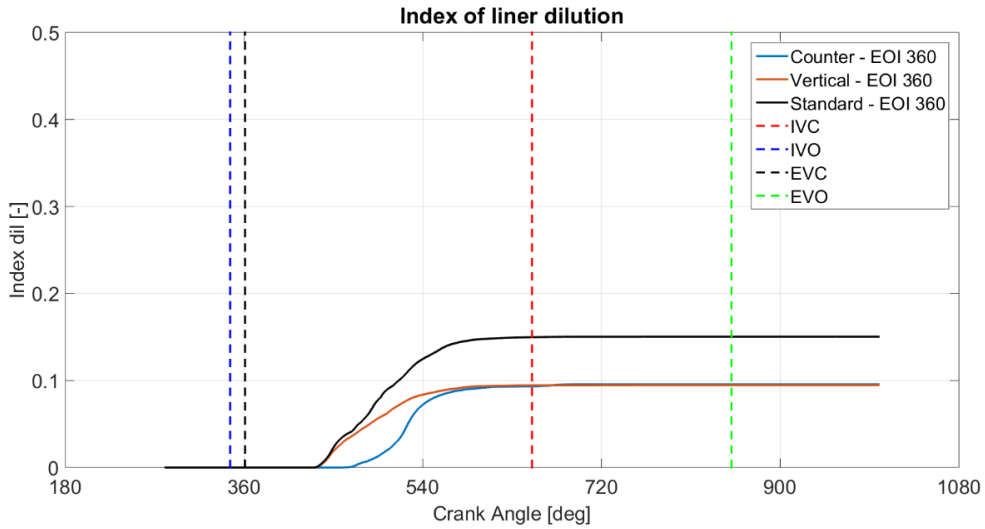

Figure 55. The comparison of the index of dilution for different configuration with EOI=360 degrees

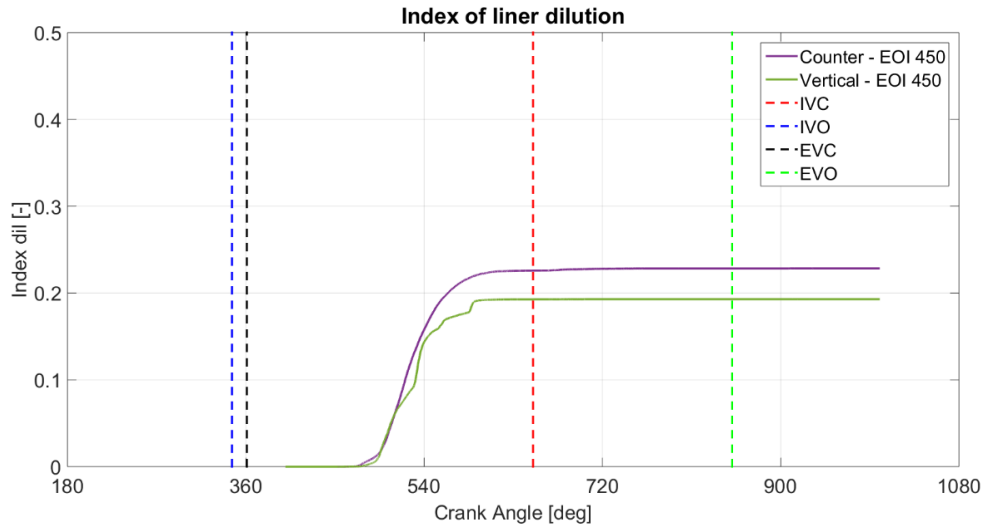

Figure 56. The comparison of the index of evaporation for different configuration with EOI=450 degrees

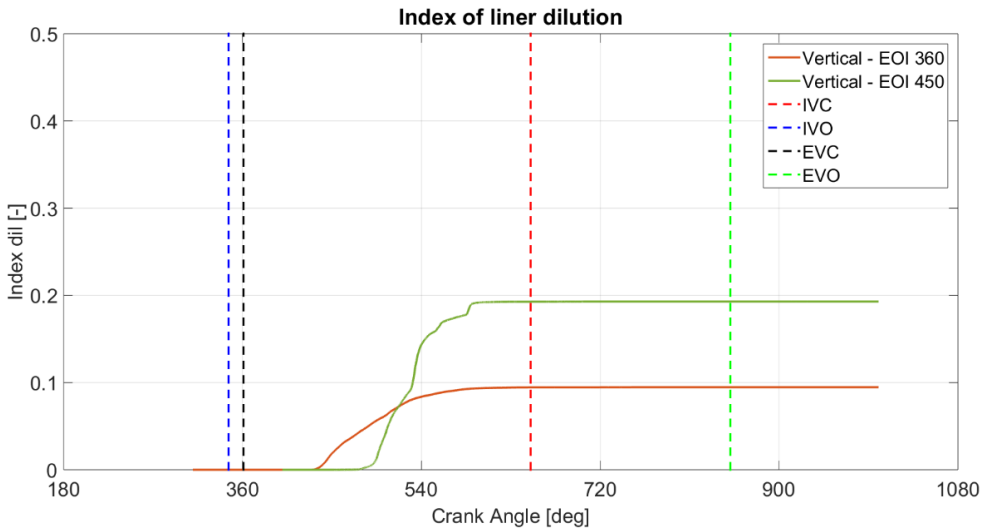

Figure 57. The comparison of the index of dilution for vertical configuration with different

In conclusion, preliminary 3D-CFD results showed that according to index of evaporation and index of dilution presented, the vertical configuration with EOI 360 degrees provides more advantages and therefore higher knock mitigation benefits with respect to other configurations. Therefore, in future investigations, different configurations including vertical could be further tested in experiments to maximize the benefits achieved through WI strategy.

.

Parte del lavoro descritto in questo capitolo è stato anche preventivamente pubblicato in:

Part of the work described in this Chapter was also previously published in the following publications:

1. V. Doria, A. Stroppiana, M. Ferrera, F. Millo, M. Mirzaeian, D. Porcu, "Knock Mitigation Techniques for Highly Boosted Downsized SI Engines: Miller Cycle and Water Injection", in: SIA Powertrain, Versailles, France, 2017.

2. N. Fogla, M. Bybee, M. Mirzaeian, F. Millo, S. Wahiduzzaman, "Development of a K-k-∈ Phenomenological Model to Predict In-Cylinder Turbulence", SAE Int. J. Engines. 10 (2017) 562–575.

3. M. Mirzaeian, F. Millo, L. Rolando, "Assessment of the Predictive Capabilities of a Combustion Model for a Modern Downsized Turbocharged SI Engine", in: SAE Tech. Pap. 2016-01-0557, SAE International, 2016. doi:10.4271/2016-01-0557.

Chapter 5

0D Combustion Modelling

5.1 Introduction

As the new downsized and turbocharged SI engines become more complex, the necessity to have reliable predictive combustion models capable to find the optimized configuration becomes dramatically important.

The first step to have a predictive combustion model is to have robust and reliable methods for the prediction of flow related phenomena such as turbulence, Mean Kinetic Energy (MKE) and length scale. Since 3D-CFD models are computationally expensive, it is not always possible to use them for the calibration purposes; hence, an accurate, cost effective and fast modeling approach in 0/1D simulation, with which a great number of configurations can be compared to find the most suitable solution of the analyzed problem, is required.

Several 0D turbulence models aiming to reproducing very complex 3D phenomena have been developed, based on homogenous and isotropic assumption [44,45]. For instance, Bozza et al. [46] have proposed a turbulence model belonging to K-k family in which the length scale is firstly estimated by the instantaneous clearance height inside the cylinder, and then adjusted by means of a calibration constant. This model has been used also by Vitek et al. [47]. De Bellis et al. [48] have implemented the same K-k model by using four different Wiebe functions to evaluate the length scale; however, this approach adds some constants to the problem that makes the calibration procedure more challenging. Rivas et al. [49] has proposed a method in which two balance equations for Turbulent Kinetic Energy (TKE) and dissipation rate are solved and the macro scale kinetic energy is imposed.

After estimation of flow parameters by a turbulence model, the predicted flow parameters have to be implemented in a predictive combustion model, in order to obtain the proper flame front development, burn rate and in-cylinder pressure. For instance, Gatowsky [50] has shown that the flame propagation within the turbulent flow field is a very thin and highly wrinkled surface inside the combustion chamber, and several combustion models can be found in literature trying to mimic these phenomena, such as [51], [52], [48] and [53]. In the current paper the so-called SI-Turb predictive combustion model is utilized which is described in more details in the following sections.

After calibration of the combustion model for the mean cycle, it is important to define a procedure to simulate CCV. A basic method for the CCV simulation consists of modeling of the combustion by means of a Wiebe function, whose coefficients are randomly varied ([17],[54]) to reproduce the experimental cyclic dispersion. Bozza et al. ([55],[56]) has utilized the experimental variation of maximum pressure and Indicated Mean Effective Pressure (IMEP) and has used a polynomial function in order to fit the mentioned parameters. The problem is that these models are not capable of predicting CCV outside of specific operating points studied. Indeed, they are the result of a fitting procedure of experimental data rather than the variation of real combustion parameters resulting in lack of prediction.

The other approach often used to model CCV is to perform multi-cycle simulations in which the input parameters of standard 1D-CFD combustion chamber models are randomly perturbed from cycle to cycle [44], [47]. In this kind of approach, a thorough experimental analysis is required to find the main cause of CCV and consequently to perturb the relevant combustion parameters in order to predict CCV at various operating points.

After simulating CCV, the final step is to have a knock model aiming to model auto-ignition of the end-gas. Models predicting auto-ignition of unburned mixture in spark-ignition engines range from simple empirical expressions to complex formulations featuring reduced or full chemical kinetics. Detailed chemical kinetic [57] models contain several elementary reactions and species required to define the combustion process. The detailed kinetic mechanism of n-butane and isobutene has been investigated by Wilk et al. [58] for the analysis of auto-ignition. This type of model can be utilized in conjunction with 3D-CFD as a part of a larger model in order to study the reactive flows [59]. Although these methods are very accurate for the prediction of knock onset, the problem is that they require substantial computational effort which makes them inefficient for control and optimization purposes.

Another alternative approach for studying auto-ignition is using the reduced chemical kinetics which captures only the rate limiting reactions leading to auto-ignition [60]. This approach is computationally efficient and it can be implemented for the prediction of combustion pathway by the proper calibration [61]. Cowart et al. [61], [62] has shown that both reduced and detailed mechanisms are capable of

predicting auto-ignition, while the time associated for these kind of simulations is still high to be utilized for control purposes; hence, it is of crucial importance to develop 0D models for this stochastic phenomena.

0D knock models are typically based on the approach developed by Livengood and Wu [63] which is the so-called knock integral method. Soylu et al. [64] has incorporated the knock integral method combined with a 0D model and has determined the Knock Limited Spark Advance (KLSA). Douaud and Eyzat [65] have proposed an Arrhenius function for the calculation of induction time with two calibration parameters which should be adjusted to fit the experimental knocking onset. This model has been widely used for the analysis and simulation of auto-ignition in 0D simulations [17].

In this chapter, a 0-D turbulence model [66] belonging to K-k and k- ε model family is presented, in which three sets of equations for "mean kinetic energy", "turbulent kinetic energy" and "dissipation rate" are solved at each time step. Afterwards, the model is calibrated on the basis of a single 3D-CFD simulation carried out in one engine operating point, and it is shown that the model is capable of properly predicting the level of turbulence for different engine operating points. Afterwards, the above described turbulence model has been coupled with the SI-Turb predictive combustion model [16], which was calibrated using Design of Experiments (DoE) method coupled with Genetic Algorithm (GA) to predict the burn rate at various operating points. It is worth to be pointed out that a single set of calibration parameters were used for all the engine operating points, covering a broad range of engine speeds and loads.

In the next step, the sensitivity of different stages of combustion has been investigated by multi cycle analysis of the burn rates at different operating points. It is confirmed that both first and second stages of combustion vary from cycle to cycle; therefore, it is of crucial importance to take into account both variations. Finally, an innovative procedure has been adopted in order to obtain Probability Density Functions (PDFs) of two calibration constants of the SI-Turb combustion model in order to simulate CCV. Finally, the CCV model has been coupled with a 0D knock model in order to calculate KLSA at different operating conditions.

5.2 Test matrix

5.2.1 Engine A test matrix

The experimental investigation has been carried out at 6 different engine loads, namely 2, 4, 6, 8, 10, 12 and 16 bar bmep, and 6 different engine speeds, namely 1500, 2000, 2500, 3500, 4000 and 4500 rpm. Moreover, spark timing sweeps were also carried out at 12 and 16 bar bmep, in order to better assess the predictive capability of the model. The test matrix is depicted in Figure 58. The engine has

been operated at stoichiometric air to fuel ratio and fuel type by which the experiment has been performed is gasoline 95 Research Octane Number (RON).

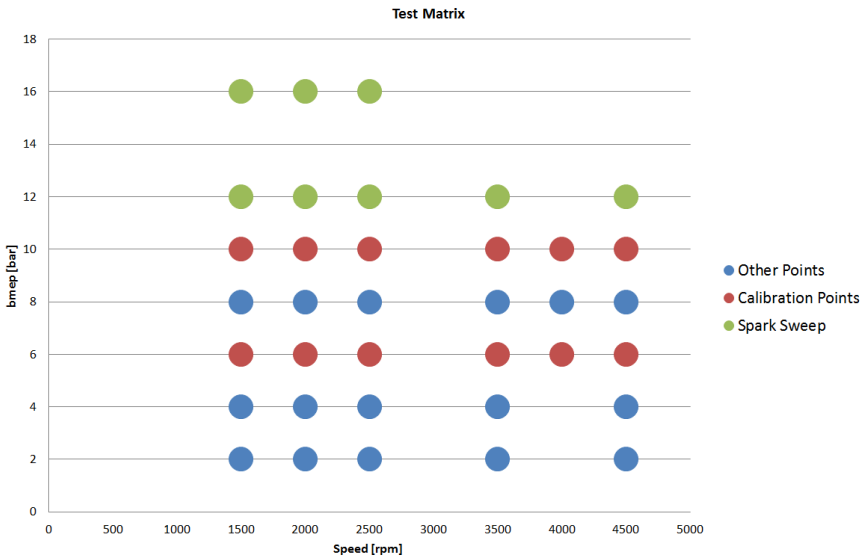

Figure 58. Experimental test matrix: operating points highlighted in red were used for model calibration, while points shown in blue and in green were used for the assessment of the model predicting capabilities

5.2.2 Engine B test matrix

The experimental tests performed on Engine B include lambda and spark sweeps at 2500 x 17, 4000 x 14, 2500 x 22, 4000 x 21 [rpm x bar bmep].

5.2.3 Engine C test matrix

The experimental tests performed on Engine C, using CR13, include:

- EGR sweep at 2000 x 10, 3000 x 10, 4000 x 10, 3000 x 13, 4000 x 13[rpm x bar bmep].
- Water injection and Spark Advance (SA) sweep at 2000 x 15, 4000 x 17 [rpm x bar bmep].

5.3 0D turbulence model

The 0D turbulence model has been conceived and elaborated by the development team of Gamma Technologies LLC, IL, USA in GT-SUITE which is described in details in [66]. In a 0D setting, most in-cylinder flow models found in the literature follow either a K-k energy cascade approach, where K is the mean kinetic energy and k is the turbulent kinetic energy, or a k- ε approach, where ε is the dissipation rate. In the energy cascade method [67], the mean kinetic energy and turbulent kinetic energy are modeled via two differential equations, one each for K and k.

Algebraic equations are used to model the turbulence dissipation rate and integral length scale. Mean Kinetic Energy, generated primarily due to valve flow, leads to the production of turbulence via shear stresses, modeled as a production source term. In the k- ε method [68] turbulent kinetic energy and its dissipation are modeled via two differential equations. The effects of mean fluid motion are added via source terms (representing intake flow, turbulence production via shear, etc.) in the turbulent kinetic energy equation. Integral length scale of turbulence is obtained as an output of the two equations via the Equation 16:

$$L_t = 0.164\frac{k^{\frac{3}{2}}}{\varepsilon} \tag{16}$$

Effects of tumble and/or swirl are modeled via additional differential equations conserving angular momentum. Source terms in the angular momentum and the turbulence equations capture the effects of mean motion decay and production of turbulence, respectively.

In this model, the K-k and the k-ϵ approaches have been combined via three differential equations. (Equation 17, 18 and 19)

$$\frac{d(mK)}{dt} = C_{in}(1-\alpha_{in})E_{in} + K\dot{m}_{out} - P_k \tag{17}$$

$$\frac{d(mk)}{dt} = C_{in}\alpha_{in}E_{in} + k\dot{m}_{out} + P_k + C_{tumb}Tf - m\dot{\epsilon} \tag{18}$$

$$\frac{dm\dot{o}}{dt} = C_{in}E_{in}\frac{\sqrt{k}}{L} + \dot{\epsilon}\dot{m}_{out} + P_{\dot{\epsilon}} + C_{tumb}Tff\frac{\sqrt{k}}{L} - 1.92\frac{m\dot{\epsilon}^2}{k} \tag{19}$$

The equations shown above govern the evolution of the following flow quantities:

- Mean kinetic energy $K = \frac{1}{2}U^2$, where U is the mean velocity inside the cylinder.
- Turbulent kinetic energy $k = \frac{3}{2}u'^2$ where u' is the intensity of the turbulent field inside the cylinder, assumed to be homogeneous and isotropic.
- Turbulent dissipation rate $\dot{\epsilon}$.

The first term on the right-hand side of each equation describes the production of each quantity due to flow entering the cylinder. The term E_{in} is calculated as Equation 20.

$$E_{in} = (1-C_T)\frac{1}{2}\dot{m}_{in}v_{in}^2 \tag{20}$$

Where $\dot{m}_{in}$ and v_{in} are the mass flow rate and isentropic velocity of the flow entering the cylinder, respectively. C_T is the tumble coefficient associated with the valves, typically measured on a steady state flow bench as a function of the valve lift and provided as an input to the 0D model. The tumble coefficient provides a measure of the fraction of inflow energy that is imparted to the tumble macro-vortex. This coefficient takes on values from 0 to 1.

The coefficient α_{in} is indicative of the fraction of inflow energy that directly enters the cylinder as turbulence and is not generated by the cascade process. It tries to model turbulence generated in the cylinder as soon as the valves open causing significant shearing flow and was set to a fixed value of 0.1.

The term $C_{in} = 0.18 \times C_1$ is a model parameter which is used to account for the actual flow velocities through the valves, which are not equal to the isentropic ones. C_1 is a tuning constant which can be used to adjust the magnitude of the inflow source term. Exhaust backflow into the cylinder, which is included in the inflow source term, typically occurs for a shorter period of time compared to the intake flow. Also, this high velocity backflow is typically localized to a smaller region of the cylinder. This localized source of energy can be well resolved by 3D-CFD and hence it makes a small contribution to the values of energy that are averaged over the entire cylinder. However, the 0D model does have the required spatial resolution to capture this localized source and hence energy coming in the cylinder via exhaust backflow was scaled differently to incorporate the effect of localization. A scaling constant equal to $0.3C_{in}$ was found to produce appropriate results. The second term in the equations describes the energy flowing out of the valves, where $\dot{m}_{out}$ is the mass flow rate of the flow exiting the cylinder.

The terms P_k and $P_{\dot{\epsilon}}$ model the production of turbulent kinetic energy and dissipation rate, respectively, from the large-scale mean flows via the energy cascade process. These terms are calculated as Equation 21 and Equation 22.

$$P_k = C_\beta v_T \frac{2mK}{L^2} - \frac{2}{3} mk\left(\frac{\dot{\rho}}{\rho}\right) \tag{21}$$

$$P_{\dot{\epsilon}} = \frac{\dot{\epsilon}}{k}\left(5.76 C_\beta v_T \frac{mK}{L^2} - 2mk\left(\frac{\dot{\rho}}{\rho}\right) - \frac{2.64}{3} m v_T \left(\frac{\dot{\rho}}{\rho}\right)^2\right) \tag{22}$$

Where:

- $v_T = 0.09 \frac{k^2}{\dot{\epsilon}}$ is the turbulent viscosity,
- ρ and $\dot{\rho}$ is the density and rate of change of density of the charge inside the cylinder respectively
- $C_\beta = 0.38 C_2$ is a model parameter

- The term $L = C_{len} \times \min(s, 0.5B)$, B being the bore of the cylinder and s the instantaneous piston stroke, is representative of a geometric length scale.
- The model parameter $C_{len} = 0.19 \times C_3$ modulates the value of the length scale. The tuning constants C_2 and C_3 can be used to adjust the magnitudes of the production source terms. The forms of the production terms shown in Equation 21 and Equation 22 are motivated by their forms in the k-ϵ equations typically used in 3D-CFD [69]

The terms including the quantity T, model the production of turbulence due to the decay of the tumble macro-vortex during the compression stroke and C_{tumb} is a tuning constant that controls the intensity of this process. The last term on the right-hand side of each equation acts as a sink term for that respective quantity. The mean kinetic energy is converted into turbulent kinetic energy via turbulent dissipation modeled by the term P_k, the turbulent kinetic energy is converted into heat via viscous dissipation $m\dot{\epsilon}$ and the dissipation of the turbulent dissipation rate is given by the term $1.92 \frac{m\dot{\epsilon}^2}{k}$.

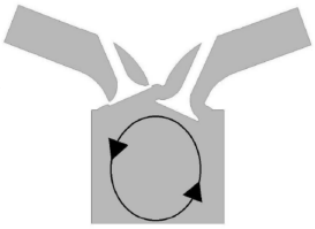

Figure 59. Illustration of the tumble macro-vortex.

The rotational component of the mean flow, i.e. the tumble, is modeled as a single macro-vortex, as shown in Figure 59, whose evolution is described via an equation for its angular momentum $L = m\tilde{r}^2\omega$ given as Equation 23.

$$\frac{dL}{dt} = \dot{L}_{in} + \dot{L}_{out} - Lf\left(\frac{s}{B}\right)\frac{\sqrt{k}}{\tilde{r}} \tag{23}$$

The first term on the right-hand side of Equation 23 represents the tumble production by the incoming charge which is defined as Equation 24:

$$\dot{L}_{in} = C_T \dot{m}_{in} |v_{in}| \tilde{r} \tag{24}$$

Where $\tilde{r}$ is the radius of the tumble macro-vortex and is modeled as $\tilde{r} = \frac{1}{4}\sqrt{B^2 + s^2}$. The second term on the right-hand side of Equation 23 accounts for flow out of the cylinder and is given by Equation 25, in which ω is the angular speed of the tumble macro-vortex.

$$\dot{L}_{out} = \dot{m}_{out}\tilde{r}^2\omega \tag{25}$$

The third term on the right-hand side of Equation 23 accounts for the decay of the tumble vortex during compression and its conversion to turbulence close to Top Dead Center (TDC). It is modeled in a fashion similar to Grasreiner et al. [70]. The decay is proportional to the turbulence levels in the cylinder and is modulated by the term $f\left(\frac{s}{B\tilde{r}}\right)$. This term seeks to intensify the tumble decay as the piston approaches close to TDC. The tumble decay function f is plotted versus $\left(\frac{s}{B}\right)$ in Figure 60. The contribution of tumble decay to turbulence is modeled via the term T given by Equation 26.

$$T = \frac{1}{2} L\omega f(\frac{s}{B}) \frac{\sqrt{k}}{\tilde{r}} \tag{26}$$

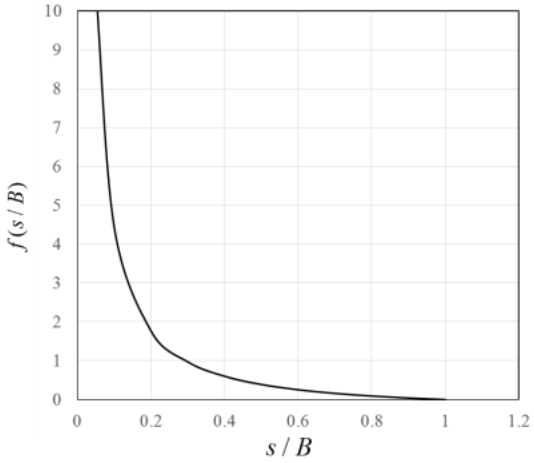

Figure 60. Tumble decay function

Finally, since both turbulent kinetic energy and dissipation rate are being modeled in the proposed model, evolution of the integral length scale over time can be easily be obtained via Equation 16.

The proposed flow model can be calibrated to match 3D-CFD results by varying the following tuning constants:

- ✓ C_1- controls the levels of mean and turbulent kinetic energies during inflow into the cylinder.
- ✓ C_2, C_3- control the production of turbulence from the mean flow.
- ✓ C_{tumb}- controls the contribution of tumble decay to turbulence production.

Note that the tuning constants C_1, C_2 and C_3 influence the model parameters C_{in}, C_β and L, respectively. The effects of varying these tuning constants individually on the turbulent kinetic energy output from the model are shown in Figure 61.

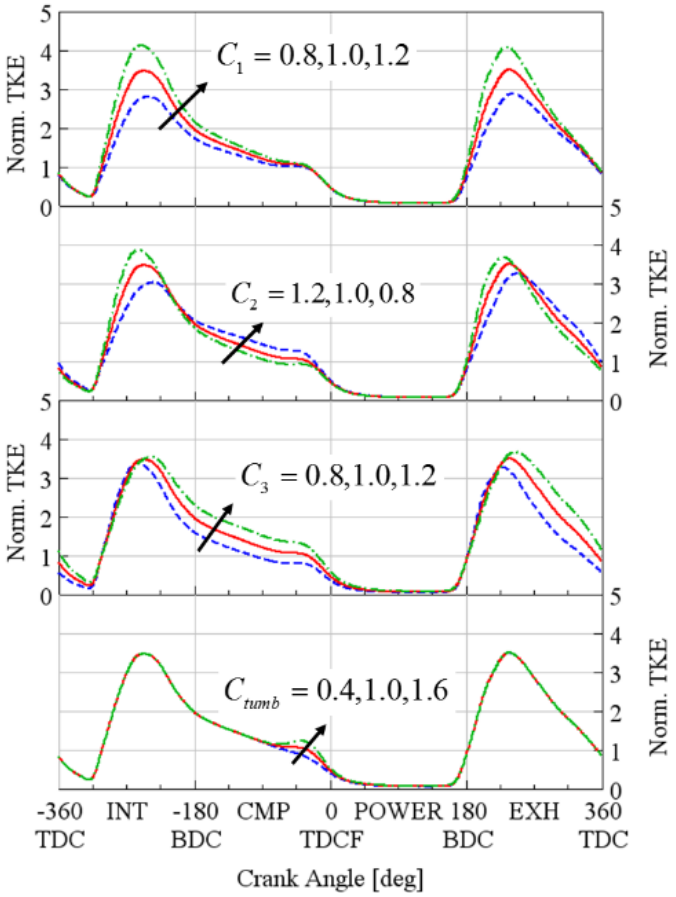

Figure 61. Effects of varying the tuning constants of the 0D model on turbulent kinetic energy output.

5.4 SI-Turb predictive combustion model

The main characteristics of the SI-Turb combustion model which was adopted in this work will be briefly summarized hereafter for reader's convenience. More details can be found in [71], [53].

The entrained mass rate of the unburned gas $\left(\frac{dM_e}{dt}\right)$ is dependent on the flame area (A_f) and the entrained velocity as expressed by Equation 27, where , S_L and S_T are laminar flame speed and turbulent flame speed, respectively.

$$\frac{dM_e}{dt} = \rho_u A_f (S_L + S_T) \tag{27}$$

During the first flame kernel development phase, the gas entrainment is limited by the laminar flame speed, and it is therefore important to account for transition to

the turbulent flame speed, which can be indicated by Equation 28, where R_f, $u'$and L_t are flame radius, turbulent intensity and turbulent length scale, respectively.

$$S_T = C_s u'(1 - \frac{1}{1 + \frac{C_k R_f^2}{L_t^2}}) \tag{28}$$

In Equation 28, the flame kernel growth multiplier (C_k) scales the flame front evolution from an initial smooth surface – corresponding to a laminar-like combustion – to a fully developed turbulent wrinkled flame, while the turbulent flame speed multiplier (C_s) is a scaling factor for the turbulent flame speed.

The rate of burnup $\left(\frac{dM_b}{dt}\right)$ is then proportional to the unburned mass behind the flame front, resulting in Equation 29.

$$\frac{dM_b}{dt} = \frac{M_e - M_b}{\tau} \tag{29}$$

Where τ is assumed to be the time needed by the laminar flame speed to cover the Taylor microscale (λ) of turbulence, expressed by Equation 30. Assuming isotropic turbulence, the Taylor micro scale can be computed by using Equation 31, where C_λ is a further calibration parameter.

$$\tau = \frac{\lambda}{S_L} \tag{30}$$

$$\lambda = \frac{C_\lambda L_t}{\sqrt{Re_t}} \qquad \text{where} \qquad Re_t = \frac{\rho_u u' L_t}{\mu} \tag{31}$$

Finally, the effect of dilution (exhaust residuals and EGR) on the laminar flame speed is taken into account by means of a further calibration parameter, the Dilution Exponent Multiplier (DEM), as shown in Equation 32.

$$S_L = \left(B_m - B_\phi(\phi - \phi_m)^2\right)\left(\frac{T_u}{T_0}\right)^\alpha \left(\frac{p}{p_0}\right)^\beta (1 - 2.06 Dilution^{2.77 DEM}) \tag{32}$$

Where:

- B_m is the maximum laminar speed which is set to $0.35\ m/s$
- B_ϕ is laminar speed roll-off value which is used to describe the decay profile of the flame speed from its maximum value as a function of fuel/air equivalence ratio which is set to -0.549
- ϕ is the in-cylinder equivalence ratio
- ϕ_m is the fuel/air equivalence ratio at the maximum laminar flame speed which is set to 1.10

- T_u is the unburned gas temperature
- P is the in-cylinder pressure
- T_0 is the reference temperature equal to 298 K
- p_0 is the reference pressure equal to 101325 Pa
- α is the temperature exponent, $\alpha = 2.4 - 0.271\phi^{3.51}$
- β is the pressure exponent, $\beta = -0.357 + 0.14\,\phi^{2.77}$
- $Dilution$ is the mass fraction of the residuals in the unburned zone

5.5 3D-CFD preliminary analysis for calibration of 0D turbulence model

In this work, the 3D-CFD simulation has been done for the cold flow motored condition using a Reynolds Averaged Navier-Stokes (RANS) turbulence model. The 3D-CFD outputs at one operating point is being utilized for Engine A in order to calibrate the 0D turbulence model. The other operating points are used for the validation of the model.

The mass averaged integral length scale (L_I), the specific turbulent kinetic energy (TKE) and the mean flow kinetic energy (MKE) are calculated all over the 3D domain according to Equations group 33, where *i*, ρ, *U* and *V* represent cell number, density, mean flow velocity and volume, respectively. The calibration constants which are adopted in the 0D turbulence model is being utilized in order to match the turbulent kinetic energy and integral length scale of turbulence in the 0D model with the mass averaged integral length scale (L_I) and the specific turbulent kinetic energy (TKE) coming from 3D-CFD.

$$\begin{cases} L_I = \dfrac{\sum_i \rho_i V_i L_{I,i}}{\sum_i \rho_i V_i} \\ TKE = \dfrac{\sum_i \rho_i V_i k_i}{\sum_i \rho_i V_i} \\ MKE = \dfrac{\sum_i \rho_i V_i U_i^2}{\sum_i \rho_i V_i} \;\; ; U_i = \sqrt{u_i^2 + v_i^2 + w_i^2} \end{cases} \tag{33}$$

5.6 0D calibration of the model for the mean cycle

After the calibration of the 0D turbulence model, the model constants are fixed for the calculation of the turbulent length scale and the turbulent intensity which are required as inputs for the SI-Turb combustion model. Afterwards, the procedure described in this section was utilized in order to calibrate the SI-Turb combustion model by tuning C_k, C_s, C_λ and *DEM* constants. The 12 engine operating points at

6 and 10 bar bmep, shown in red in Figure 58, were chosen for the calibration of the combustion model, while the other operating points were used for the assessment of the predictive capability of the model.

A Design of Experiment (DoE) [72] methodology, integrated with a Genetic Algorithm (GA) optimization search method, was used in order to identify the optimized calibration parameters C_k, C_s, C_λ and *DEM* aiming to minimize the error between experimental and simulated burn rates for the selected operating conditions (i.e. 6 and 10 bar bmep points) in the engine map.

As far as DoE is concerned, after a preliminary analysis on the calibration constants, the calibration parameters were varied ranging from 0.5 to 2. A 0.05 increment for each parameter would have required, with a full factorial approach, a total number of experiments of 810'000 for each engine operating point, which is clearly not feasible. A Latin Hypercube approach for the DoE analysis was therefore preferred, which, with the same variation range for each parameter from 0.5 to 2, can explore all the region under investigation by means of a reduced number of experiments, which was chosen to be equal to 2000 for each operating point.

Afterwards, the fitting equation for the error between experimental and simulated burn rates should be identified. The quadratic polynomial in Equation 34 has been used in order to represent the mentioned error. In order to find the best value of $a_i (i = 1,2, \dots 14)$, the least square method has been utilized. It is obvious that the fitting procedure should be done for all of the operating points used for the calibration procedure.

$$\begin{aligned} burn\ rate\ error = {} & a_1 + a_2 C_k + a_3 C_s + a_4 C_\lambda + a_5 \mathrm{DEM} \\ & + a_6 C_k C_\lambda + a_7 C_k C_s + a_8 C_k \mathrm{DEM} + a_8 C_s C_\lambda \\ & + a_9 C_s DEM + a_{10} C_\lambda DEM + a_{11} C_k^2 + a_{12} C_s^2 \\ & + a_{13} C_\lambda^2 + a_{14} DEM^2 \end{aligned} \tag{34}$$

Since the aim of the combustion model is to find one set of parameters for all operating points, it is important to define one single objective function to minimize all the error functions simultaneously. Therefore, the cumulative squared error between the predicted response values and target values has been chosen to find the calibration constants (Equation 35).

$$total\ error = \sum_{1}^{i=12} (burn\ rate\ error)_i^2 \quad i = 1,2, \dots, n \tag{35}$$

where n is the number of operating points using for the calibration procedure which is equal to 12 for this model.

In the next step, GA was used with the aim to find the optimized solution such that the "$total\ error$" is minimized. The reason why GA was chosen for the optimization is that with this approach the search is not likely to be trapped in a local minimum, and hence it is more probable to reach the global optimum solution.

5.7 CCV investigation

CCV simulation in 0D is typically done by imposing random perturbations on modelling constants of governing combustion and/or in-cylinder flow [44,47,73] As an example, Vitek et al. [47] used perturbations imposed on turbulence integral length scale, ignition delay and combustion near walls. In another study, Sjeric et al. [73] applied Gaussian perturbations imposed on turbulence production, while Dulbecco et al. [74] used Gaussian perturbations imposed on tumble number and turbulence integral length scale. In addition, Wenig et al. [44] modeled CCV by means of fluctuation factor on laminar flame velocity and inflammation phase.

After preliminary experimental analysis of the in-cylinder pressure on a cycle by cycle basis, suitable perturbation to the 0D combustion model parameters aiming to mimic CCV at different operating condition could be found. Based on a sensitivity analysis on different combustion parameters, ignition delay and TFSM (reflecting the variability of MFB10-75) parameters are selected for imposing perturbation to mimic CCV.

As far as ignition delay perturbation is concerned, a speed dependent correlation [44] has been added to the ignition delay, expressed in Equation 36. The standard deviation (σ) is calculated by Equation 36 and the upper and lower limit of the PDF is limited by $\pm 3\sigma$. The speed dependent parameter (E_s) can also be used to further tune the model, however it is left 1.0 for all operating points. Therefore, the only adjustable parameter of the model is $cons$ which is considered equal to 5.5.

$$3\sigma\ [CA\ deg] = range\ of\ Ign = cons - 3.5E_s\left(\frac{n}{1000}\right)^{-1.75} \tag{36}$$

As far as TFSM perturbation is concerned, the PDF can be calculated using a mean value, through mean cycle calibration, and an upper limit. In order to define the upper limit:

- ✓ Firstly, a cumulative probability function for the peak pressures of all the cycles is fitted at an arbitrary operating point, as shown in Figure 62.
- ✓ Afterwards, the peak pressure at 90% probability over the fitted function is obtained, P_1.
- ✓ The corresponding TFSM is computed such that the peak pressure is targeted to P_1.

- ✓ The obtained TFSM is defined as the upper limit for the PDF such that 90% probability is acquired. Once the PDF is calculated, it is fixed and is used for all the operating points.

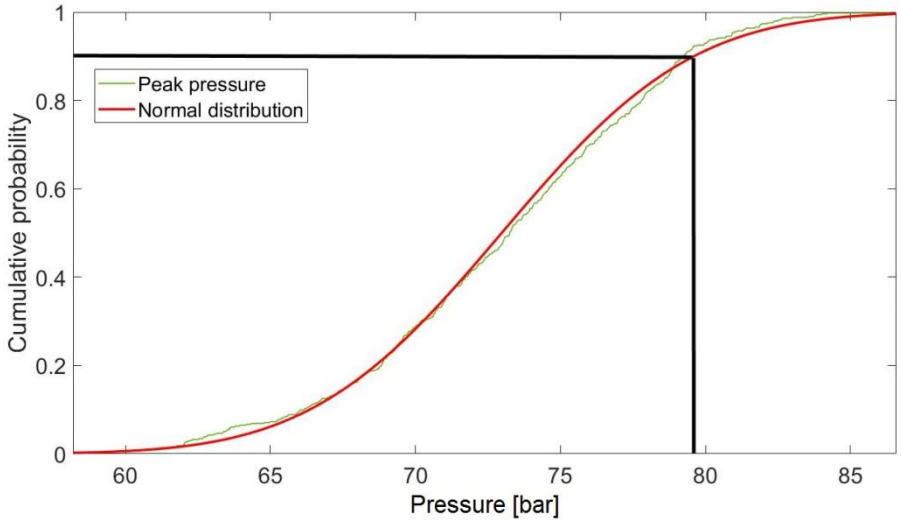

Figure 62. Cumulative probability function of peak pressure at 2500 rpm x 16 bar bmep, Engine A

5.8 Knock analysis

5.8.1 Experimental knock investigation

Since one of the main objectives of the current work is the prediction of Knock Limited Spark Advance (KLSA), first of all, it is required to evaluate the experimental KLSA

Among the various approaches for knock detection, the standard procedure adopted at Centro Ricerche Fiat (CRF), Italy, is based on the high frequency filtering of in-cylinder pressure measurements which allows calculation of the Maximum Amplitude of Pressure Oscillation (MAPO) index indicated by Equation 37.

$$MAPO = \max(p_f) \tag{37}$$

Where p_f is the rectified in-cylinder pressure, windowed in a crank angle interval, -5.70 Crank Angle (CA), and high-pass filtered by a specified knock related cut-off frequency. For the sake of brevity the mentioned analysis will not be given in the current work while the procedure of the detailed analysis can be found in the study performed by Millo et al. [75],[17].

5.8.2 Douaud and Eyzat (DE) knock model

The knock integral method is based on the assumption that the auto-ignition of the end gas occurs once Equation 38 is satisfied, in which t_i is the time of auto-ignition and t is the elapsed time from the start of the end gas compression process.

$$Induction\ time\ integral = \int_{t=0}^{t_i} \frac{dt}{\tau} = 1 \tag{38}$$

A number of empirical relations for the estimation of the induction time are introduced among which the most extensively tested correlation is proposed by Douaud and Eyzat. Two calibration parameters namely Induction Time Multiplier (ITM) and Activation Energy Multiplier (AEM) are adopted as expressed by Equation 39.

$$\tau = 17.68 ITM \left(\frac{NO}{100}\right)^{3.402} P^{-1.7}\ exp\left(\frac{3800 AEM}{T}\right) \tag{39}$$

As an example, Figure 63-a indicates that the induction time integral did not reach 1 until all the fuel is being burnt .On the contrary, it can be observed in Figure 63-b that the induction time integral reaches 1 while some unburned mixture is still available inside the cylinder which is translated in to a knocking phenomenon.

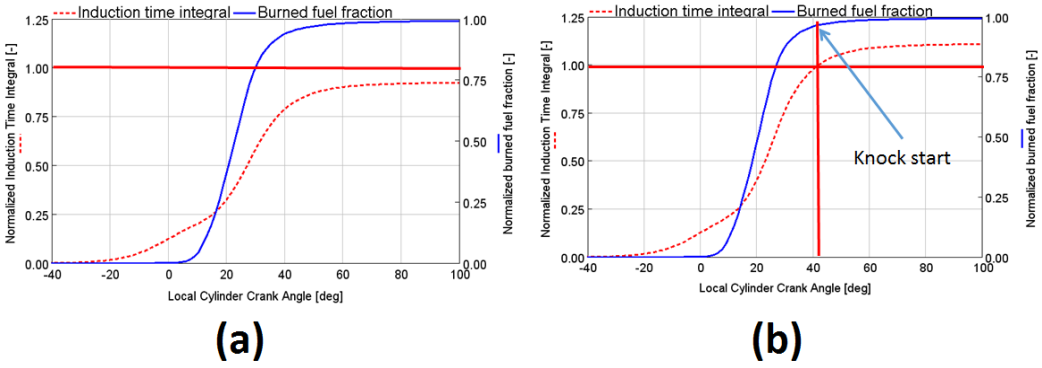

Figure 63. Burned mass fraction and induction time multiplier a) knock free condition b) knocking condition

5.9. Results and discussion

5.9.1 Turbulence model validation

The calibration of the turbulence model has been carried out at 2500 rpm, Wide Open Throttle (WOT), under "cold flow" conditions (i.e. without simulating the combustion process) for Engine A. The comparison between the 0D and 3D-CFD values of turbulent kinetic energy and normalized length scale (normalized with

respect to the cylinder bore) is depicted in Figure 64: a satisfactory agreement can be observed.

Afterwards, other engine operating points were also simulated for the assessment of the model predicting capabilities. For the sake of conciseness, only the comparison between 3D-CFD and 0D turbulence of TKE and normalized length scale at 5500 rpm, WOT, is shown in Figure 65 as an example, which confirms the satisfactory predicting capability of the 0D turbulence model.

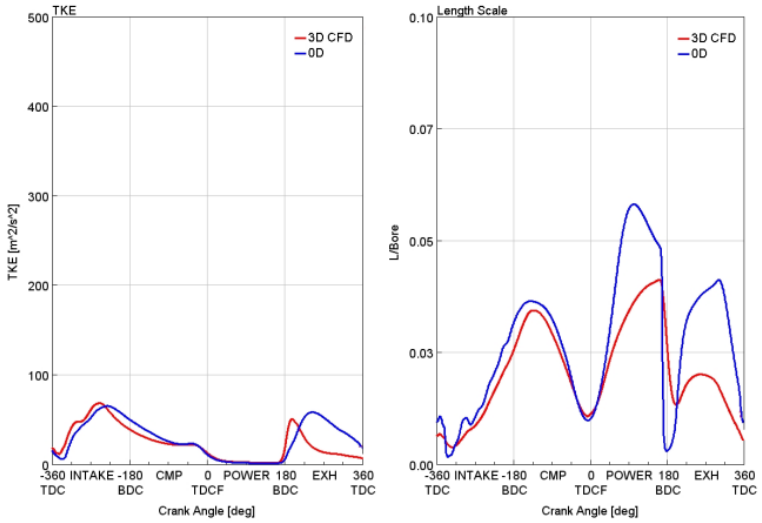

Figure 64. Turbulent kinetic energy and normalized length scale at 2500 rpm (0D turbulence model calibration), Engine A

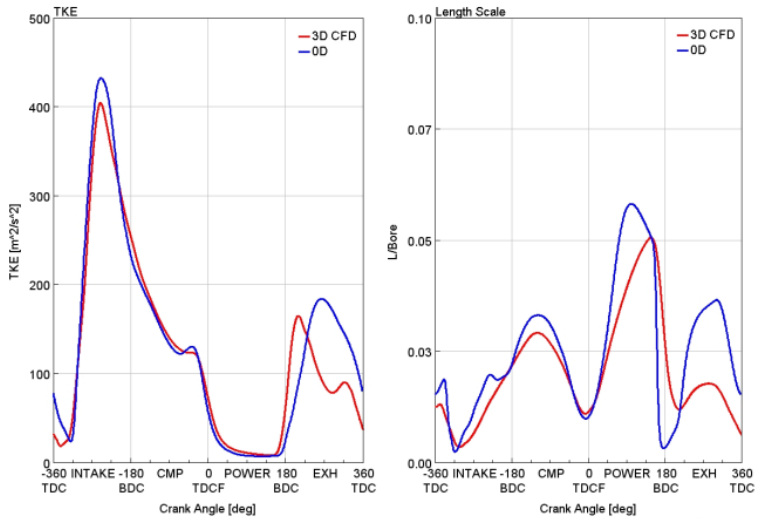

Figure 65. Turbulent kinetic energy and normalized length scale at 5500 rpm (0D turbulence model validation), Engine A

The TKE dissipation rate is calculated by means of Equation 16 and the comparison between 3D-CFD and 0D has been shown in Figure 66. Although the predicted TKE dissipation rate is under-estimated during the exhaust and intake regions, it has a relatively good conformity with 3D-CFD close to Top Dead Center Firing (TDCF) which is the important part for combustion prediction. Moreover, the MKE comparison between 0D and 3D-CFD has been shown in Figure 67.

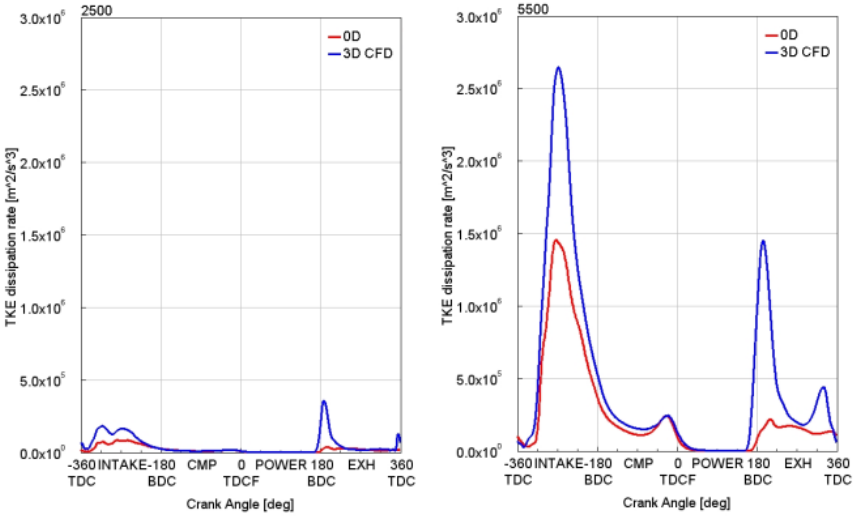

Figure 66. TKE dissipation rate comparison between 0D and 3D-CFD, Engine A

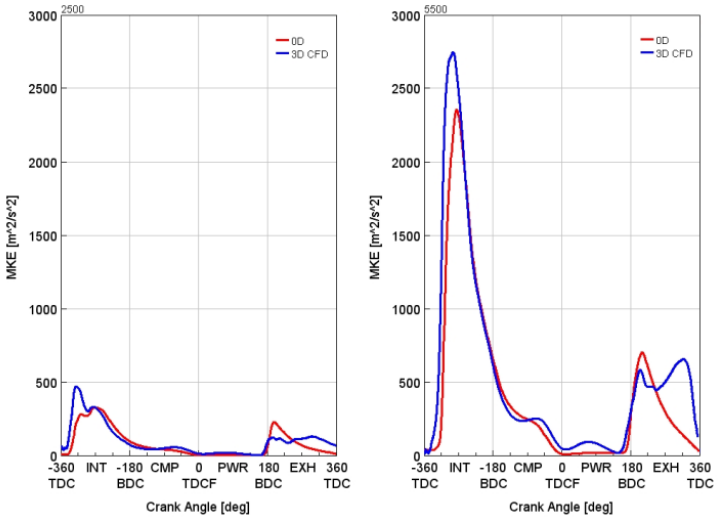

Figure 67. MKE comparison between 0D and 3D-CFD, Engine A

5.9.2. Combustion model validation

5.9.2.1 Base points, effect of spark timing and lambda

After calibration of the SI-Turb combustion model as described in Section 5.4, the optimized SI-Turb calibration parameters are obtained and kept constant for the entire engine operating points. For the sake of conciseness, the pressure and burn rate profiles for Engine A have been shown in Figure 68, Figure 69 and Figure 70; respectively, for three different loads and speeds ranging from low to high values to indicate the predictive capability of the model for various engine map regions. As it can be seen, there is an acceptable accuracy between the experimental and simulated burn rates and in-cylinder pressure traces.

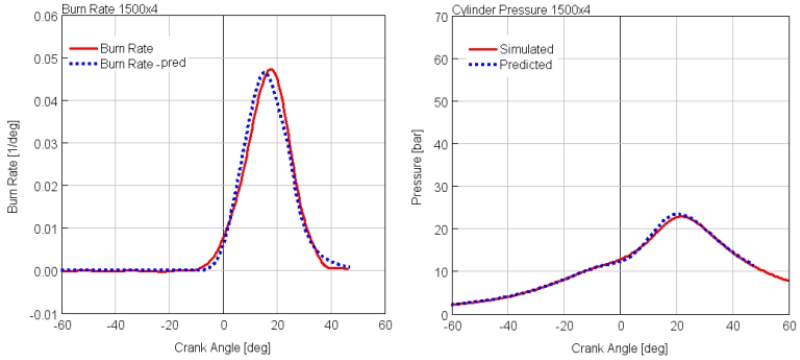

Figure 68. The comparison between simulated and experimental in-cylinder pressure and burn rate at 1500 rpm x 4 bar bmep, Engine A

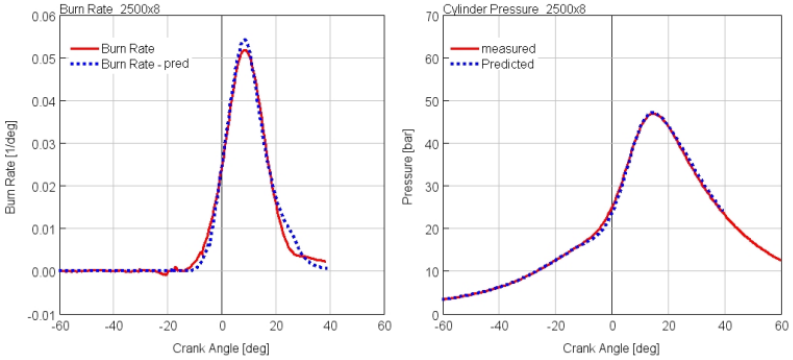

Figure 69. The comparison between simulated and experimental in-cylinder pressure and burn rate at 2500 rpm x 8 bar bmep, Engine A

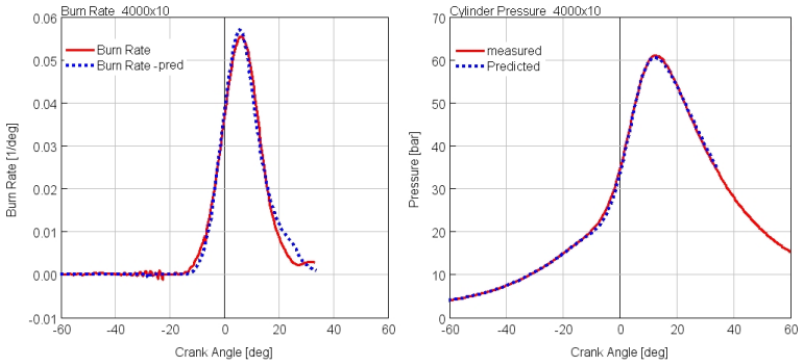

Figure 70. The comparison between simulated and experimental in-cylinder pressure and burn rate at 4000 rpm x 10 bar bmep

The resulted IMEP percentage errors between experimental and simulation for low and part load conditions are depicted in Figure 71. It can be realized that the maximum IMEP percentage error is around 2.5 percent which confirms the robustness and reliability of the model.

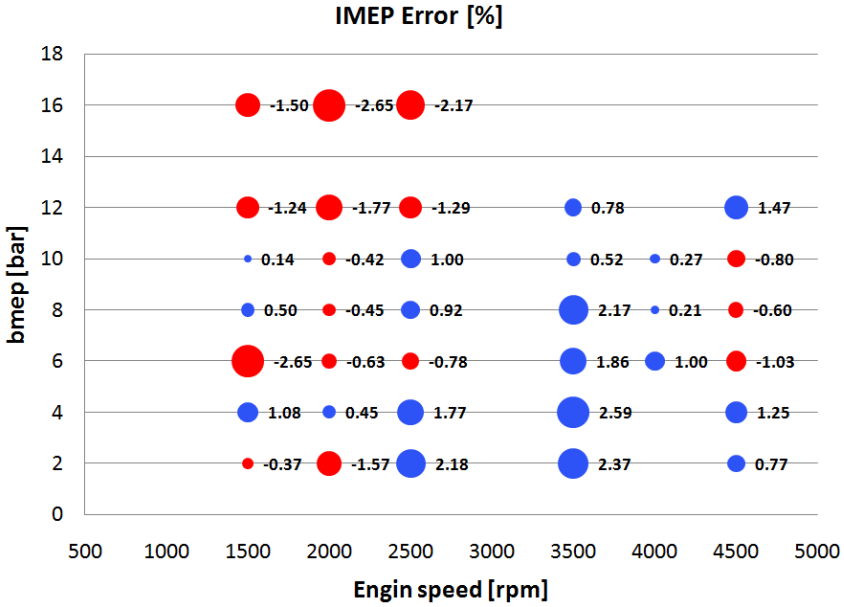

Figure 71. Percentage error between the experimental and simulated IMEP at all operating points, Engine A

The errors between experimental and simulated of MFB50, burn duration from 10 to 75 (MFB10-75), peak pressure crank angle and the peak pressure are depicted in Figure 72, Figure 73, Figure 74 and Figure 75, respectively. It can be seen that the maximum errors are about 2.8, 1 and 2 crank angles and 4.72 bar, respectively, which confirms the good predicting capability of the model. It is worth mentioning that could be possible to give some speed and load functions to the calibration

parameters to achieve better accuracy but it jeopardizes the aim of this work which is the utilization of one set of parameters for all operating points.

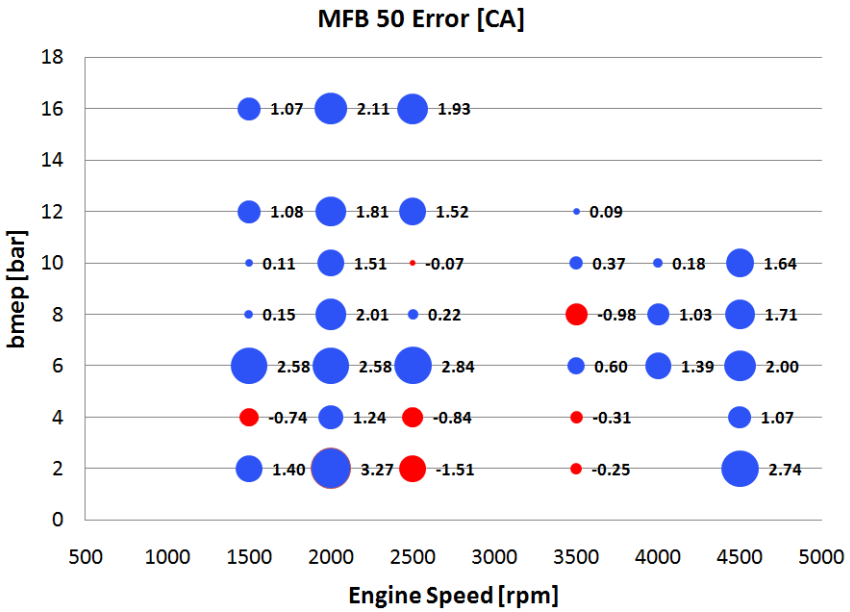

Figure 72. Error between simulated and experimental crank angle at MFB50, Engine A

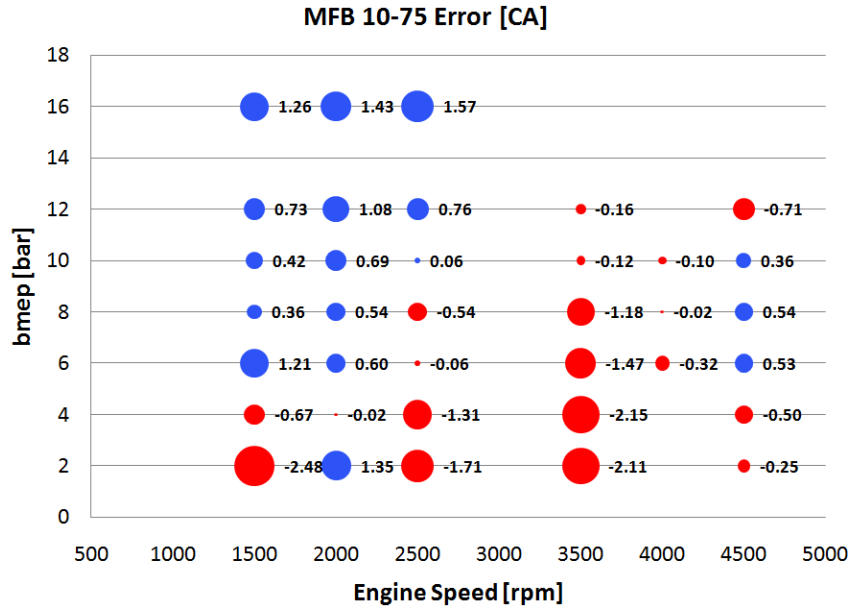

Figure 73. Error between simulated and experimental burn duration of MFB10-75, Engine A

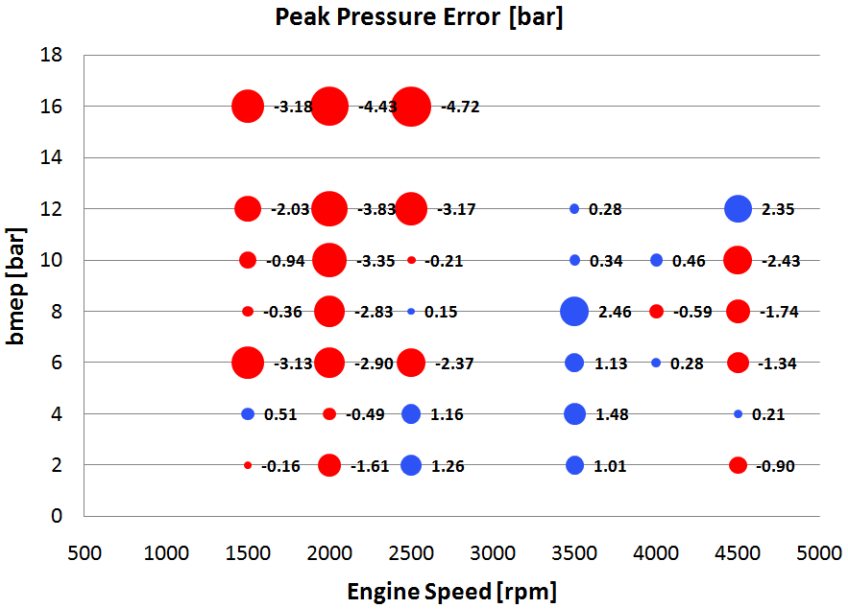

Figure 74.Error between simulated and experimental peak pressure, Engine A

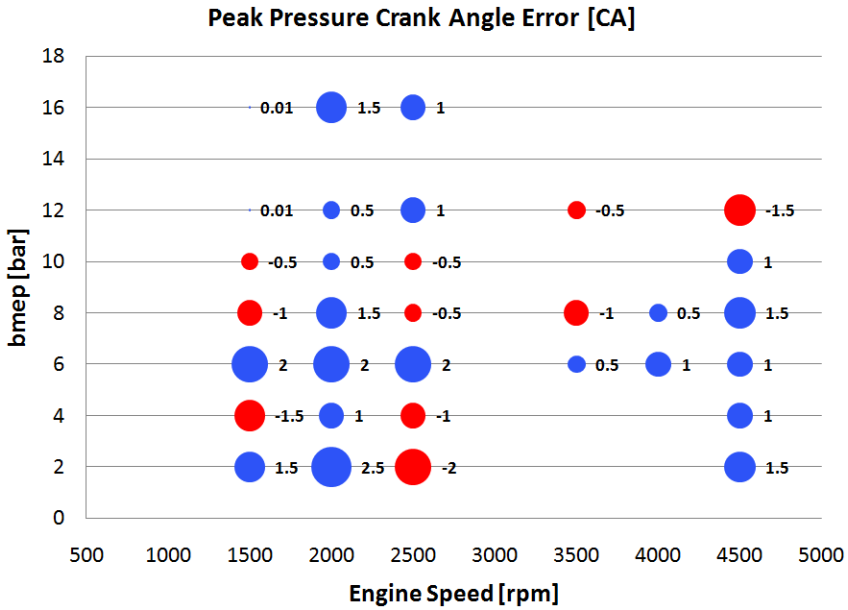

Figure 75. Error between simulated and experimental peak pressure CA, Engine A

In order to further assess the predicting capability of the model, spark timing sweeps at higher load condition were also analyzed. The IMEP percentage errors for three different spark timing settings are depicted in Figure 76. It can be observed that the errors are within an acceptable range, thus confirming the predictive capability of the model.

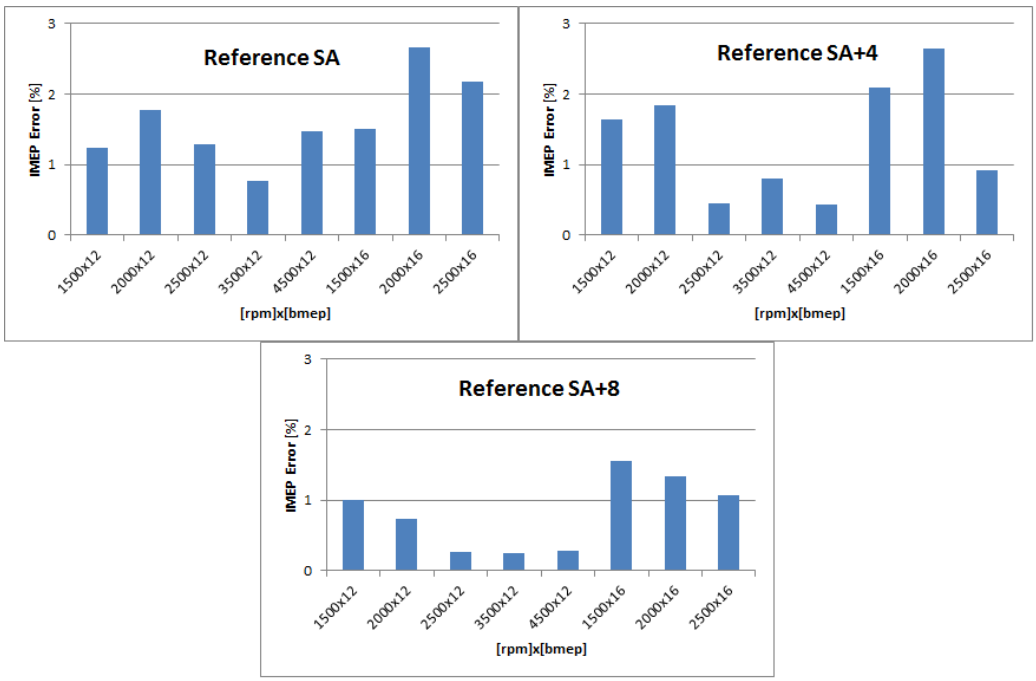

Figure 76. Percentage error between the predicted and experimental IMEP values for different spark timing settings, Engine A

Moreover, the absolute errors which are the difference between the predicted and experimental peak pressure, MFB50, burn duration (MFB10-75) and crank angle at peak pressure, have been shown in Figure 77, Figure 78 and Figure 79 for three spark timing settings which indicate that the model is capable of predicting combustion related parameters with an acceptable accuracy.

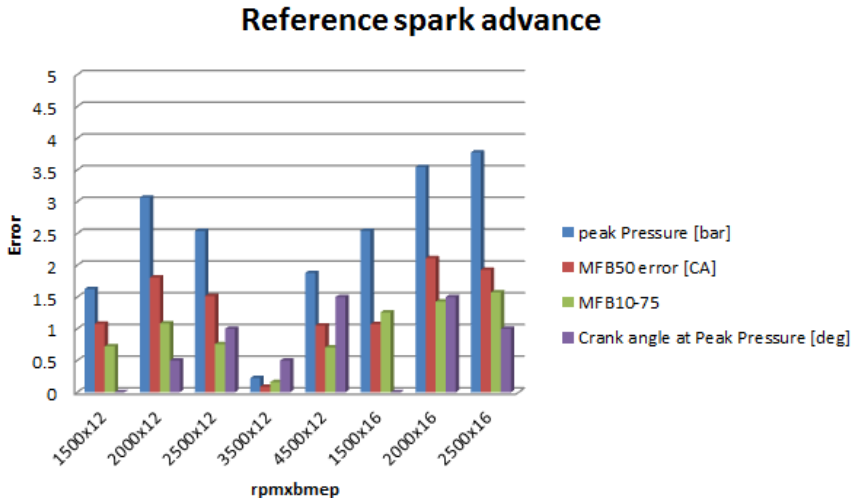

Figure 77. Absolute error between the predicted and experimental peak pressure, MFB50, burn duration (MFB10-75) and crank angle at peak pressure for various operating points and reference spark advances, Engine A

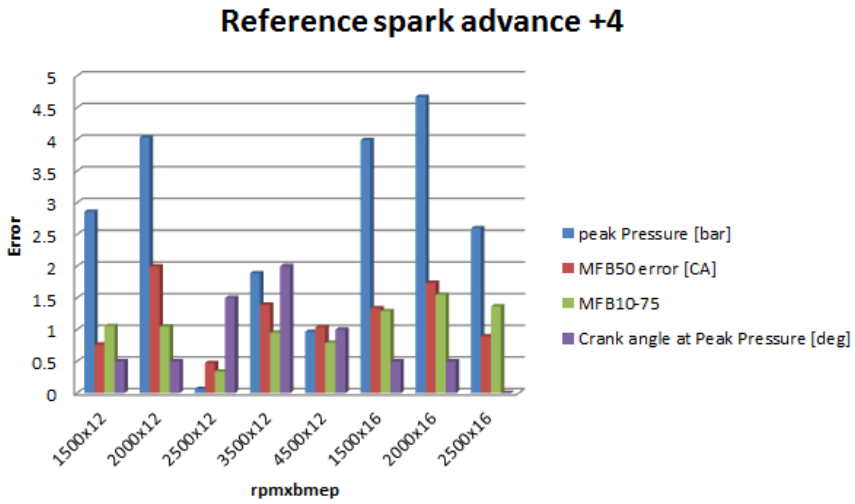

Figure 78. Absolute error between the predicted and experimental peak pressure, MFB50, burn duration (MFB10-75) and crank angle at peak pressure for various operating points and spark advance augmented by 4 CA from reference values, Engine A

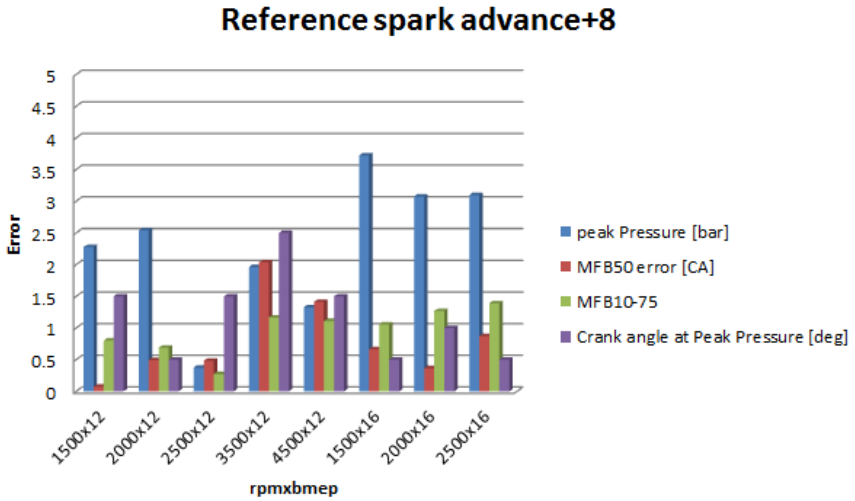

Figure 79. Absolute error between the predicted and experimental peak pressure, MFB50, burn duration (MFB10-75) and crank angle at peak pressure for various operating points and spark advance augmented by 8 CA from reference values, Engine A

Since, the engine is not always operating at the stochiometric condition, especially at high load and speed condition, it is often needed to enrich the mixture up to lambda equal to 0.7. Mixture enrichment is being used in order to mitigate knock and to maintain the Turbine Inlet Temperature (TIT) below 950 $°C$ which is a limit for turbine structure. That is why it is important to assess the capability of the model to capture the effect of lambda at different operating points. The analysis on Engine B shows that (Figure 80 and Figure 81) the IMEP error does not exceed 4% with the average error of 1% and the maximum pressure error does not exceed 6.4 bar with an average error of 2.16 bar.

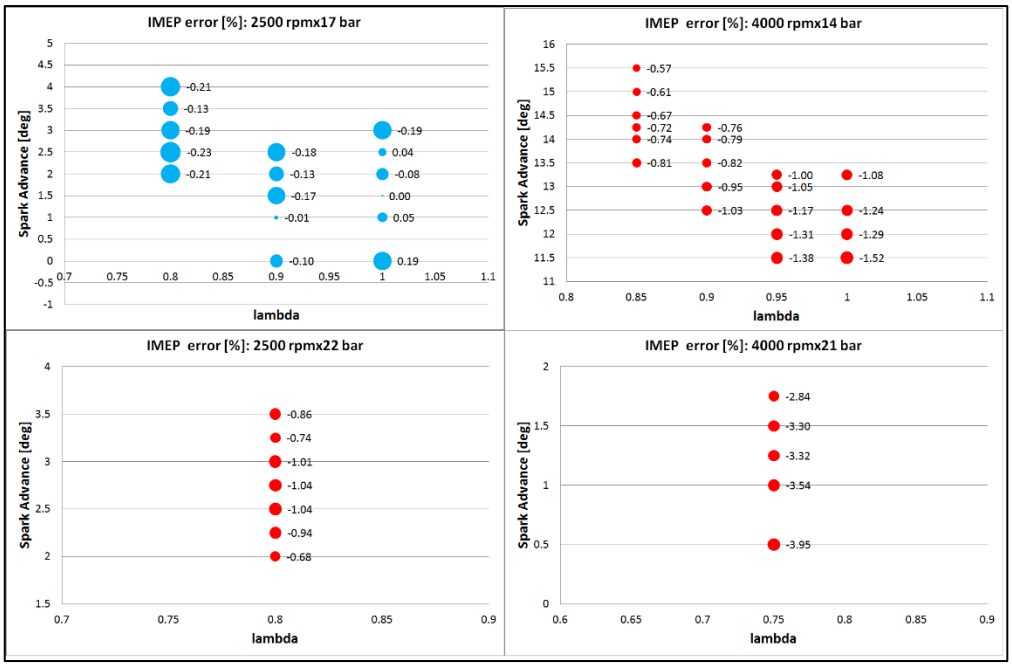

Figure 80. The percentage error between the experimental and simulated IMEP for different lambda, speed and load, Engine B

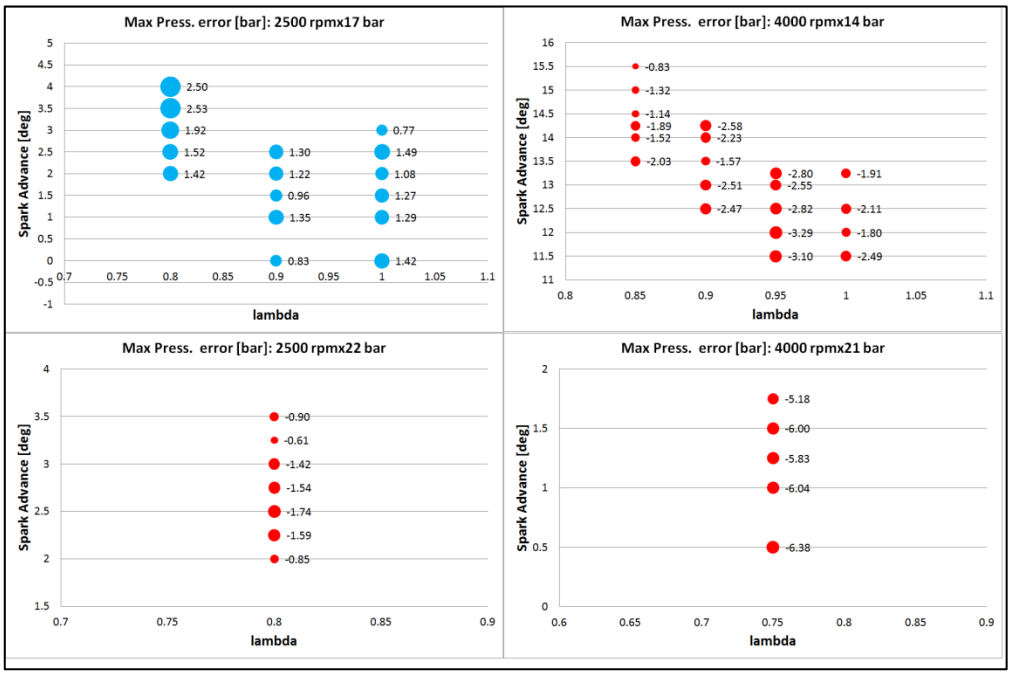

Figure 81. The percentage error between the experimental and simulated maximum pressure for different lambda, speed and load, Engine B

5.9.2.2 Effect of EGR

Exhaust Gas Recirculation (EGR) is another technology which is typically used at part and high load conditions for different purposes. The EGR could be either internal [29], [7] or external [10], [11] and [76]. The former is obtained by maintaining residual gas in the cylinder until the next combustion cycle. However, due to the high temperature of the residual gases, the improvement in terms of lowering the total charge temperature and therefore knock mitigation is minimal. The latter, external EGR, is defined as extraction of a portion of the exhaust flow towards the intake system. Cooled EGR system is one of the well-known strategies which have been used in SI gasoline engines to reduce NO_x emissions and surplus knock [77], [13]. The schematic representation of a Long Route (LR) EGR also referred to as low pressure loop EGR has been shown in Figure 82. This technology has been used in the experiment and it attempts to preserve turbocharger performance by supplying exhaust gas from a point downstream of the turbine; thus, allowing all the exhaust flow to be utilized in the turbine.

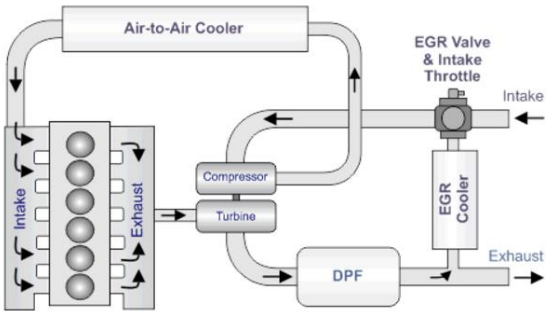

Figure 82. Low pressure loop EGR system for heavy-duty diesel engines [18]

The comparison between the simulated and experimental burn rate and pressure traces at different level of EGR for Engine C is shown in Figure 83, Figure 84, Figure 85 and Figure 86. It can be observed that the model is not only capable to capture the effect of EGR on the ignition delay but also is capable of capturing the effect of EGR on flame speed at the second stage of combustion.

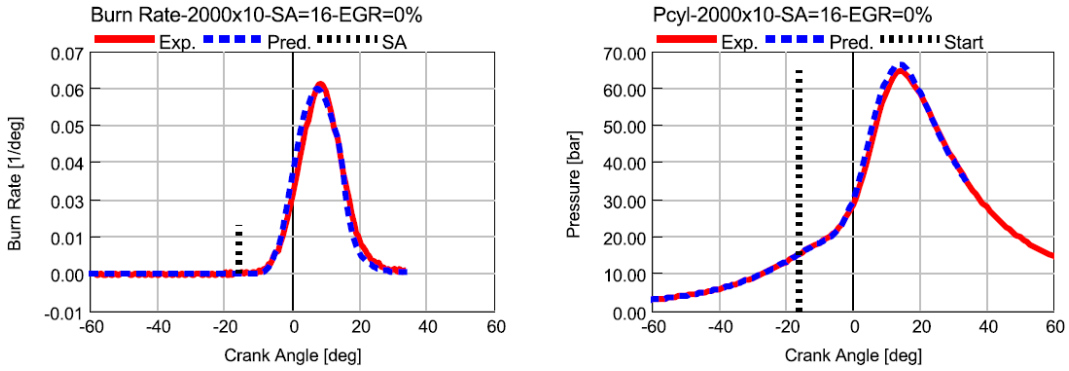

Figure 83. Simulated and experimental Burn rate and in-cylinder pressure comparison at 2000 rpm and EGR=0, Engine C

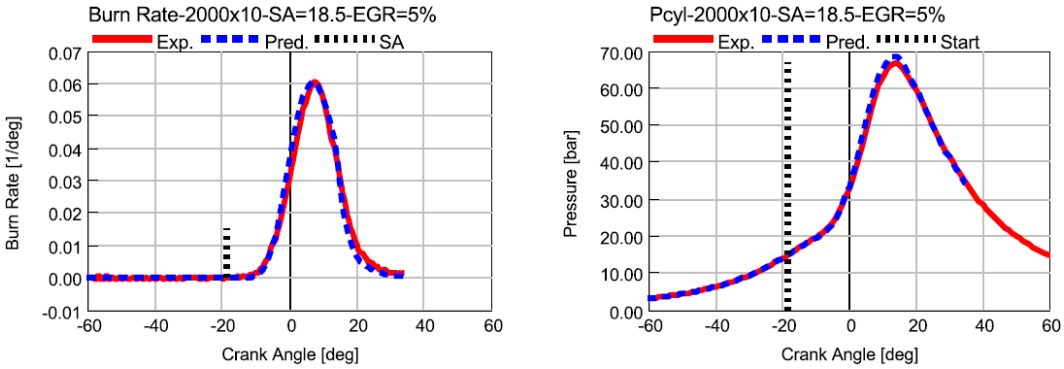

Figure 84. Simulated and experimental Burn rate and in-cylinder pressure comparison at 2000 rpm and EGR=5%, Engine C

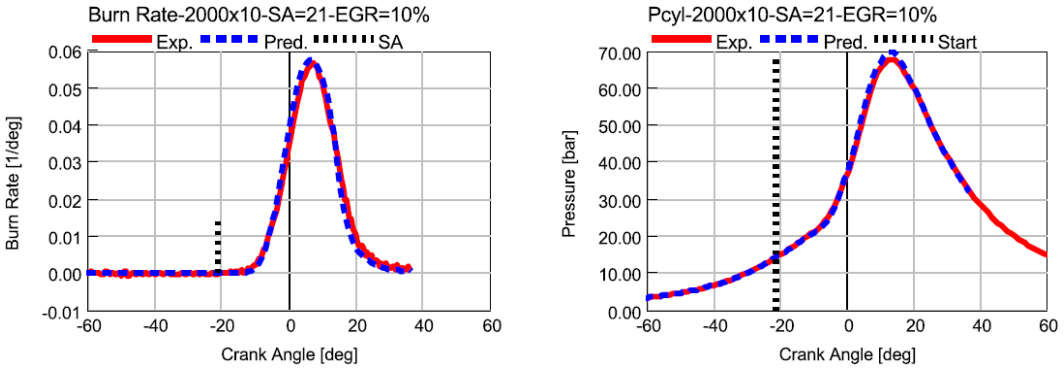

Figure 85. Simulated and experimental Burn rate and in-cylinder pressure comparison at 2000 rpm and EGR=15%, Engine C

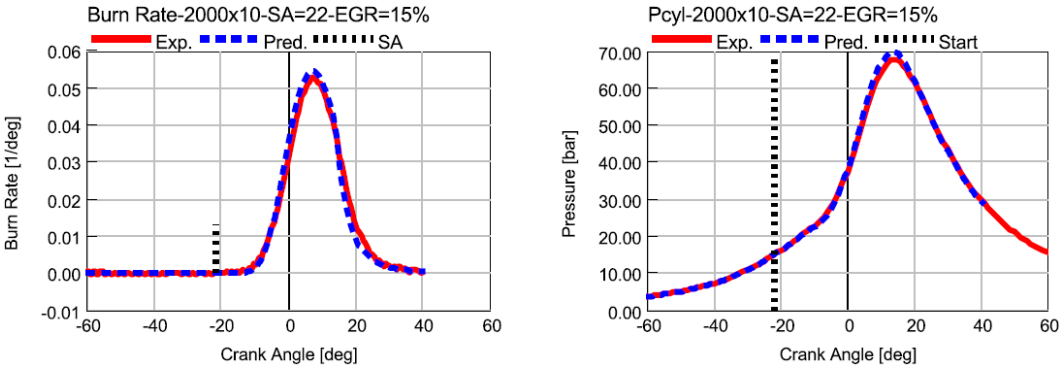

Figure 86. Simulated and experimental Burn rate and in-cylinder pressure comparison at 2000 rpm and EGR=15 %, Engine C

The comparison between the simulated and experimental IMEP is shown in Figure 87 and Figure 88 at different loads, speeds and EGR percentage which confirms the predictive capability and robustness of the model.

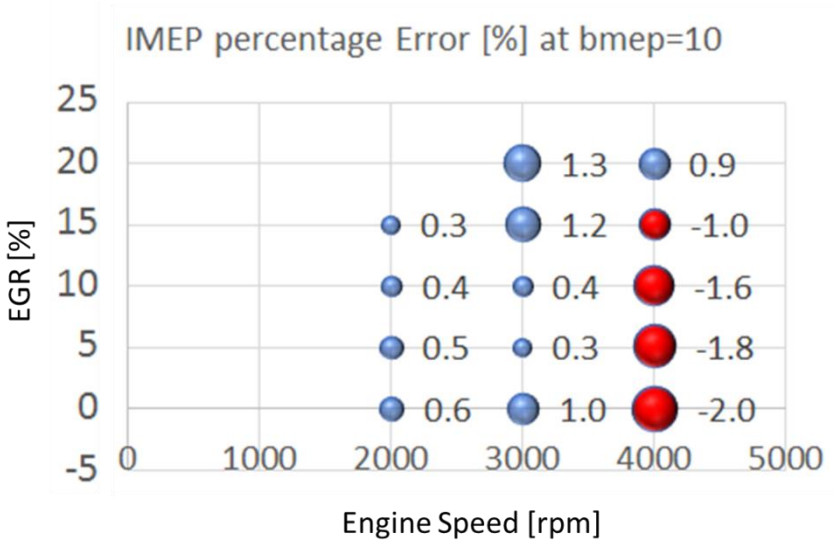

Figure 87. IMEP percentage error at various speed and EGR, bmep=10, Engine C

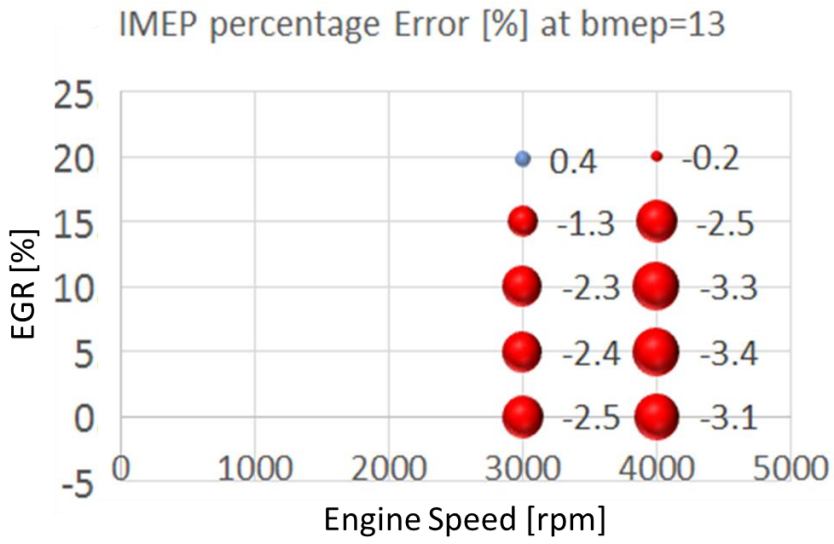

Figure 88. IMEP percentage error at various speed and EGR, bmep=13, Engine C

Moreover, as the amount of EGR increases the ignition delay increases because of its dilution effect. It can be observed from the Figure 89 that the prediction of ignition delay by the model shows a good agreement with the experiments.

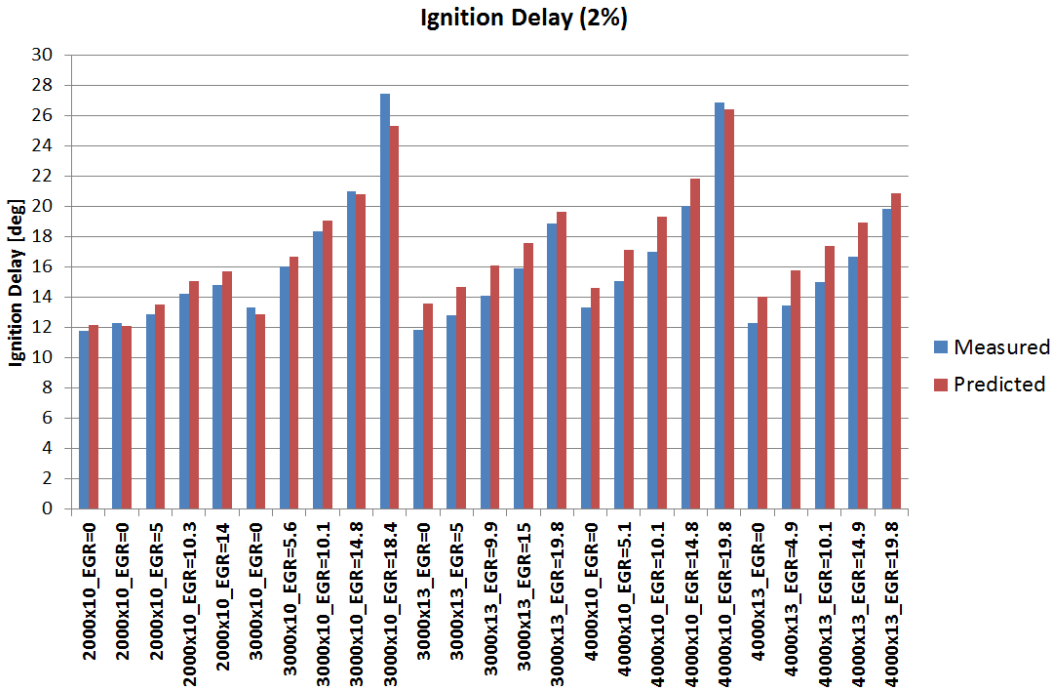

Figure 89. Comparison between predicted and measured ignition delay at different speed, load and EGR percentage, Engine C

5.9.2.3 Effect of water injection

Water injection is another promising technology for knock mitigation at higher load operating points. It can be seen from Figure 90 that the burn duration (MFB10-75) increases even by advancing the spark timing; therefore, the effect of slower flame propagation in the presence of the water should be considered. The analysis is performed on Engine C.

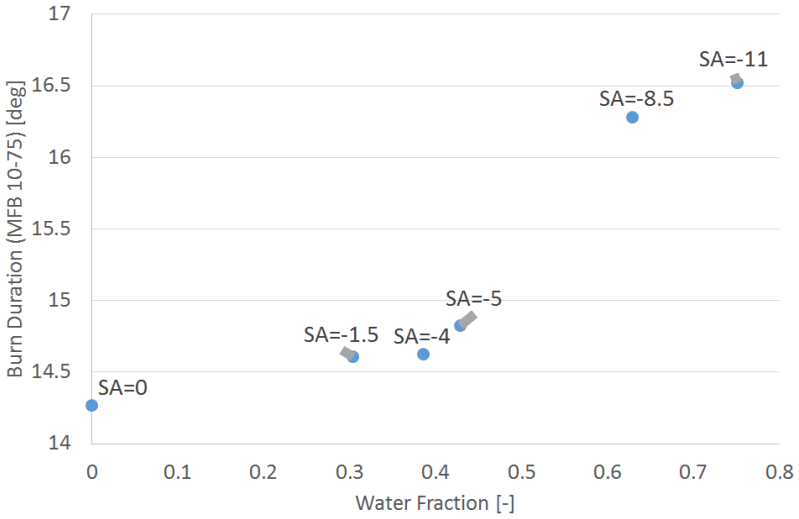

Figure 90. Burn Duration vs water injected at 2000 rpm x 15 bar bmep, Engine C

In order to model the effect of water injection on combustion, in addition to the C_s (defined in Equation 28), two additional constants have been added to the model namely C_{s1} and C_{s2} which are considered as scaling factors for the turbulent flame speed; therefore, turbulent flame speed is written as Equation 40. It should be noted that this approach is a preliminary analysis which is a fitting procedure aiming to match the turbulent combustion model with the experimental burn rate. However, the physical modelling of the effect of water on slowing down the combustion duration is to understand how the laminar flame speed is affected by the charge dilution and the temperature in the presence of water.

$$S_T = (C_{s1}WF^2 + C_{s2}WF + C_s)u'(1 - \frac{1}{1 + \frac{C_k R_f^2}{L_t^2}}) \quad (40)$$

It is noteworthy that the injected water may not evaporate completely and can remain as a film layer in the intake port or can cause lubricant oil dilution by impacting on the cylinder liner. In the 0D/1D model, it is assumed that 100% of the water will be evaporated at the spark timing. (Equation 41); however, 3D-CFD simulation, presented in Section 4.3, showed that only a portion of water will be evaporated in the cylinder and so further refinements of the model will be needed.

$$Turbulent\ Flame\ Speed\ Multiplier = C_{s1}WF^2 + C_{s2}WF + C_s \quad (41)$$

It is worth mentioning that the operating points at 2000 rpm x 15 bar bmep and different water to fuel ratios are used for the calibration of the model and 4000 rpm x 17 bar bmep and different water to fuel ratios are used for validation to show the predictive capability of the model.

Due to the high latent heat of water, the intake charge is cooled down and it reduces the possibility of knock; moreover, the presence of water vapor also slows down the flame propagation inside the cylinder. The burned fuel fraction at two different speeds has been depicted in Figure 91. It can be observed that the combustion is getting slower with the same SA and higher water to fuel fraction and this effect could be fairly captured by the model.

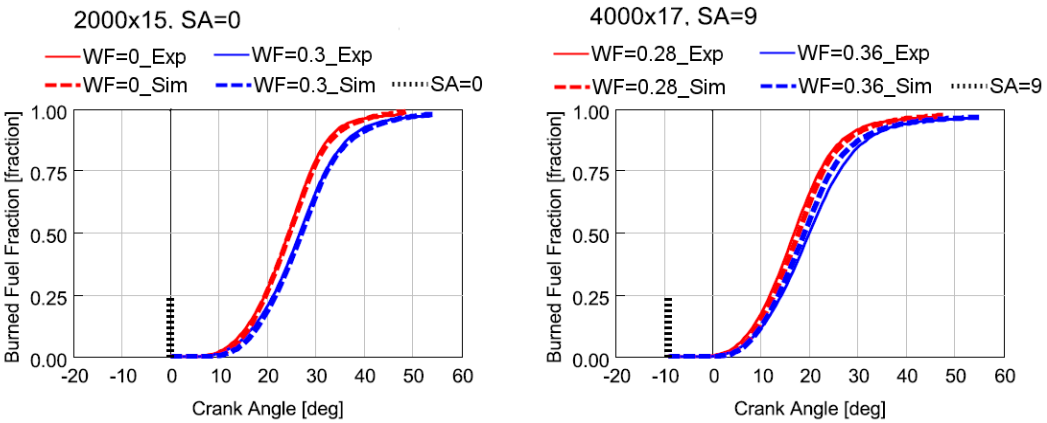

Figure 91. Comparison of experimental and simulated mass fraction burned at same SA and different water to fuel ratio at 2000 rpm x 15 bar bmep and 4000 rpm x 17 bar bmep, Engine C

The comparison between simulated and experimental burn rate has been depicted in Figure 92, Figure 93, Figure 94 and Figure 95 for various spark advances, water to fuel fractions, loads and speeds.

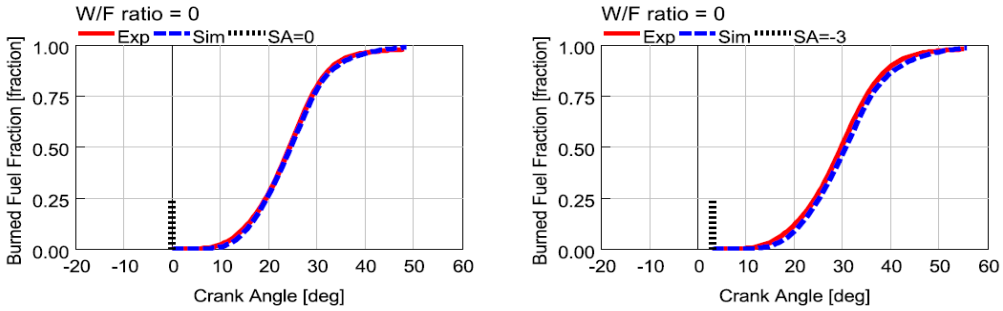

Figure 92. the comparison between the simulated and experimental burned fuel fraction at W/F=0 and different SA at 2000 rpm x 15 bar bmep , Engine C

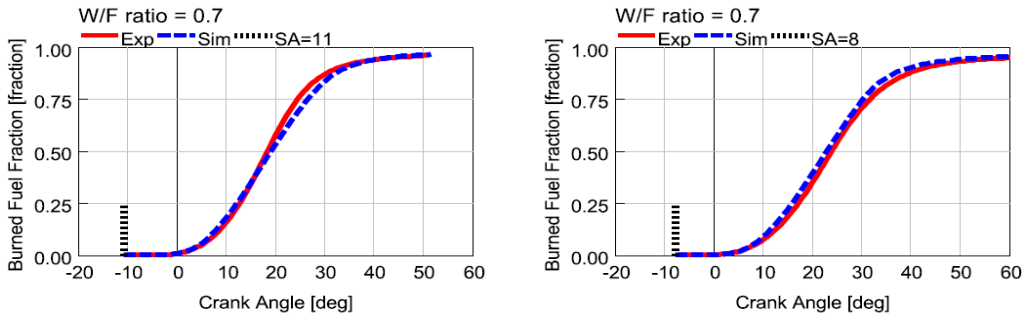

Figure 93. the comparison between the simulated and experimental burned fuel fraction at W/F=0.7 and different SA at 2000 rpm x 15 bar bmep, Engine C

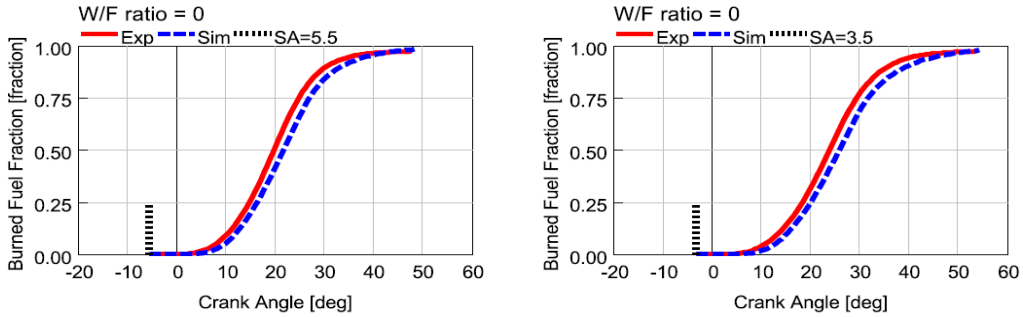

Figure 94. the comparison between the simulated and experimental burned fuel fraction at W/F=0 and different SA at 4000 rpm x 17 bar bmep, Engine C

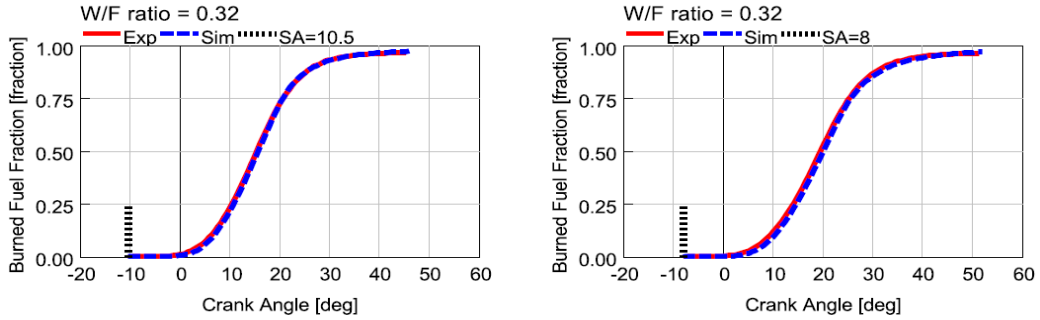

Figure 95. the comparison between the simulated and experimental burned fuel fraction at W/F=32 and different SA at 4000 rpm x 17 bar bmep, Engine C

The resulted IMEP percentage errors between experimental and simulation at 2000 rpm x 15 bar bmep and 4000 rpm x 17 bar bmep are depicted in Figure 96 and Figure 97, respectively. It can be realized that the absolute average error is equal to 1.74% which confirms the robustness and reliability of the model.

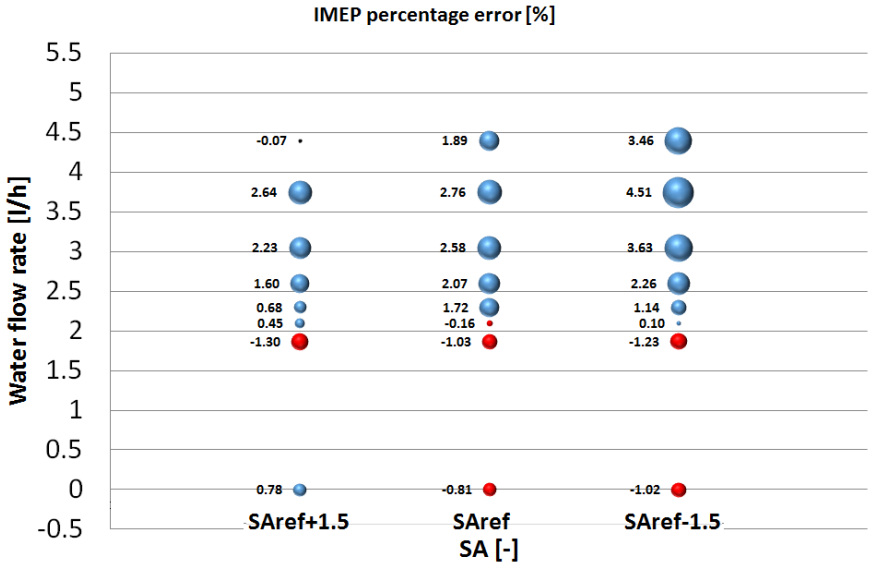

Figure 96. The percentage error between the experimental and simulated IMEP at 2000 rpm x 15 bar bmep considering sweep of SA and water flow rate, Engine C

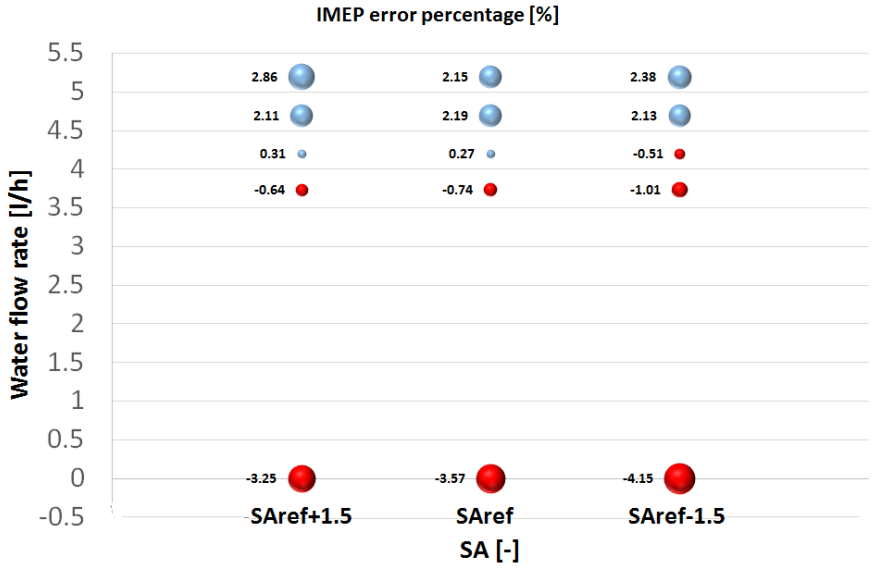

Figure 97. The percentage error between the experimental and simulated IMEP at 4000 rpm x 17 bar bmep considering sweep of SA and water flow rate, Engine C

The errors between measured and simulated MFB50, burn duration from 10 to 75 (MFB10-75) at 2000 rpm x 15 bar bmep and 4000 rpm x 17 bar bmep are shown in Figure 98, Figure 99, Figure 100 and Figure 101, respectively.

It is noteworthy that the average errors for MFB50 and MFB10-75 are 0.82 and 0.86 respectively confirming the good predicting capability of the model. It is worth mentioning that is possible to give some speed and load functions to the calibration parameters to achieve better accuracy but it jeopardizes the aim of this work which is the utilization of one set of parameters for all operating points.

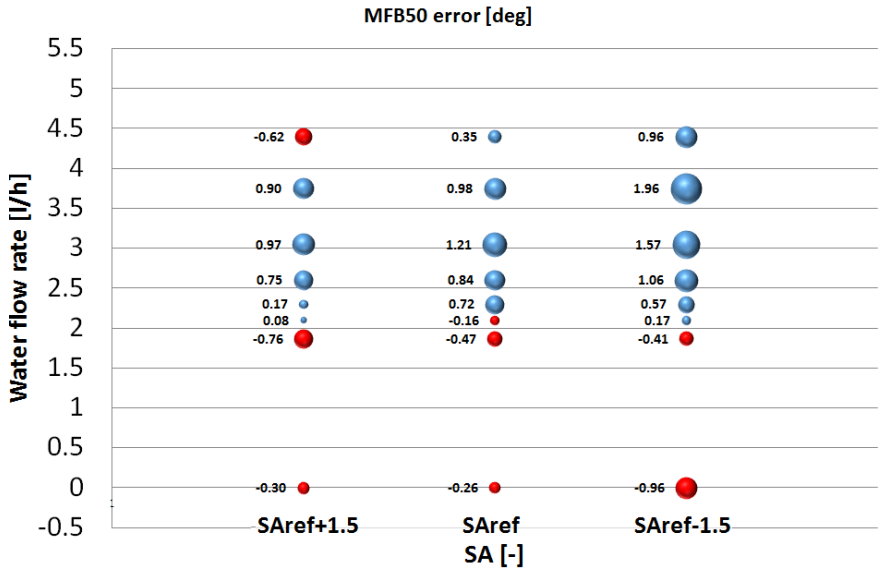

Figure 98. The percentage error between the experimental and simulated MFB50 at 2000 rpm x 15 bar bmep considering sweep of SA and water flow rate, Engine C

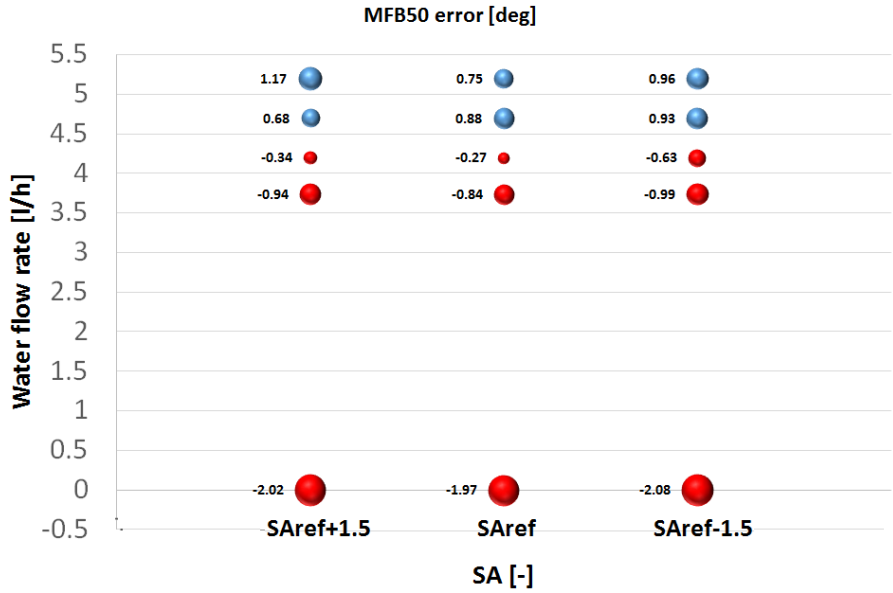

Figure 99. The percentage error between the experimental and simulated MFB50 at 4000 rpm x 17 bar bmep considering sweep of SA and water flow rate, Engine C

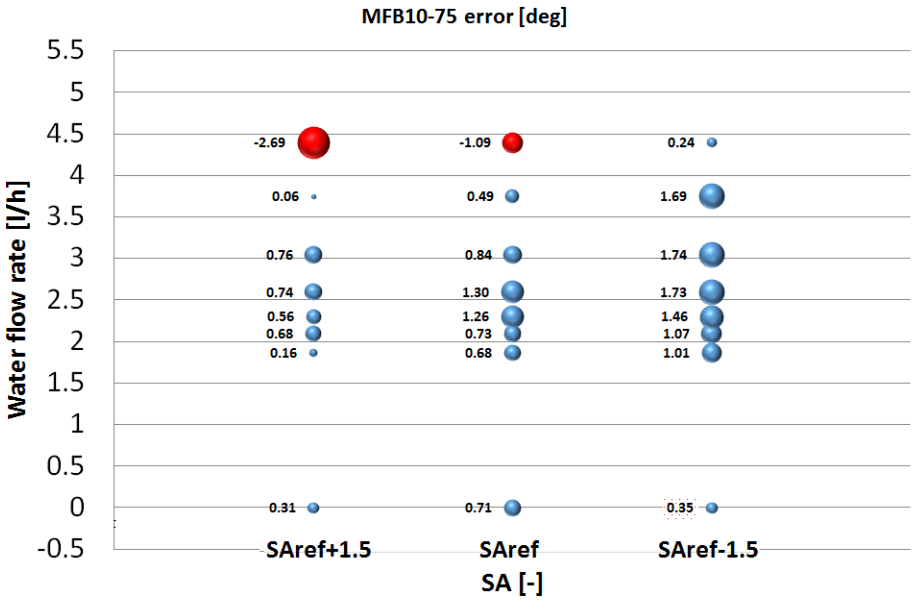

Figure 100. The percentage error between the experimental and simulated MFB10-75 at 2000 rpm x 15 bar bmep considering sweep of SA and water flow rate, Engine C

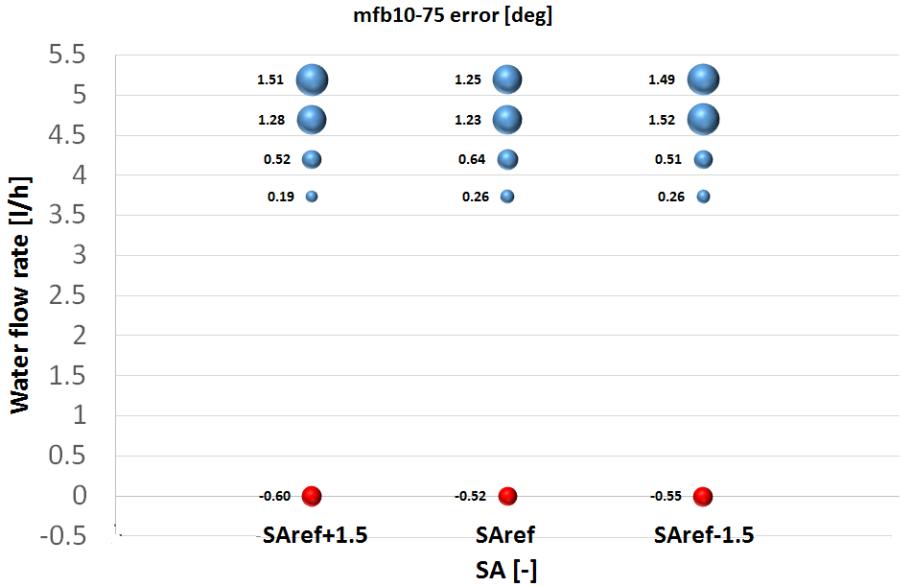

Figure 101. The percentage error between the experimental and simulated MFB10-75 at 4000 rpm x 17 bar bmep considering sweep of SA and water flow rate, Engine C

5.9.3 CCV model results

After showing the capability of the model for prediction of mean cycle, presented in Section 5.9.2, the procedure explained in Section 5.7 is adopted to mimic CCV. More in detail, in order to show the predicting capability of the model, the COV of IMEP and peak pressure for Engine A have been depicted in Figure 102 and Figure 103 which have satisfactory agreement with the experimental data.

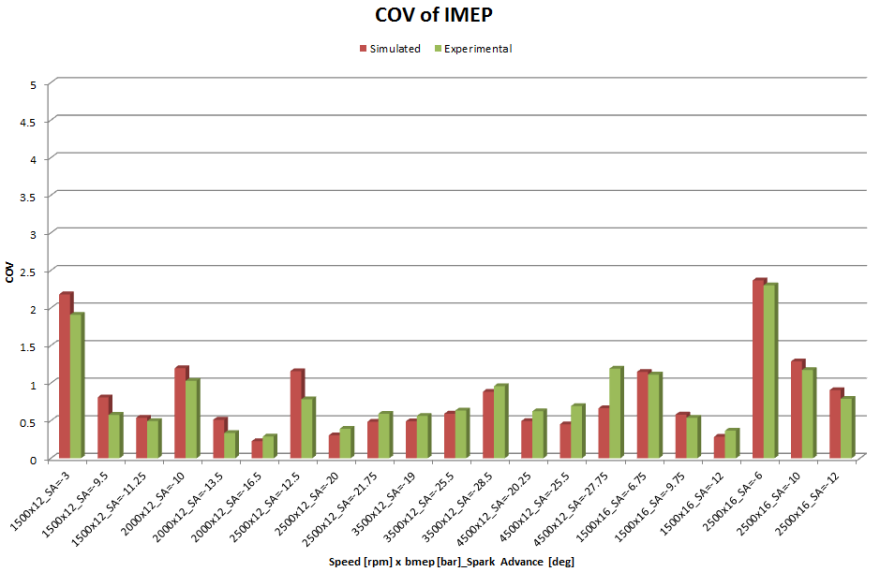

Figure 102. The COV of IMEP at different operating points (red: simulated, green: experimental), Engine A

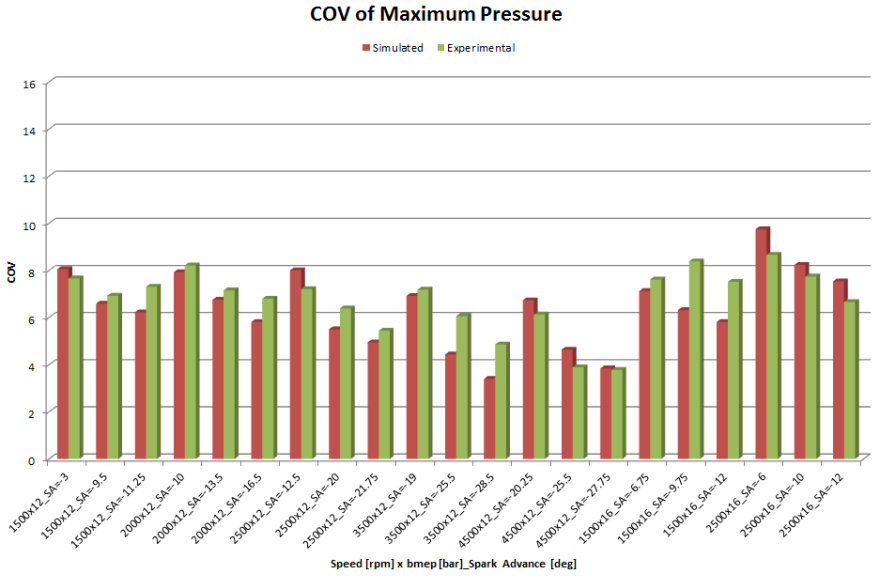

Figure 103. The COV of peak pressure at different operating points (red: simulated, green: experimental), Engine A

The model is also capable of predicting the variation of different stages of combustion. The COV and standard deviation of MFB10-75 and MFB50 have been depicted in Figure 104 and Figure 105 respectively, which indicates an acceptable accuracy.

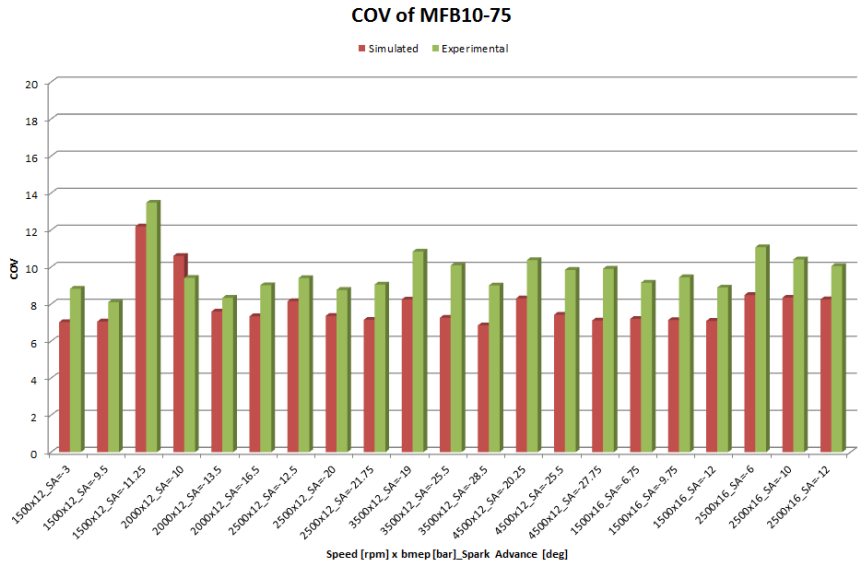

Figure 104. The COV of MFB10-75 at different operating points (red: simulated, green: experimental), Engine A

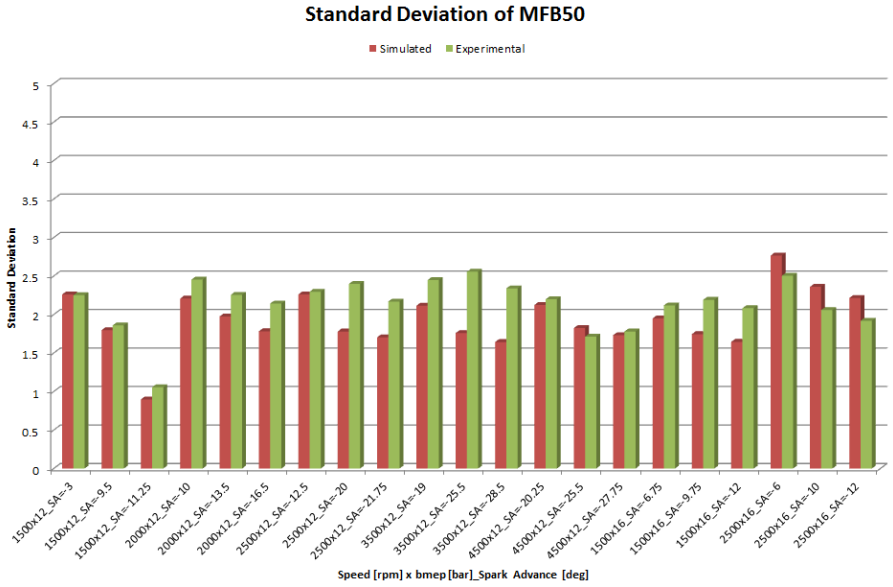

Figure 105. The standard deviation of MFB50 at different operating points (red: simulated, green: experimental), Engine A

5.10 Knock prediction

Among the different knock prediction models, the Douaud and Eyzat model discussed in Section 5.8.2 was used. In the 0D GT-SUITE model, the Induction Time Multiplier (ITM) and the Activation Energy Multiplier (AEM), Equation 39, are the two calibration parameters of the model. The comparison between simulated

and experimental percentage of knocking cycles is shown in Figure 106 at 2500 rpm x 16 bar bmep, stoichiometry air to fuel ratio (base point, Engine A).

Since the spark timing sweeps at the base operating points of Engine A are acquired with the large increment it is not possible to define the experimental KLSA at all operating points; hence, the experimental data acquired with different water to fuel ratio of Engine C has been utilized for this purpose in which the spark timing sweeps have been carried out with a short increment and the KLSA could be detected.

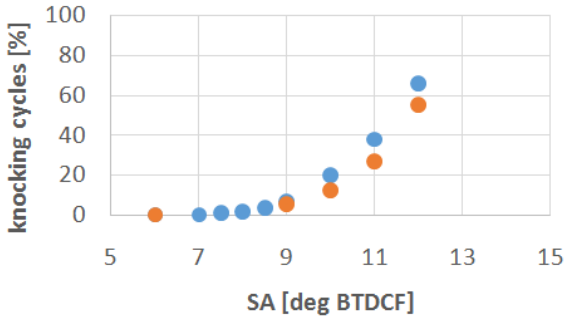

Figure 106. Comparison between simulated and experimental percentage of knocking cycles at 2500 rpm x 16 bar bmep, lambda=1, Engine A

In order to calibrate the knock model, for the sake of simplicity, the ITM parameter is set to unity and the calibration was carried out tuning the AEM parameter which was found to be 0.945 and was kept constant for all the engine map operating points.

It can be seen from Figure 107 and Figure 108 that as the amount of injected water is increasing the knock probability is decreased and the KLSA is increased. Moreover, it can be observed that the model is capable to predict the trend both quantitatively and qualitatively fairly well.

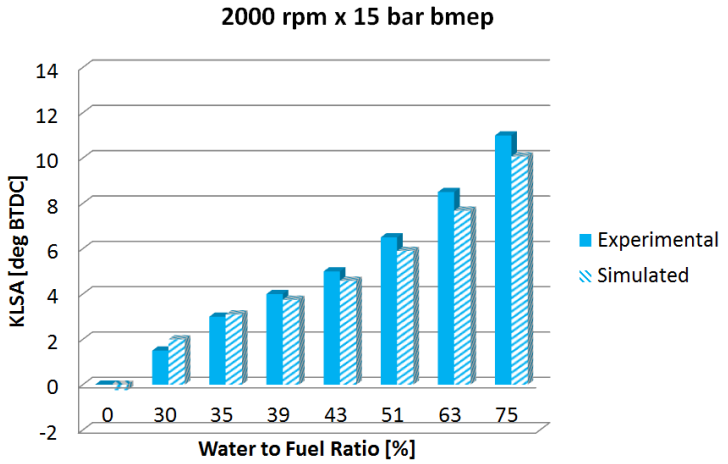

Figure 107. Comparison between the simulated and experimental Knock Limited Spark Advance (KLSA) at 2000 rpm x 15 bar bmep, Engine C

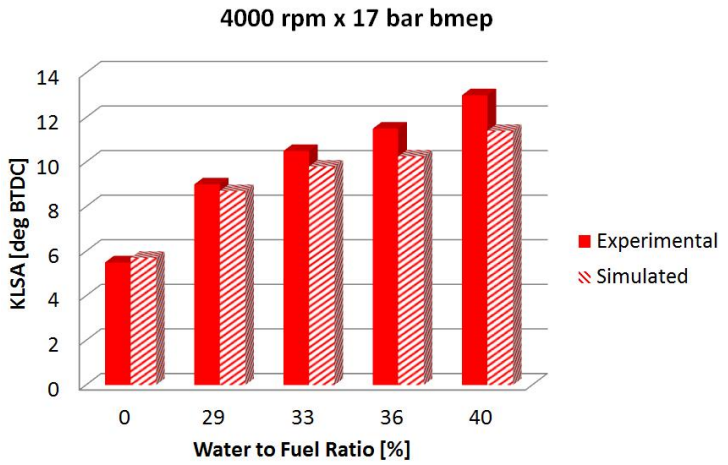

Figure 108. Comparison between the simulated and experimental Knock Limited Spark Advance (KLSA) at 4000 rpm x 17 bar bmep, Engine C

The absolute error between predicted and experimental KLSA is reported in Table 5. It can be observed that the maximum error is 1.49 and the average one is 0.53 which indicates the good predictive capability of the model.

Table 5. Absolute error between simulated and experimental KLSA, Engine C

Engine Speed [rpm]	Water to Fuel Ratio	KLSA Absolute Error
2000	0	1.14
2000	0.3	1.49
2000	0.35	0.77
2000	0.38	0.42
2000	0.42	0.03
2000	0.5	0.20
2000	0.62	0.25
2000	0.75	0.38
4000	0	0.11
4000	0.28	0.01
4000	0.32	0.42
4000	0.36	0.62
4000	0.4	1.01

Parte del lavoro descritto in questo capitolo è stato anche preventivamente pubblicato in:

Part of the work described in this Chapter was also previously published in the following publications:

1. Zhao, E., Moiz, A.A., Sibendu, S., Fogla, N., Bybee, M., Wahiduzzaman, S., Mirzaeian, M., Millo, F., Kodavasal, J., "Examining the Role of Flame Topologies and In-cylinder Flow Field on Cyclic Variability in SI Engines Using Large Eddy Simulation", International Journal of Engineering Research (IJER), 2017.

2. Zhao, E., Moiz, A.A., Sibendu, S., Fogla, N., Bybee, M., Wahiduzzaman, S., Mirzaeian, M., Millo, F., Kodavasal, J., "Multi-cycle Large Eddy Simulation to Capture Cycle-to-Cycle Variation (CCV) in Spark-Ignited (Si) Engines", 10th US National Combustion Meeting, 2017.

3. Mirzaeian, M., Millo, F., Fogla, N., Bybee, M., Wahiduzzaman, S., Kodavasal, J., et al., "Modeling and Understanding Cycle-to-Cycle Variation Through Multi-Cycle LES", CONVERGE CFD User Conference, Vienna, 2017.

Chapter 6

Large Eddy Simulation

6.1. Introduction

The 3D-CFD approach is typically being utilized to simulate various phenomenon in internal combustion engines (ICE) in order to analyze the flow motion, spray and combustion. Reynolds Averaged Navier-Stokes (RANS) model [78], [79] is a standard method to simulate the turbulence flow in internal combustion engines; however, this approach is based on ensemble averaged governing equations; hence, it is not capable of predicting the local unsteadiness in the flow and CCV in SI engines. Another approach which has been introduced recently is Large Eddy Simulation (LES) [80] in which the large scale flow structures are resolved while small scale eddies can be considered to be isotropic and are therefore modeled. LES can be exploited to identify physical quantities which are varied from cycle to cycle in order to understand the root cause of CCV. Previous LES studies [81],[82] and [83] indicated a strong impact of in-cylinder flow variations on combustion processes. Enaux et al. [82] stated that variations in the velocity field at the spark plug control the initial growth of the flame and decide a large extent on the entire combustion duration.

The present chapter aims to achieve, through LES, a better understanding of the root cause of CCV. The LES simulation was performed at Argonne National Labaratory (ANL), IL, USA in collaboration with Gamma Technologies, IL, USA and Politecnico di Torino, Italy.

6.2. Numerical setup

The liquid spray is modeled as dispersed phase in Lagrangian framework and the surrounding air is modeled as continuous phase in Eulerian framework. In order to track the turbulent flame front using LES, the dynamic structure model with one equation has been utilized. The description of this model has been given in [84].

The G-Equation model in which the premixed turbulent combustion occurs in either the corrugated flamelet or the thin reaction zone regime, is used in the current study. The turbulence flame speed for the LES simulation can be calculated by Equation 42. The parameter b_3 has been adjusted in order to capture the trend of the experimental measurements and it was fixed for the entire simulation.

$$s_t = s_l\left(\frac{{b_3}^2 C_{s,dynamic}}{2b_1 Sc}\frac{\Delta}{l_F} + \sqrt{\left(\frac{{b_3}^2 C_{s,dynamic}}{2b_1 Sc}\frac{\Delta}{l_F}\right)^2 + \frac{{b_3}^2 D_1}{s_l l_F}} + 1\right) \qquad (42)$$

Where:

- s_l is the laminar flamespeed
- b_1 and b_3 are modeling constants
- $C_{s,dynamic}$ is the dynamic Smagorinsky number
- Sc is the turbulent Schmidt number
- Δ is the filter width
- l_F is the length scale

The laminar flame speed can be calculated by the Metghalchi and Keck correlation [85] which is expressed as Equation 43:

$$s_{l,ref} = B_m + B_2(\emptyset - \emptyset_m)^2 \qquad (43)$$

In which $\emptyset$ is the equivalence ratio, B_m, B_2, and $\emptyset_m$ are tuning constants appropriate for the specific fuel and oxidizer used in the simulation.

The base cell size is 2.8 mm both in intake and exhaust ports. Adaptive mesh refinement (AMR) was used to automatically refine the grid based on fluctuating gradients of velocity, so the base grid size in cylinder region is 0.7 mm. Furthermore, different levels of embedding were applied to cylinder and spark plug region. the computational domain for LES simulation on the engine case is composed by approximately 7 million cells at intake port and 1 million cells at TDC. The simulation was run with 96 cores.

As it is indicated in Figure 109 and Figure 110, the results indicate that COV of quantities from LES are comparable to experiments.

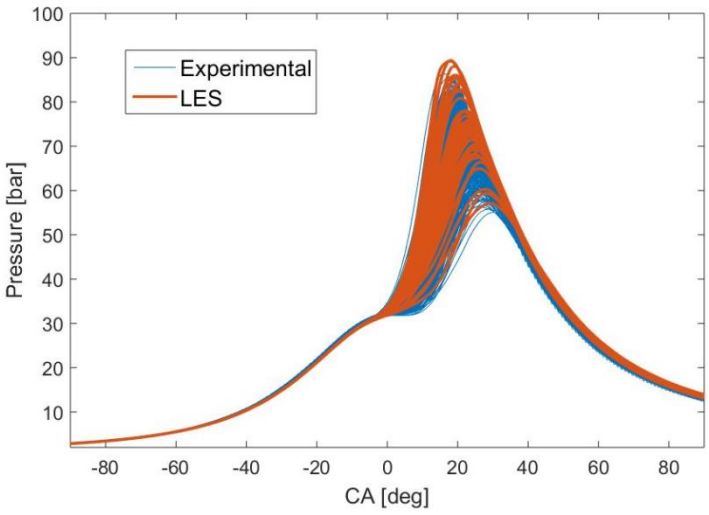

Figure 109. In-cylinder pressure trace comparison between simulation and experiment

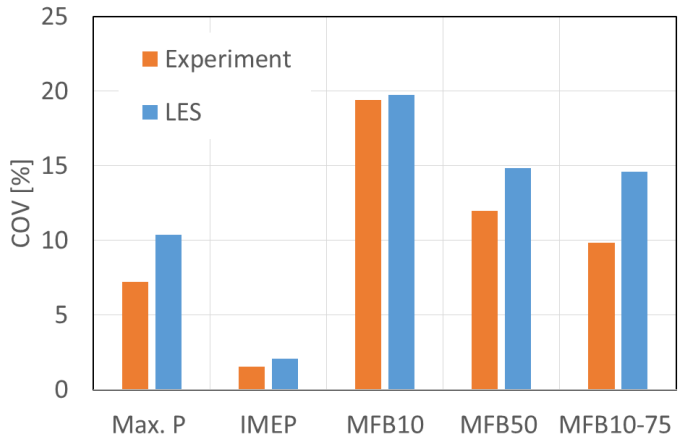

Figure 110. Comparison between different quantities between LES and experiment

6.3. CCV analysis using LES

6.3.1. Possible cause of CCV

After the cycle by cycle analysis of the in-cylinder pressure data coming from LES, it is observed (Figure 111) that early burn phase plays the key role on cycle to cycle variation and most cycles that start burning fast, continue to burn faster.

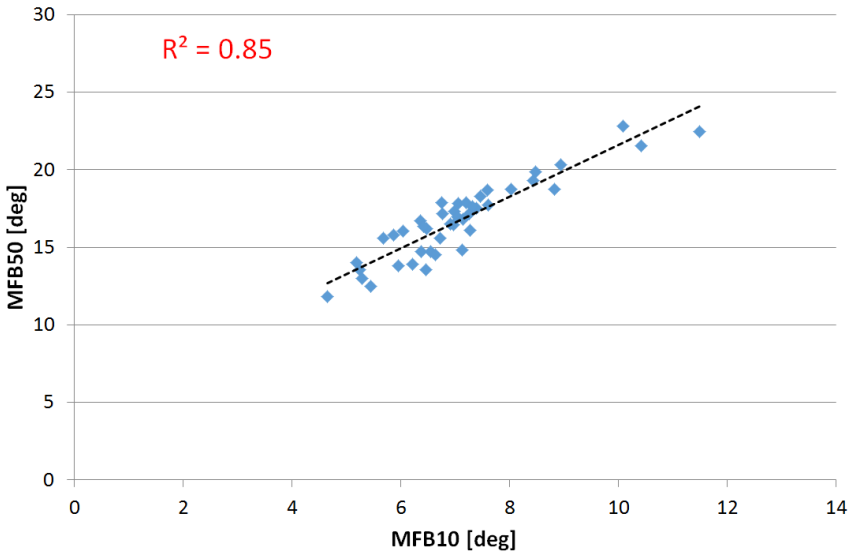

Figure 111. The correlation of MFB50 and MFB10 coming from LES

Potentially, CCV could be related to:

- In-cylinder flow variations (bulk flow and turbulence)
- Composition inhomogeneity
- A combination of the two

In order to understand the effect of velocity and mixture inhomogeneity on CCV cycle 4 and 5 which are fast and slow cycles respectively, are selected. The equivalence ratio and velocity field 1 degree before spark timings for cycle 4 and 5 are depicted in Figure 112 and Figure 113, respectively.

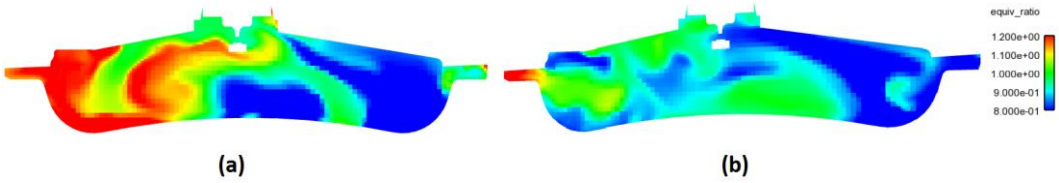

Figure 112. a) Equivalence ratio distribution in cycle 4 one degree before the spark timing; b) Equivalence ratio distribution in cycle 5 one degree before the spark timing

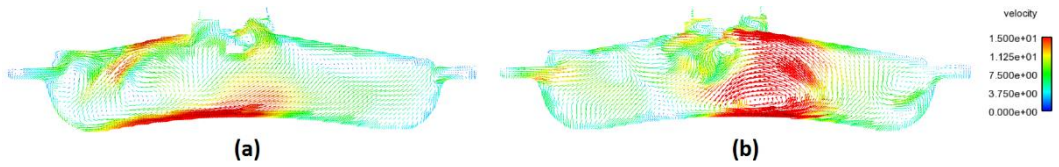

Figure 113. a) Velocity field in cycle 4 one degree before the spark timing; b) Velocity field in cycle 5 one degree before the spark timing

In order to understand which one (effect of mixture inhomogeneity and flow) has the dominant effect on CCV, the velocity field effect from the equivalence ratio distribution is decoupled numerically. It should be noted that computer simulations afforded the unique ability to decouple these naturally co-occurring phenomena; something which is not possible in experiments.

In order to evaluate the effect of velocity field, Cycle 4 until 710 degrees was run and map file at this point was written. This is just prior to ignition, which is at 711 degrees. The map file contains the spatial distribution of velocity, sub-grid turbulent kinetic energy, temperature, pressure, and composition. Now, Cycle 4 is restarted from this point by mapping all the quantities except the velocity field from this map file. For the velocity field, a map file generated by running Cycle 5 until 710 degrees was used which therefore allows to isolate the effect of velocity field differences between the two cycles. It can be observed from Figure 114 that Cycle 4 with the velocity field of Cycle 5 varies significantly and gets close to the original Cycle 5's in-cylinder pressure trace.

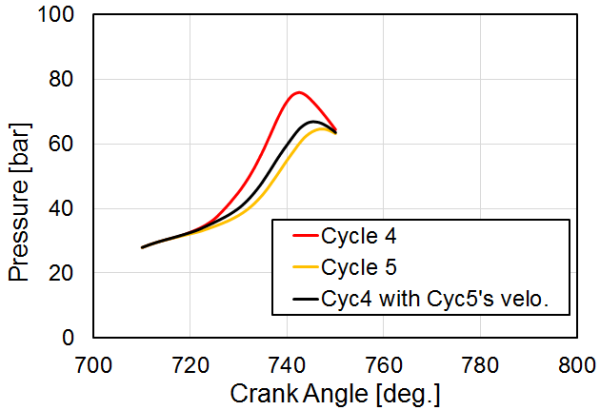

Figure 114. The comparison between cycle 4, 5 and cycle 4 with cycle 5's velocity field

Similarly, in order to evaluate the effect of composition inhomegenity Cycle 4 until 710 degrees was run and map file at this point was written and Cycle 4 was restarted from this point by mapping all the quantities except the composition field from this map file. For the composition field, a map file generated by running Cycle 5 until 710 degrees was used, which isolates the effect of composition field differences between the two cycles. It can be observed from Figure 115 that when Cycle 4 (pressure trace shown with a red line) is restarted from 710 degrees with Cycle 5's composition field (but with temperature, velocity, pressure, and sub-grid turbulent kinetic energy from Cycle 4), the resulting pressure trace (black dotted line) aligns still more closely to that of Cycle 4 (red line).This numerical study suggests that the velocity flow-field at spark timing has a strong effect on the flame kernel development which is the primary mechanism that causes CCV for this operating point.

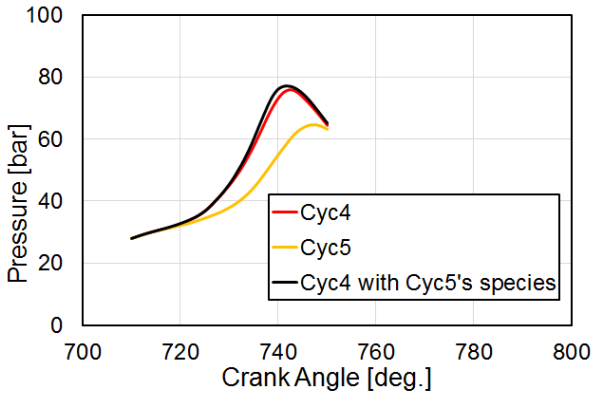

Figure 115. The comparison between cycle 4, 5 and cycle 4 with cycle 5's species

More in detail, it could be appreciated (Figure 116 and Figure 117) that the flame grows in one direction which causes smaller surface and turbulent flame speed; however, it is shown in Figure 118 and Figure 119 that the flame is growing almost evenly in all the directions which leads to higher turbulent flame speed.

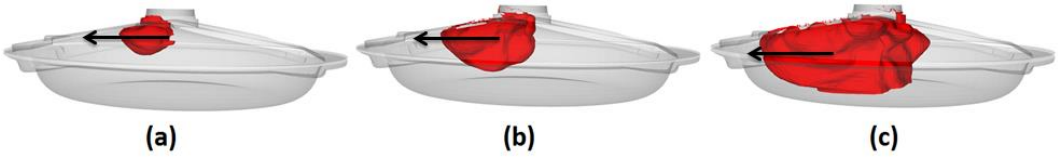

Figure 116. Front view of the flame at cycle 5 at a) 5 degree after SA; b) 10 degree after SA; c) 15 degree after SA

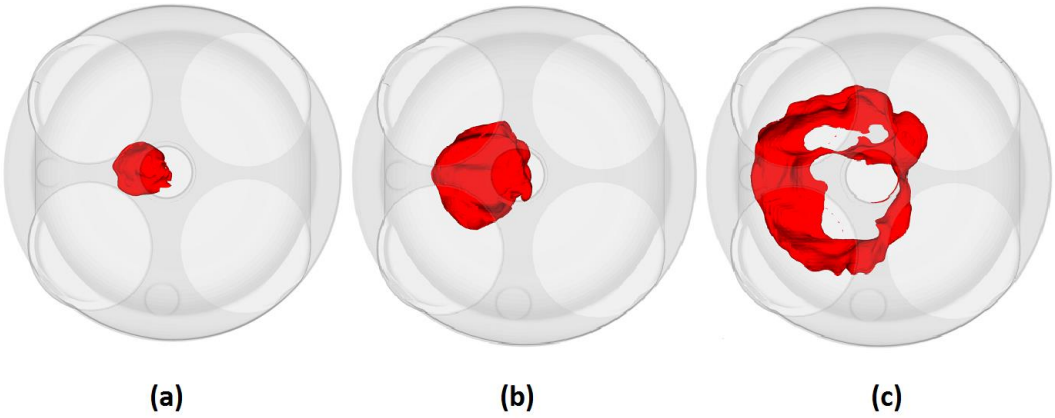

Figure 117. Top view of the flame at cycle 5 at a) 5 degree after SA; b) 10 degree after SA; c) 15 degree after SA

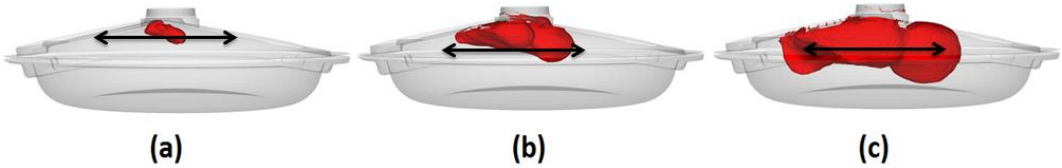

Figure 118. Front view of the flame at cycle 4 at a) 5 degree after SA; b) 10 degree after SA; c) 15 degree after SA

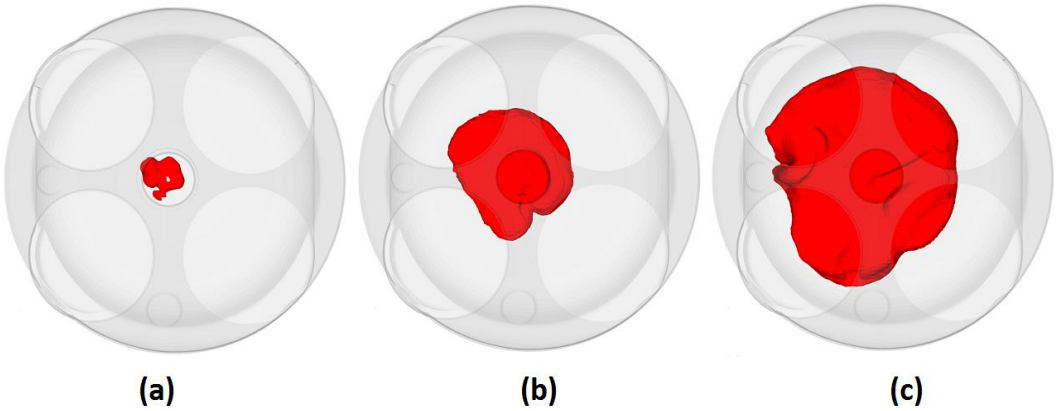

Figure 119. Front view of the flame at cycle 4 at a) 5 degree after SA; b) 10 degree after SA; c) 15 degree after SA

The next step is focused on finding a relationship between the flow field near the spark plug and turbulence level inside the cylinder. In the LES concept only the smaller scales are modelled, the sub-grid turbulent kinetic energy is a small fraction of the total TKE inside the cylinder. Therefore, it is important to take into account the resolved TKE as well. In order to focus on the velocity field near the spark plug, 6 different monitor volumes with various radius near the spark plug (Figure 113) is considered. Each component of velocity is considered as the mean plus a fluctuation which can be written as Equation 44:

$$x = < x > + x' \tag{44}$$

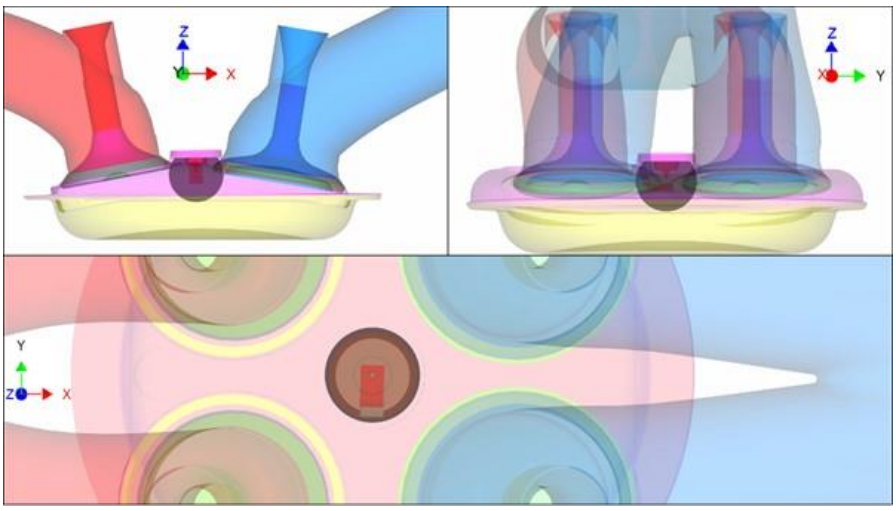

Figure 120. Monitor volume for evaluating average velocities in the X, Y, and Z directions prior to ignition. Note that the negative X direction (towards the exhaust) represents the direction of the mean flow created by tumble.

Where x is the velocity component in x, y and z directions. The filtering technique with a cut-off frequency equal to the engine frequency has been considered in order to decouple the mean and turbulence flow field. The high frequency filtering leads to the calculation of resolved turbulence (x') while the low frequency gives the mean portion of the velocity $(< x >)$. The mean flow contribution for cycle 4 and 5 is depicted in Figure 121 and Figure 122, respectively; while the turbulence flow contribution for cycle 4 and 5 is depicted in Figure 123 and Figure 124, respectively.

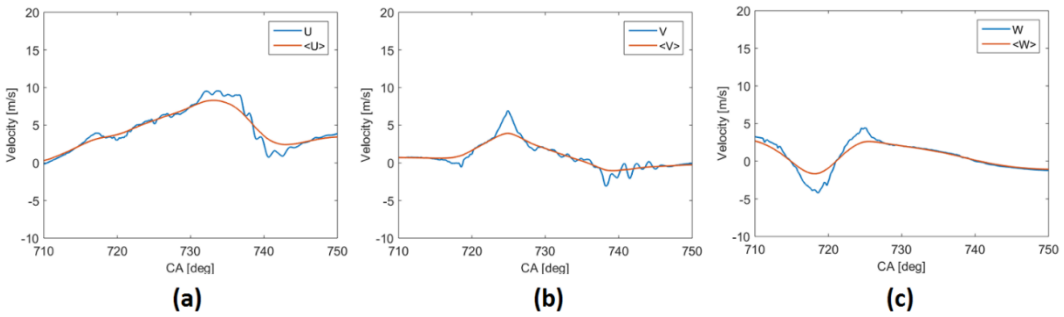

Figure 121. The mean contribution of velocity versus the velocity at different directions for cycle 4

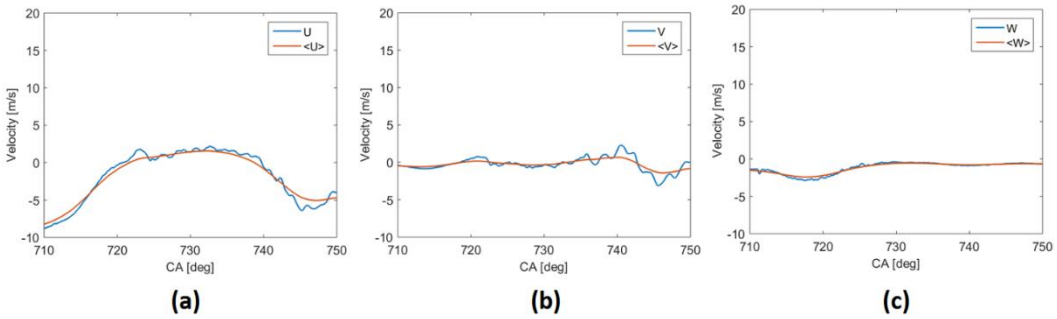

Figure 122. The mean contribution of velocity versus the velocity at different directions cycle 5

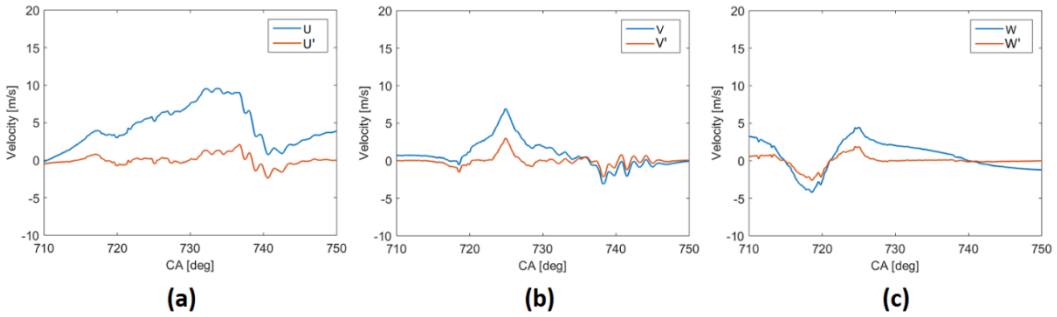

Figure 123. The turbulence contribution of velocity versus the velocity at different directions for cycle 4

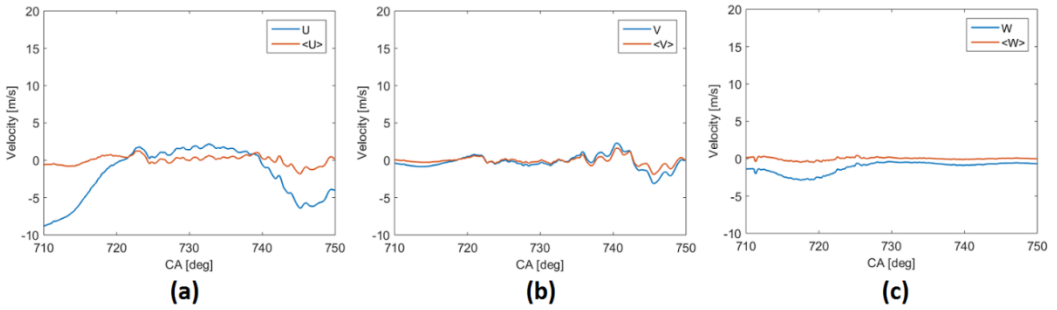

Figure 124. The mean contribution of velocity versus the velocity at different directions for cycle 5

After the calculation of the resolved turbulent kinetic energy, shown in Equation 45, the total kinetic energy is calculated using Equation 46, in which TKE_{model} is obtained by solving the RNG-Ke model equations.

$$TKE_{resolved} = \frac{U'^2 + V'^2 + W'^2}{2} \tag{45}$$

$$TKE_{tot} = TKE_{model} + TKE_{resolved} \quad (46)$$

It can be seen in Figure 125 that the total turbulent kinetic energy (TKE_{tot}) calculated in cycle 4 is always higher than the one in cycle, which indicates that different level of turbulence inside the cylinder from cycle to cycle leads to cyclic variability inside the combustion chamber.

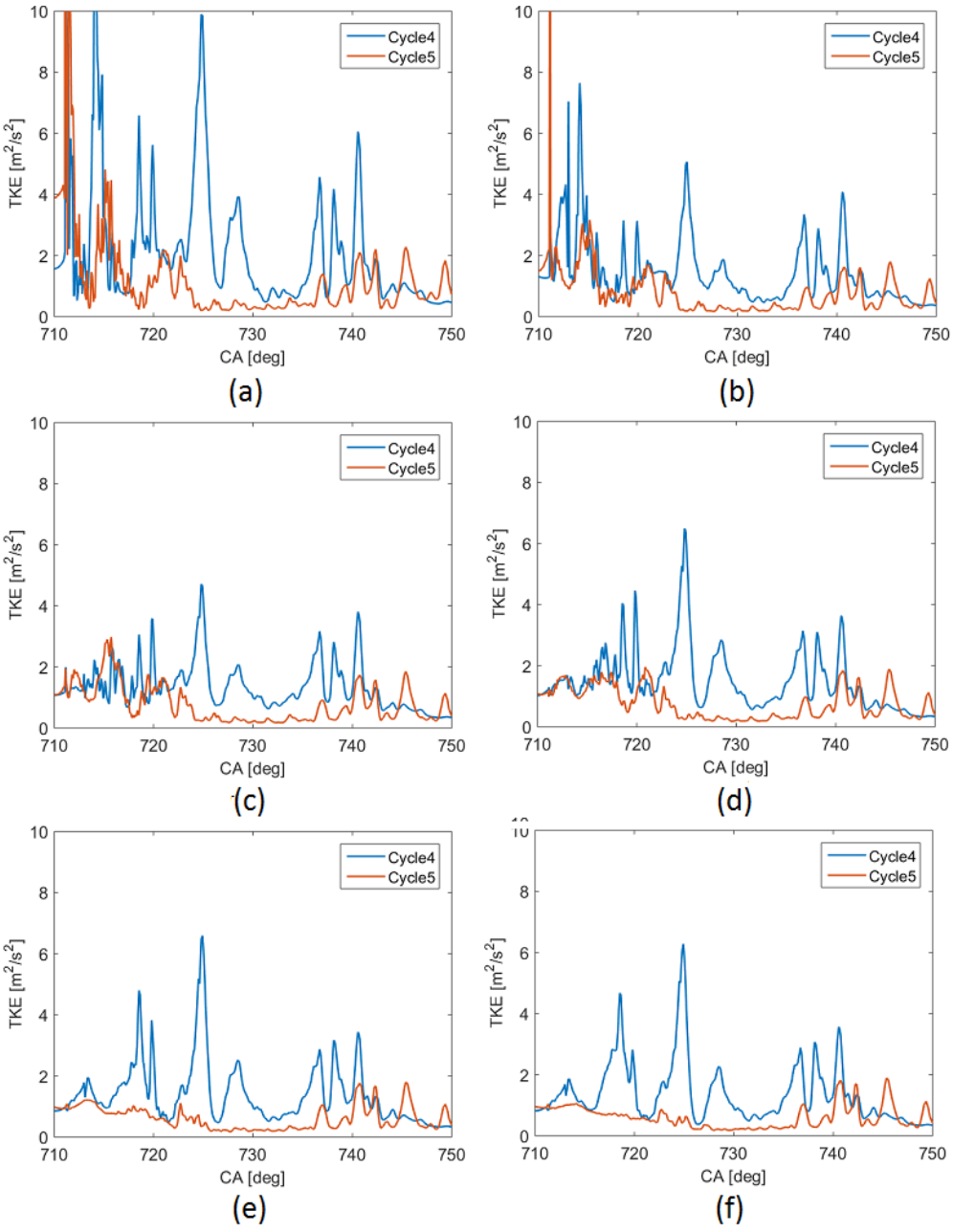

Figure 125. the comparison between total TKE of cycle 4 and 5 at different control volumes

6.3.2. Correlation analysis of the effects of the flow-field and flame structure

In this step, the correlation analysis of the Peak Cylinder Pressure (PCP), which is an indicator of a cycle being high or low, with the flame geometry is studied. Since there is a strong correlation between different indicators of high/low cycles such as PCP, IMEP and MFB50, the analysis is carried out on PCP alone. Figure 126 shows the flame geometry of the highest four cycles, and the lowest four cycles (in terms of PCP) at 722 degrees, which represents 11 degrees after ignition. The choice of 722 degrees is a subjective one, and represents a point where all the cycles have a well-developed flame volume. It is worth mentioning that all the cycles have a different mass fraction burned at 722 degrees.

It can be appreciated from Figure 126, that the high cycles tend to have a flame geometry that is squished in the Z direction (direction of piston motion), and more spread out in the X and Y directions, while the low cycles show a more elongated-in-Z flame volume. Further, the low cycles tend to have a flame volume that is offset to the right (towards the exhaust port), while the high cycles have flame volumes that are more symmetric left to right. Clearly a more symmetric flame is preferable for faster combustion so the charge may be consumed equally in all directions before the flame hits a wall. Moreover, a squished flame volume (in Z) allows the flame to propagate more in the XY direction, consuming the charge, rather than hitting the piston earlier on in its combustion progress.

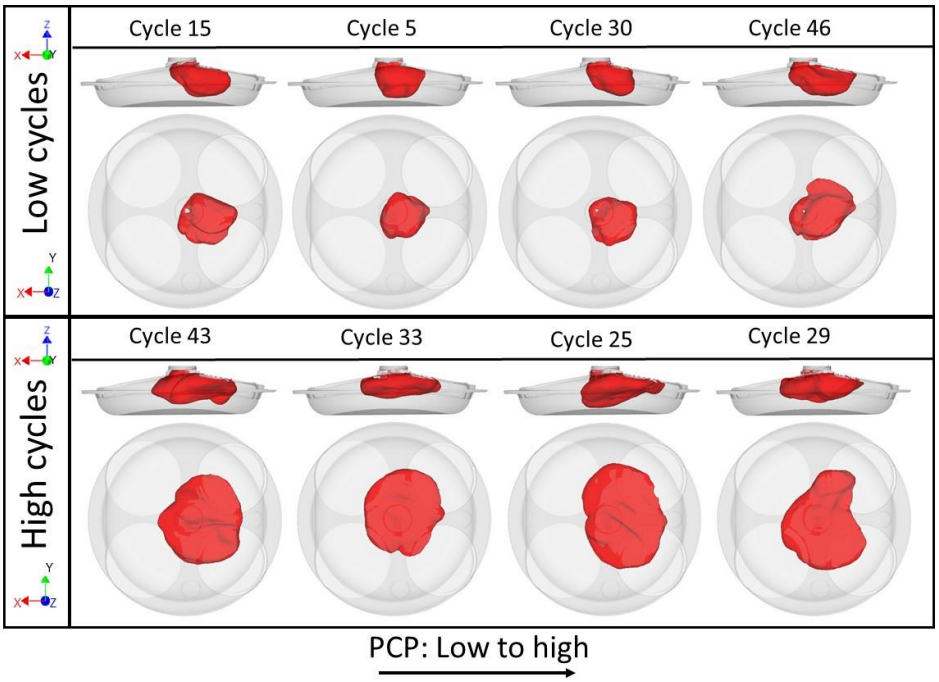

Figure 126. Flame geometry at 722 degrees for the highest four and lowest four cycles by PCP [86]

Figure 127 shows the correlation between the offset of the Center of Mass of the flame volume at 722 degree with respect to the ignition location (COMoX), and the span of the flame volume in the Z direction (ZZ), with respect to PCP. From Figure 127, it can be noted that over the 49 cycles simulated, cycles that have a higher offset of their flame volume center of mass at 722 degree in the negative X direction have a lower PCP, though there is some scatter in this distribution (with R^2 of 0.2731). Moreover, it can be realized from Figure 127 that there is a mild negative correlation between PCP, and the span of the flame volume in the Z direction at 722 degree (with R^2 of 0.0488).

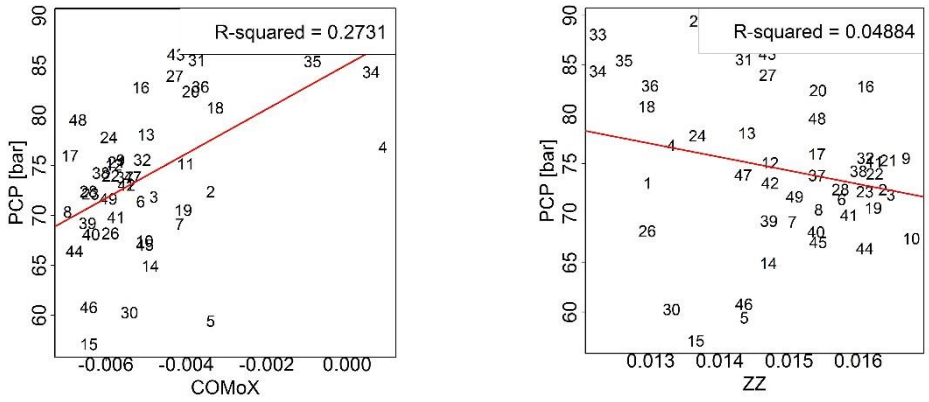

Figure 127. Correlation between PCP and COMoX (left) and ZZ (right) [86]

The reasoning behind the relatively low correlation between ZZ and PCP can be explained based on the fact that there are two competing effects when looking at the flame geometry at 722 degree. Firstly, cycles that have a higher PCP would have also burned to a greater extent compared to low cycles by 722 degree. Hence their flame volumes would be larger, and therefore their ZZ values would be higher. Secondly, the flame geometries that are more elongated in the Z direction (for a given mass fraction burned) tend to produce lower PCP cycles. This is clearer when focusing on the strong positive correlation between XX and YY (span of the flame in the X and Y directions respectively) with respect to PCP, as shown in Figure 128. Therefore, a strong positive correlation between ZZ and PCP too would be expected, which cannot be detected from Figure 127.

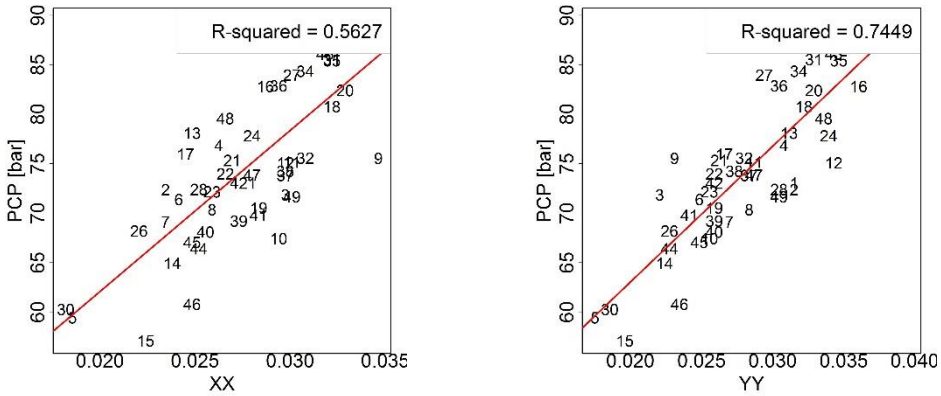

Figure 128. Correlation between PCP and XX (left) and YY (right)

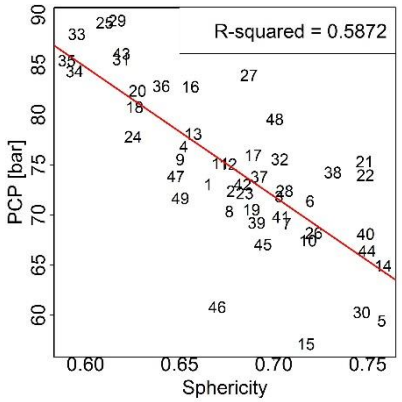

Figure 129. Correlation between PCP and sphericity of the flame volumes at 722° [86]

In order to take out the confounding effect of mass MFB on ZZ, the flame shapes of the two highest PCP cycles (25 and 29), and the two lowest PCP cycles (5 and 15) at the same MFB value of 3% are analysed (shown in Figure 130). This value of MFB occurs at 720.6˚, 721.02˚, 725.2˚, and 724.5˚ for cycles 25, 29, 5, and 15; respectively.

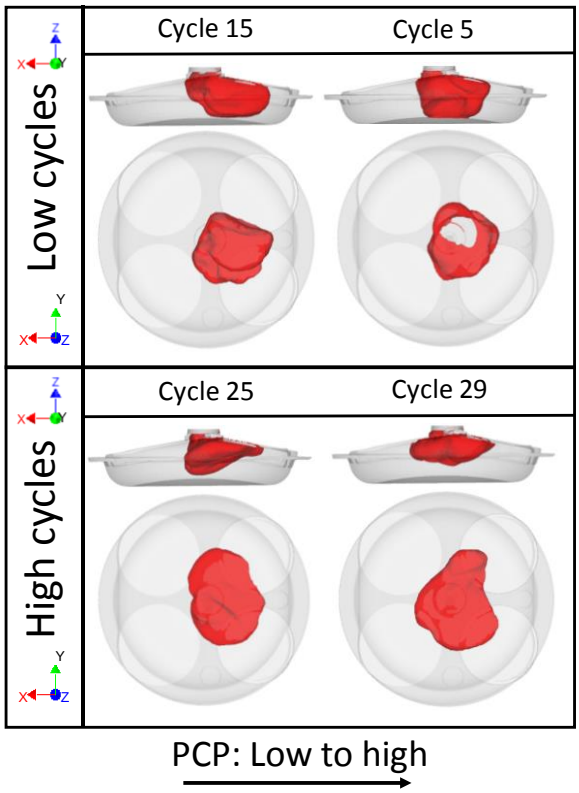

Figure 130. Flame geometry at 3% MFB for the highest two and the lowest two cycles in terms of PCP [86]

Table 6 reports the values of following parameters for these cycles, #15, #5, #25 and #29, at 3% MFB:

- Sphericity which is proportional to the flame volume divided by flame surface area
- Flame area,
- Flame volume
- ZZ which is the span of the flame volume in the Z direction

Table 6. Flame shape metrics for the highest two and the lowest two cycles at 3% mass fraction burned occurring at different crank angles [86]

Cycle# [-]	CA [deg]	Sphericity [-]	Flame Area [mm^2]	Flame Volume [mm^3]	ZZ [mm]	PCP [bar]
15	724.5	0.691	1.65E+03	3.62E+03	15.8	57.10
5	725.2	0.731	1.70E+03	4.11E+03	16.5	59.42
25	720.6	0.635	1.86E+03	3.81E+03	14.7	89.23
29	721.02	0.637	1.87E+03	3.88E+03	13	89.43

It can be stated that the low cycles have higher ZZ values, and lower flame areas. The flame volumes are roughly equal for the four cycles, since they are all at the same MFB. Thus, the sphericity (which is proportional to the flame volume divided by flame surface area) of the low PCP cycle flames is higher (more sphere-like flames), while the high PCP cycles, being more squished have lower sphericity.

In order to understand the potential link between velocity fields and flame geometry, the pre-ignition velocity fields for the highest four and lowest four cycles by PCP were studied. The velocity flow-fields for these cycles at 710 degree (1 degree before ignition) is depicted in Figure 131.

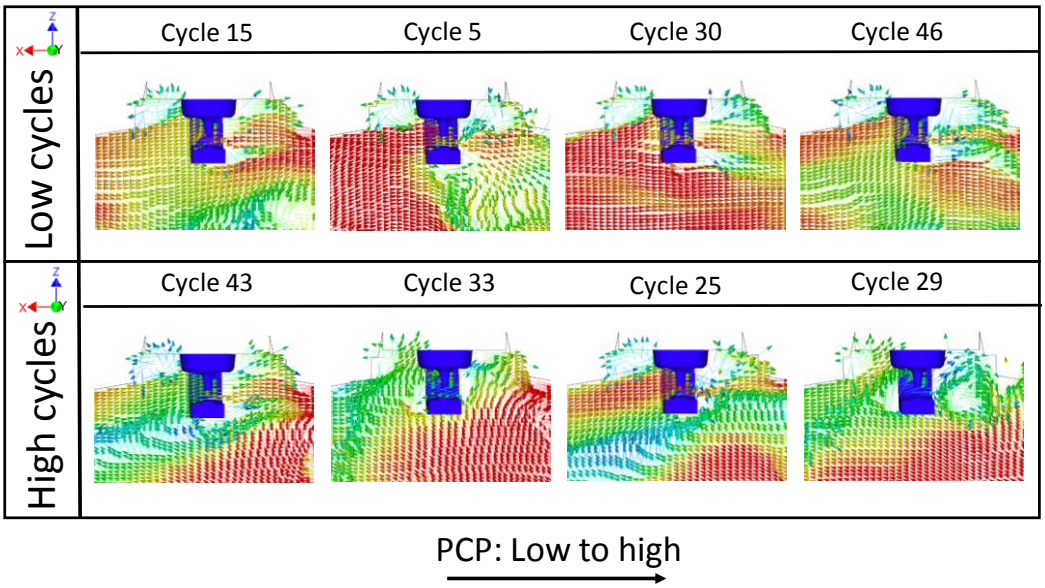

Figure 131. Velocity flow field snapshot at 710 degrees (1 degree prior to ignition) for the four lowest and the four highest cycles in terms of PCP, shown on the tumble plane [86]

It is important to note that the low cycles tend to have a stronger velocity in the negative X direction (from intake to exhaust) in the spark gap prior to ignition. This flow is generated by the tumble (the XZ plane is the tumble plane, and the YZ plane is the cross-tumble plane) which is perhaps the reason why the low cycles tend to have a more offset flame volume in the negative X-direction later on in the cycle. This assumption can be confirmed by computing the average pre-ignition velocities (at 710 degree, 1 degree prior to ignition) in a spherical monitor volume of radius 5.5 mm (shown in Figure 120).

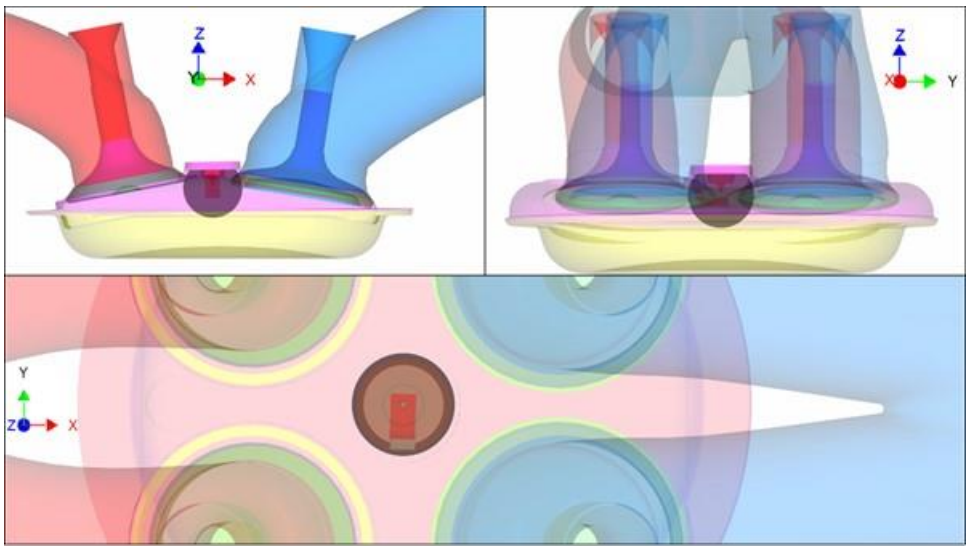

Figure 132. Monitor volume for evaluating average velocities in the X, Y, and Z directions prior to ignition. Note that the negative X direction (towards the exhaust) represents the direction of the mean flow created by tumble [86]

The correlation between the COMoX (at 722 degree) and the pre-ignition (at 710 degree) value of the velocity in the X-direction in the monitor volume (denoted as U5.5mm) is depicted in Figure 133. It can be observed that cycles that with a stronger negative X velocity in the spark gap prior to ignition tend to have a more offset flame volume later on in the cycle.

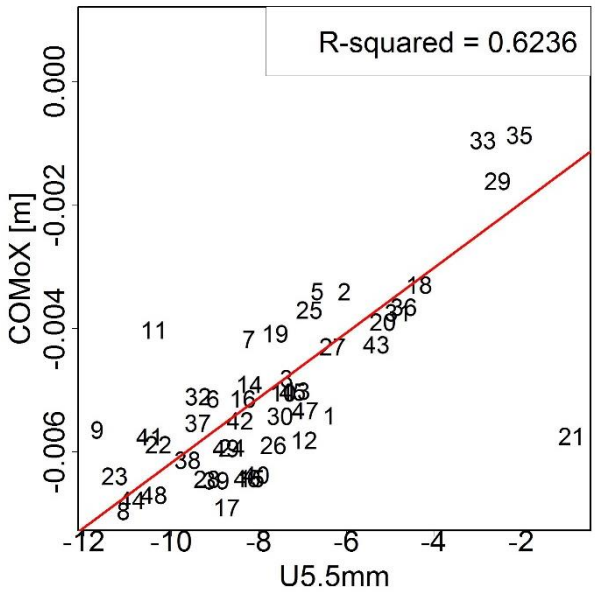

Figure 133. Correlation between COMoX (at 722 degree) and the average pre-ignition (at 710 degree) in X-direction velocity (U5.5mm) computed in a spherical monitor volume of 5.5 mm radius, centered at the ignition location [86]

From this monitor volume, it can be seen that the high cycles tend to have a higher velocity in the positive Z direction pre-ignition (from piston to the head), though this is not immediately apparent from Figure 131. This higher upward Z velocity for certain cycles is likely to squish the flame volume upwards towards the head, resulting in larger surface area to volume for these cycles' flames, leading to faster combustion and higher PCP. Figure 134 shows the correlation between PCP and U5.5mm (left), V5.5mm (middle), and W5.5mm (right), which represent respectively the average X, Y, and Z velocities in a spherical monitor volume of 5.5 mm radius centered at the ignition location, at 710 degree (1 degree before ignition). As it can be seen from Figure 134, cycles that with a higher value of velocity in the negative X direction (towards the exhaust) tend to be lower cycles, as discussed previously. Moreover, cycles with a higher W5.5mm value (or a stronger upward flow from the piston to the head prior to ignition) tend to produce higher values of PCP (high cycles) potentially through the squishing effect on the flame volume. It is also interesting to note that though both the X and Y directions represent the radial directions in the combustion chamber, unlike with U5.5mm, there is no significant correlation between PCP and V5.5mm values; which is likely due to the fact that the Y-axis in the model is orthogonal to the tumble direction.

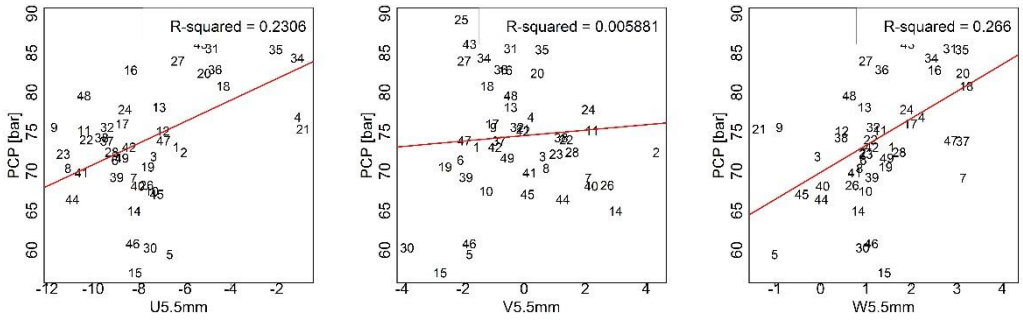

Figure 134. Correlation between PCP and U5.5mm (left), V5.5mm (middle), and W5.5mm (right), which represent respectively the average X, Y, and Z velocities in a spherical monitor volume of 5.5 mm radius centered at the ignition location, at 710 degree (1 degree before ignition) [86]

To remove any bias with respect to axes orientation and the tumble/cross-tumble planes, the X and Y axes were rotated counter-clockwise by 45 degree, and U5.5mmROT and V5.5mmROT were re-computed with respect to the rotated axes. As it can be observed in Figure 135, the correlation between the X-velocities (U5.5mmROT) and PCP goes down in terms of R^2 value, while the correlation between the Y-velocities (V5.5mmROT) and PCP goes up in terms of R^2 value.

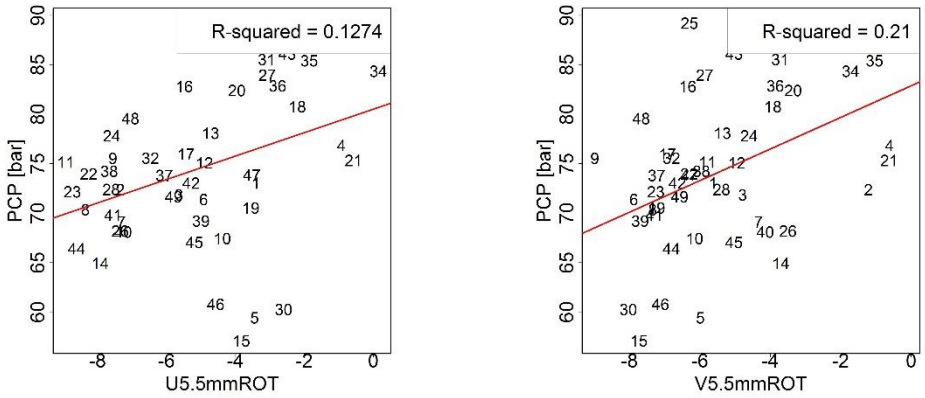

Figure 135. Correlation between PCP with respect to U5.5mmROT (left) and V5.5mmROT (right) after rotating the X and Y axes by 45˚ in the counter-clockwise direction and computing the average X and Y velocities respectively in a spherical monitor volume of 5.5 mm radius centered at the ignition location, at 710° (1 degree before ignition) [86]

Chapter 7

Conclusions

Worldwide legislations are significantly reducing the mandatory limits for CO_2 target. Moreover, the introduction of dynamic test procedures such as WLTP and RDE moves the operating area of the engine to higher loads and hence increasing the knock likelihood in SI engines. Therefore, the aim of the current work is to investigate, through experimental and numerical analysis, the potential benefits of different knock mitigation techniques and to develop reliable and predictive simulation models aiming to detect root cause of cyclic variations and knock phenomena in downsized turbocharged SI engines.

First, technologies for the enhancements of SI engines efficiencies, such as downsizing and turbocharging, coupled with Miller cycles, LP EGR, cylinder deactivation and water injection were experimentally and numerically investigated.

As far as Miller cycle is considered; a consistent efficiency enhancement has been achieved at medium speeds and high loads, while LIVC strategy was less effective at lower speeds where turbocharger is not capable to provide sufficient boost to compensate for the volumetric efficiency reduction. It was found out that utilization of LIVC strategy leads up to 20% improvement in the engine indicated fuel conversion efficiency.

Regarding WI technology, the potential knock mitigation was confirmed through a detailed experimental study followed by 3D-CFD simulations. It was demonstrated that the engine fuel efficiency can be improved at part and high load condition up to 4 and 4.5%, respectively, thanks to increasing geometric compression ratio with limited impact on full load performances.

Afterwards, considering that various advanced and complex technologies are being exploited in the development of SI engines, the necessity of understanding

their effect on the combustion process, cycle to cycle variations and knock is of crucial importance; therefore, prediction of combustion is a major step in the combustion optimization which can be achieved through both experimental and numerical analysis, using 0D and 3D CFD simulation tools.

In the current study, primary, the predictive capabilities of a 0D phenomenological turbulence model, based on the K-k and k-ε approaches, coupled with a turbulent combustion model, have been assessed for a typical European downsized and turbocharged SI engine over a wide range of speed, load, lambda, EGR, water injected and spark timings operating conditions. The model has been properly tuned in order not only to predict the mean cycle but also the CCV. The combustion model used in this work could therefore be utilized as a "virtual test rig" from the early stage of new engines development, thanks to its reduced computational and calibration requirements.

Considering that CCV is an important step to predict knock, in the next step, LES has been performed using 3D-CFD simulations in order to understand the root cause of CCV. The effects of the velocity field and the equivalence ratio field (in the spark gap region prior to ignition) on CCV have been decoupled confirming that the velocity field and not the equivalence ratio field is what results in differences in flame propagation from cycle to cycle for the stable operating point under studied.

To wrap up, since efficient performance of SI engines has a great significance in today's automotive industry, understanding the effectiveness of various advanced technologies in terms of fuel economy enhancement is of crucial importance. As a consequence, robust and reliable methods for the prediction of the combustion process and CCV as discussed in this study can be used to support the design and calibration of modern high-performance, downsized and turbocharged SI engines.

References

[1] Z. Yang, Some upcoming changes in the ICCT global passenger vehicle GHG standard comparison charts, (2014). http://www.theicct.org/.

[2] A. Königstein, U.D. Grebe, K.-J. Wu, P.-I. Larsson, Differentiated analysis of downsizing concepts, MTZ Worldw. 69 (2008) 4–11. doi:10.1007/BF03227890.

[3] P. Leduc, B. Dubar, A. Ranini, G. Monnier, Downsizing of Gasoline Engine: an Efficient Way to Reduce CO2 Emissions, Oil Gas Sci. Technol. – Rev. IFP. 58 (2003) 115–127. doi:10.2516/ogst:2003008.

[4] C. Schernus, J. Ewald, F. Di Matteo, Methods to Reduce End Gas Temperatures for Lower Knocking Sensitivity – A Simulation Study, SIA Tech. Pap. (2013).

[5] F. Millo, Knock & Megaknock: the ultimate barrier to s.i. engines downsizing ?, SAE 2014 High Effic. IC Engine Symp. (2014).

[6] S. Luisi, V. Doria, A. Stroppiana, Knock Mitigation Techniques for highly boosted downsized SI engines, in: Proc. CO2 Reduct. Transp. Syst. ATA – SAE Int. Conf., Turin, Italy, 2017.

[7] F. Millo, M. Mirzaeian, S. Luisi, V. Doria, A. Stroppiana, Engine displacement modularity for enhancing automotive s.i. engines efficiency at part load, Fuel. 180 (2016) 645–652. doi:10.1016/j.fuel.2016.04.049.

[8] R. Flierl, F. Lauer, M. Breuer, W. Hannibal, Cylinder Deactivation with Mechanically Fully Variable Valve Train, SAE Int. J. Engines. 5 (2012) 207–215. doi:10.4271/2012-01-0160.

[9] M.R. Gaballo, M. Giodice, A. Diano, F. Fersini, F. Miccolis, S. Mannal, S. Motz, Application of a Modular Simulation Approach : Optimizations from Combustion to Vehicle Management, SAE Int. (2015). doi:10.4271/2015-24-2505.

[10] S. Potteau, P. Lutz, S. Leroux, S. Moroz, E. Tomas, Cooled EGR for a Turbo

SI Engine to Reduce Knocking and Fuel Consumption, in: SAE Tech. Pap., SAE International, 2007. doi:10.4271/2007-01-3978.

[11] D.B. Roth, P. Keller, M. Becker, Requirements of External EGR Systems for Dual Cam Phaser Turbo GDI Engines, in: SAE Tech. Pap., SAE International, 2010. doi:10.4271/2010-01-0588.

[12] F. Hoppe, M. Thewes, H. Baumgarten, J. Dohmen, Water injection for gasoline engines: Potentials, challenges, and solutions, Int. J. Engine Res. 17 (2016) 86–96. doi:10.1177/1468087415599867.

[13] F. Bozza, V. DeBellis, L. Teodosio, Potentials of cooled EGR and water injection for knock resistance and fuel consumption improvements of gasoline engines, Appl. Energy. 169 (2016) 112–125. doi:10.1016/j.apenergy.2016.01.129.

[14] R. Miller, High-pressure supercharging system, Patent Number: 2670595, 1954. http://www.freepatentsonline.com/2670595.html.

[15] T. Li, Y. Gao, J. Wang, Z. Chen, The Miller cycle effects on improvement of fuel economy in a highly boosted, high compression ratio, direct-injection gasoline engine: EIVC vs. LIVC, Energy Convers. Manag. 79 (2014) 59–65. doi:10.1016/j.enconman.2013.12.022.

[16] M. Mirzaeian, F. Millo, L. Rolando, Assessment of the Predictive Capabilities of a Combustion Model for a Modern Downsized Turbocharged SI Engine, in: SAE Tech. Pap., SAE International, 2016. doi:10.4271/2016-01-0557.

[17] F. Millo, L. Rolando, E. Pautasso, E. Servetto, A Methodology to Mimic Cycle to Cycle Variations and to Predict Knock Occurrence through Numerical Simulation, Sae. (2013) 2014-4–1. doi:10.4271/2014-01-1070.

[18] S. Luisi, V. Doria, A. Stroppiana, F. Millo, M. Mirzaeian, Experimental Investigation on Early and Late Intake Valve Closures for Knock Mitigation through Miller Cycle in a Downsized Turbocharged Engine, in: SAE Tech. Pap., SAE International, 2015. doi:10.4271/2015-01-0760.

[19] L. Bernard, A. Ferrari, D. Micelli, A. Perotto, R. Rinolfi, F. Vattaneo, Electrohydraulic valve control with MultiAir technology, MTZ Press 12I2009. 70 (2009).

[20] L. Postrioti, M. Bosi, A. Mariani, C. Ungaro, Momentum Flux Spatial Distribution and PDA Analysis of a GDI Spray, in: SAE Tech. Pap., SAE International, 2012. doi:10.4271/2012-01-0459.

[21] L. Postrioti, G. Caponeri, G. Buitoni, N. Van Vuuren, Experimental Assessment of a Novel Instrument for the Injection Rate Measurement of Port Fuel Injectors in Realistic Operating Conditions, SAE Int. J. Fuels Lubr. 10 (2017). doi:10.4271/2017-01-0830.

[22] J.P. Zammit, M.J. McGhee, P.J. Shayler, I. Pegg, Benefits of cylinder deactivation on a diesel engine and restrictions due to low boost, in: Intern. Combust. Engines Performance, Fuel Econ. Emiss., Elsevier, 2013: pp. 95–108. doi:10.1533/9781782421849.3.95.

[23] A. Ihlemann, N. Nitz, Cylinder Deactivation A technology with a future or a niche application?, 10th Schaeffler Symp. (2014).

[24] A. Grob, C. Brinkmann, J. Königstedt, The new Audi 4.0-L V8 TFSI engine Part 2: Thermodynamics and Calibration, MTZ Worldw. (2013).

[25] S. Birch, VW debuts cylinder deactivation on 2012 V8 and I4 engines, Automot. Eng. Mag. (2011).

[26] T.G. Leone, M. Pozar, Fuel Economy Benefit of Cylinder Deactivation - Sensitivity to Vehicle Application and Operating Constraints, in: SAE Tech. Pap., SAE International, 2001. doi:10.4271/2001-01-3591.

[27] H. Faust, Powertrain Systems of the Future Engine, transmission and damper systems for downspeeding, downsizing, and cylinder deactivation, 2nd Schaeffler Symp. (2014).

[28] R. Anca, M. Haas, M. Rauch, G. Padroni, UniAir – a fully variable valve train system for gasoline and diesel engines, SIA Tech. Pap. (2006).

[29] F. Millo, S. Luisi, F. Borean, A. Stroppiana, Numerical and experimental investigation on combustion characteristics of a spark ignition engine with an early intake valve closing load control, Fuel. 121 (2014) 298–310. doi:10.1016/j.fuel.2013.12.047.

[30] R. Flierl, S. Schmitt, G. Kleinert, H.-J. Esch, H. Dismon, Univalve - A Fully Variable Mechanical Valve Lift System for Future Internal Combustion Engines, MTZ Worldw. (2011).

[31] R. Flierl, M. Paulov, A. Knecht, W. Hannibal, Investigations with a Mechanically Fully Variable Valve Train on a 2.0l Turbo Charged Four Cylinder Engine, in: SAE Tech. Pap., SAE International, 2008. doi:10.4271/2008-01-1352.

[32] K. WIttek, CO2-potential of a two-stage VCR system in combination with

future gasoline powertrains, 33rd Intern. Vienna Mot. Symp. (2012).

[33] R. Miller, High expansion, spark ignited, gas burning, internal combustion engines, Patent Number: US 2773490 A, 1956. https://www.google.com/patents/US2773490.

[34] R. Miller, Supercharged engine, Patent Number: 2817322, 1957. http://www.freepatentsonline.com/2817322.html.

[35] K. Okamoto, F.-R. Zhang, S. Shimogata, F. Shoji, Development of a Late Intake-Valve Closing (LIVC) Miller Cycle for Stationary Natural Gas Engines - Effect of EGR Utilization, in: SAE Tech. Pap., SAE International, 1997. doi:10.4271/972948.

[36] J.B. Heywood, Internal Combustion Engine Fundementals, 1988. doi:10987654.

[37] F. Bedford, C. Rutland, P. Dittrich, A. Raab, F. Wirbeleit, Effects of Direct Water Injection on DI Diesel Engine Combustion, in: SAE Tech. Pap., SAE International, 2000. doi:10.4271/2000-01-2938.

[38] R. Lanzafame, Water Injection Effects In A Single-Cylinder CFR Engine, in: SAE Tech. Pap., SAE International, 1999. doi:10.4271/1999-01-0568.

[39] J.A. Harrington, Water Addition to Gasoline-Effect on Combustion, Emissions, Performance, and Knock, in: SAE Tech. Pap., SAE International, 1982. doi:10.4271/820314.

[40] V. Doria, A. Stroppiana, M. Ferrera, F. Millo, M. Mirzaeian, D. Porcu, Knock Mitigation Techniques for Highly Boosted Downsized SI Engines: Miller Cycle and Water Injection, in: SIA Powertrain, Versailles, France, 2016.

[41] Converge user manual, 2016.

[42] F. Millo, M. Badami, A. Bianco, E. Delogu, CFD Diagnostic Methodology for the Assessment of Mixture Formation Quality in GDI Engines, SAE Int. J. Engines. 4 (2011) 2461–2476. doi:10.4271/2011-24-0151.

[43] M. Badami, F. Millo, A. Pinzello, The Extended Phenomenological Spray Model (EPSM): A New Approach For CFD Diesel Fuel Spray Simulation Under Evaporative and Nonevaporative Conditions, At. Sprays. 18 (2008) 669–697. doi:10.1615/AtomizSpr.v18.i8.10.

[44] M. Wenig, M. Grill, M. Bargende, A New Approach for Modeling Cycle-to-

Cycle Variations within the Framework of a Real Working-Process Simulation, SAE Int. J. Engines. 6 (2013) 1099–1115. doi:10.4271/2013-01-1315.

[45] G. D'Errico, Prediction of the combustion process and emission formation of a bi-fuel s.i. engine, Energy Convers. Manag. 49 (2008) 3116–3128. doi:https://doi.org/10.1016/j.enconman.2008.06.012.

[46] F. Bozza, A. Gimelli, A Comprehensive 1D Model for the Simulation of a Small-Size Two-Stroke SI Engine, in: SAE Tech. Pap., SAE International, 2004. doi:10.4271/2004-01-0999.

[47] O. Vitek, J. Macek, C. Poetsch, R. Tatschl, Modeling Cycle-to-Cycle Variations in 0-D/1-D Simulation by Means of Combustion Model Parameter Perturbations based on Statistics of Cycle-Resolved Data, SAE Int. J. Engines. 6 (2013) 1075–1098. doi:10.4271/2013-01-1314.

[48] V. DeBellis, E. Severi, S. Fontanesi, F. Bozza, Hierarchical 1D/3D approach for the development of a turbulent combustion model applied to a VVA turbocharged engine. Part II: Combustion model, Energy Procedia. 45 (2014) 1027–1036. doi:10.1016/j.egypro.2014.01.108.

[49] M. Rivas, P. Higelin, C. Caillol, O. Sename, E. Witrant, V. Talon, Validation and Application of a New 0D Flame/Wall Interaction Sub Model for SI Engines, SAE Int. J. Engines. 5 (2011) 718–733. doi:10.4271/2011-01-1893.

[50] J.. Gatowski, J.B. Heywood, Flame photographs in a spark-ignition engine, Combust. Flame. 56 (1984) 71–81. http://www.refdoc.fr/Detailnotice?idarticle=12361230.

[51] S. Richard, S. Bougrine, G. Font, F.A. Lafossas, F. le Berr, On the Reduction of a 3D CFD Combustion Model Simulation Tools for Powertrain Design and Control to Build a Physical 0D Model for Simulating Heat Release, Knock and Pollutants in SI Engines, Oil Gas Sci. Technol. 64 (2009) 223–242. doi:10.2516/ogst/2008055.

[52] F.C. Gouldin, An application of fractals to modeling premixed turbulent flames, Combust. Flame. 68 (1987) 249–266. doi:10.1016/0010-2180(87)90003-4.

[53] S. Wahiduzzaman, T. Moral, S. Sheard, Comparison of Measured and Predicted Combustion Characteristics of a Four-Valve S.I. Engine, in: SAE Tech. Pap., SAE International, 1993. doi:10.4271/930613.

[54] C. Poetsch, H. Schuemie, H. Ofner, R. Tatschl, A Computational Study on

the Impact of Cycle- to-Cycle Combustion Fluctuations on Fuel Consumption and Knock in Steady-State and Drivecycle Operation, (2013). doi:10.4271/2013-24-0030.

[55] V. DeBellis, L. Teodosio, D. Siano, F. Minarelli, D. Cacciatore, Knock and Cycle by Cycle Analysis of a High Performance V12 Spark Ignition Engine. Part 1: Experimental Data and Correlations Assessment, SAE Int. J. Engines. 8 (2015) 1993–2001. doi:10.4271/2015-24-2392.

[56] F. Bozza, V. DeBellis, F. Minarelli, D. Cacciatore, Knock and Cycle by Cycle Analysis of a High Performance V12 Spark Ignition Engine. Part 2: 1D Combustion and Knock Modeling, SAE Int. J. Engines. 8 (2015) 2002–2011. doi:10.4271/2015-24-2393.

[57] C.K. Westbrook, W.J. Pitz, W.R. Leppard, The Autoignition Chemistry of Paraffinic Fuels and Pro-Knock and Anti-Knock Additives: A Detailed Chemical Kinetic Study, in: SAE Tech. Pap., SAE International, 1991. doi:10.4271/912314.

[58] R.D. Wilk, R.M. Green, W.J. Pitz, C.K. Westbrook, S. Addagarla, D.L. Miller, N.P. Cernansky, An Experimental and Kinetic Modeling Study of the Combustion of n-Butane and Isobutane in an Internal Combustion Engine, in: SAE Tech. Pap., SAE International, 1990. doi:10.4271/900028.

[59] O. Colin, A. Pires Da Cruz, S. Jay, Detailed chemistry-based auto-ignition model including low temperature phenomena applied to 3-D engine calculations, Proc. Combust. Inst. 30 II (2005) 2649–2656. doi:10.1016/j.proci.2004.08.058.

[60] H.S. Soyhan, F. Mauss, C. Sorusbay, Chemical kinetic modeling of combustion in internal combustion engines using reduced chemistry, Combust. Sci. Technol. 174 (2002) 73–91. doi:10.1080/00102200290021560.

[61] J.S. Cowart, J.C. Keck, J.B. Heywood, C.K. Westbrook, W.J. Pitz, Engine knock predictions using a fully-detailed and a reduced chemical kinetic mechanism, Symp. Combust. 23 (1991) 1055–1062. doi:10.1016/S0082-0784(06)80364-4.

[62] J.S. Cowart, M. Haghgooie, C.E. Newman, G.C. Davis, W.J. Pitz, C.K. Westbrook, The Intensity of Knock in an Internal Combustion Engine: An Experimental and Modeling Study, in: SAE Tech. Pap., SAE International, 1992. doi:10.4271/922327.

[63] J.C. Livengood, P.C. Wu, Correlation of autoignition phenomena in internal

combustion engines and rapid compression machines, Symp. Combust. 5 (1955) 347–356. doi:10.1016/S0082-0784(55)80047-1.

[64] S. Soylu, Prediction of knock limited operating conditions of a natural gas engine, Energy Convers. Manag. 46 (2005) 121–138. doi:10.1016/j.enconman.2004.02.014.

[65] A.M. Douaud, P. Eyzat, Four-Octane-Number Method for Predicting the Anti-Knock Behavior of Fuels and Engines, in: SAE Tech. Pap., SAE International, 1978. doi:10.4271/780080.

[66] N. Fogla, M. Bybee, M. Mirzaeian, F. Millo, S. Wahiduzzaman, Development of a K-k-∈ Phenomenological Model to Predict In-Cylinder Turbulence, SAE Int. J. Engines. 10 (2017) 562–575.

[67] F. Bozza, A. Gimelli, L. Strazzullo, E. Torella, C. Cascone, Steady-State and Transient Operation Simulation of a "Downsized" Turbocharged SI Engine, in: SAE Tech. Pap., SAE International, 2007. doi:10.4271/2007-01-0381.

[68] T. Morel, R. Keribar, A Model for Predicting Spatially and Time Resolved Convective Heat Transfer in Bowl-in-Piston Combustion Chambers, in: SAE Tech. Pap., SAE International, 1985. doi:10.4271/850204.

[69] T. Morel, N.N. Mansour, Modeling of Turbulence in Internal Combustion Engines, SAE Tech. Pap. 820040. (1982). doi:10.4271/820040.

[70] S. Grasreiner, J. Neumann, C. Luttermann, M. Wensing, C. Hasse, A quasi-dimensional model of turbulence and global charge motion for spark ignition engines with fully variable valvetrains, Int. J. Engine Res. 15 (2014) 805–816. doi:10.1177/1468087414521615.

[71] GT-SUITE Engine Performance Application Manual, Gamma Technologies, 2016.

[72] F. Millo, E. Pautasso, D. Delneri, M. Troberg, A DoE Analysis on the Effects of Compression Ratio, Injection Timing, Injector Nozzle Hole Size and Number on Performance and Emissions in a Diesel Marine Engine, in: SAE Tech. Pap., SAE International, 2007. doi:10.4271/2007-01-0670.

[73] M. Sjeric, D. Kozarac, I. Taritas, Experimentally Supported Modeling of Cycle-to-Cycle Variations of SI Engine Using Cycle-Simulation Model, (2014). doi:10.4271/2014-01-1069.

[74] A. Dulbecco, S. Richard, C. Angelberger, Investigation on the Potential of Quantitatively Predicting CCV in DI-SI Engines by Using a One-

Dimensional CFD Physical Modeling Approach: Focus on Charge Dilution and In-Cylinder Aerodynamics Intensity, SAE Int. J. Engines. 8 (2015) 2012–2028. doi:10.4271/2015-24-2401.

[75] F. Millo, C. V Ferraro, Knock in S.I. Engines: A Comparison between Different Techniques for Detection and Control, in: SAE Tech. Pap., SAE International, 1998. doi:10.4271/982477.

[76] M. van Aken, F. Willems, D.-J. de Jong, Appliance of High EGR Rates With a Short and Long Route EGR System on a Heavy Duty Diesel Engine, in: SAE Tech. Pap., SAE International, 2007. doi:10.4271/2007-01-0906.

[77] K. Kumano, S. Yamaoka, Analysis of Knocking Suppression Effect of Cooled EGR in Turbo-Charged Gasoline Engine, in: SAE Tech. Pap., SAE International, 2014. doi:10.4271/2014-01-1217.

[78] M. Dong, G. Chen, M. Xu, C. Daniels, A Preliminary CFD Investigation of In-Cylinder Stratified EGR for Spark Ignition Engines, in: SAE Tech. Pap., SAE International, 2002. doi:10.4271/2002-01-1734.

[79] S. Das, J.C. Dent, A CFD Study of a 4-Valved, Fuel Injected Two-Stroke Spark Ignition Engine, in: SAE Tech. Pap., SAE International, 1993. doi:10.4271/930070.

[80] C.J. Rutland, Large-eddy simulations for internal combustion engines – a review, Int. J. Engine Res. 12 (2011) 421–451. doi:10.1177/1468087411407248.

[81] O. Vermorel, S. Richard, O. Colin, C. Angelberger, A. Benkenida, D. Veynante, Towards the understanding of cyclic variability in a spark ignited engine using multi-cycle {LES}, Combust. Flame. 156 (2009) 1525–1541. doi:http://dx.doi.org/10.1016/j.combustflame.2009.04.007.

[82] B. Enaux, V. Granet, O. Vermorel, C. Lacour, C. Pera, C. Angelberger, T. Poinsot, LES study of cycle-to-cycle variations in a spark ignition engine, Proc. Combust. Inst. 33 (2011) 3115–3122. doi:10.1016/j.proci.2010.07.038.

[83] C. Pera, S. Richard, C. Angelberger, Exploitation of Multi-Cycle Engine LES to Introduce Physical Perturbations in 1D Engine Models for Reproducing CCV, in: SAE Tech. Pap., SAE International, 2012. doi:10.4271/2012-01-0127.

[84] E. Pomraning, Development of large eddy simulation turbulence models, University of Wisconsin-Madison, 2000.

[85] M. Metghalchi, J.C. Keck, Burning velocities of mixtures of air with methanol, isooctane, and indolene at high pressure and temperature, Combust. Flame. 48 (1982) 191–210. doi:10.1016/0010-2180(82)90127-4.

[86] E. Zhao, A.A. Moiz, S. Sibendu, N. Fogla, M. Bybee, S. Wahiduzzaman, M. Mirzaeian, F. Millo, J. Kodavasal, Examining the Role of Flame Topologies and In-cylinder Flow Field on Cyclic Variability in SI Engines Using Large Eddy Simulation, Int. J. Eng. Res. (2017).